Modeling of domain walls dynamics in circular cross-section nanowires

Arnaud De Riz

To cite this version:

Arnaud De Riz. Modeling of domain walls dynamics in circular cross-section nanowires. Materials Science [cond-mat.mtrl-sci]. Université Grenoble Alpes [2020-..], 2021. English. NNT : 2021GRALY012 . tel-03425176

HAL Id: tel-03425176
https://theses.hal.science/tel-03425176

Submitted on 10 Nov 2021

Université Grenoble Alpes

THÈSE

Pour obtenir le grade de

DOCTEUR DE L'UNIVERSITÉ GRENOBLE ALPES

Spécialité : Physique de la Matière Condensée et du Rayonnement

Arrêté ministériel : 25 mai 2016

Présentée par

Arnaud DE RIZ

Thèse dirigée par **Jean-christophe TOUSSAINT**
et codirigée par **Daria GUSAKOVA**

préparée au sein du **Laboratoire Spintronique et Technologie des Composants**
dans **l'École Doctorale Physique**

Modélisation de la dynamique de parois de domaines dans des nanofils à section circulaire

Modeling of domain walls dynamics in circular cross-section nanowires

Thèse soutenue publiquement le **15 mars 2021**,
devant le jury composé de :

Monsieur ANDRE THIAVILLE
DIRECTEUR DE RECHERCHE, CNRS DÉLÉGATION ÎLE-DE-FRANCE SUD, Rapporteur
Monsieur FRANÇOIS MONTAIGNE
PROFESSEUR DES UNIVERSITES, UNIVERSITE DE LORRAINE, Rapporteur
Monsieur MAIRBEK CHSHIEV
PROFESSEUR DES UNIVERSITES, UNIVERSITE GRENOBLE ALPES, Président
Monsieur NICOLAS ROUGEMAILLE
CHARGE DE RECHERCHE HDR, CNRS DÉLÉGATION ALPES, Examinateur
Monsieur MATTHIEU BAILLEUL
CHARGE DE RECHERCHE HDR, CNRS DÉLÉGATION ALSACE, Examinateur

Remerciements

Je voudrais tout d'abord remercier mes encadrants Daria Gusakova et Jean-Christophe Toussaint d'avoir accepté de travailler avec moi. Ils ont su se rendre disponible à chaque fois que j'avais des questions et m'ont encouragé jusqu'au bout.

Je voudrais remercier également, Olivier Fruchart pour avoir proposé une collaboration avec notre équipe ce qui m'a permis d'être plus en contact avec les expérimentateurs. Je le remercie également pour les discussions constructives et ses conseils qui m'ont accompagné tout au long de la thèse.

Je tiens également à remercier Christophe Thirion pour son soutient sur des questions difficiles auxquelles j'ai fait face durant mon parcours.

Je remercie Jérôme Hurst pour sa perspicacité et pour m'avoir épaulé dans mes recherches ainsi que Michael Schöbitz avec qui j'ai beaucoup échangé sur les aspects expérimentaux de mes travaux.

Je remercie aussi Lucian Prejbeanu et Alain Marty d'avoir fait partie de mon comité de suivi de thèse.

J'adresse mes remerciements à André Thiaville et François Montaigne pour avoir accepté d'être mes rapporteurs de thèse ainsi que Mairbek Chshiev, Nicolas Rougemaille et Matthieu Bailleul d'avoir accepté de faire partie de mon jury.

Je voudrais aussi remercier les membres permanents et non-permanents de Spintec pour les nombreux échanges que nous avons eu aussi bien au niveau professionnel qu'au niveau personnel.

Enfin, je tiens à remercier mes parents et mes amis qui m'ont soutenu dans cette épreuve.

Résumé en français

Introduction

Au cours de ces dernières décennies, les conduits magnétiques ont suscité un vif intérêt dans le champ de la spintronique. Ces structures permettent l'étude d'une variété de phénomènes tels que la formation de textures magnétiques, la dynamique d'aimantation sous un courant appliqué et la propagation d'ondes de spin. En raison de l'interaction entre l'aimantation et le spin des électrons, ces conduits sont de bons candidats pour le développement d'applications telles que les mémoires magnétiques [1], la logique de spin [2] et plus récemment, les dispositifs neuromorphiques [3].

Un des phénomènes les plus étudiés en spintronique, à la fois expérimentalement et théoriquement, est le mouvement de paroi de domaines. Le mouvement de paroi initialement considéré sous un champ magnétique appliqué [4, 5] a été étendu depuis le début des années 2000 aux cas sous courant, basés sur les effets du transfert de spin [6], et plus récemment aux cas soumis aux couples spin-orbite [7] et d'autres effets comme des gradients de chaleur [8], de la tension mécanique [9], des ondes de spins [10] etc. Il existe des caractéristiques communes du mouvement de paroi sous l'influence soit d'un champ soit d'un courant qui sont: un état de propagation stationnaire pour de faibles intensités, ainsi qu'un régime précessionnel au-dessus d'un seuil, avec un processus transitoire appelé instabilité de Walker. Ce régime induit des oscillations d'aimantations indésirables ou des changements chaotiques des degrés de liberté internes des parois de domaines.

Jusqu'à récemment, les nanorubans plats avec des parois de domaines sont les types de conduits les plus étudiés, en raison de techniques de fabrication bien établies comme la lithographie. Des études extensives ont été faites sur le mouvement de paroi de domaines à l'intérieur de nanorubands magnétiquement doux sous un champ appliqué ou sous courant [11, 12]. Cependant, des contraintes technologiques liées à l'intégration de telles nanostructures 2D dans un dispositif réel suscitent un intérêt pour des nanostructures naturellement 3D [13], comme par exemple des nanofils cylindriques ou des tubes. Ces géométries sont maintenant disponibles pour des études expérimentales grâce aux avancées des techniques de fabrication [14].

L'extension des nanostructures 2D vers une troisième dimension donne lieu à des textures de spins non conventionnelles, dans lesquelles de nouveaux effets physiques liés à la géométrie, la topologie et la chiralité sont présents. Par exemple, on trouve deux types de paroi de domaines qui sont stables ou métastables selon le diamètre du fil [15]. Sous un seuil d'environ sept fois la longueur d'échange, la configuration la plus stable est une paroi transverse ou transverse-vortex. Cette paroi est caractérisée par une aimantation transverse par rapport à l'axe du fil, ce qui en fait un analogue de la paroi transverse dans un nanoruban plat, spécifiquement dans des petits diamètres. Pour des diamètres un peu plus larges, cette paroi commence à acquérir une vorticité par rapport à sa composante transverse. Au-dessus du diamètre seuil précédemment mentionné, la configuration la plus stable est la paroi point de Bloch [15], aussi appelée paroi vortex [16]. Cette paroi est caractérisée par une vorticité de l'aimantation autour de l'axe du fil. Cette configuration donne lieu à un point de Bloch [17, 18], où l'aimantation est évanescente. C'est la seule singularité tri-dimensionnelle connue dans le micromagnétisme et c'est aussi un défaut topologique du point de vue de la topologie. En raison de sa vorticité, la paroi point de Bloch est caractérisée par une circulation qui peut influencer son comportement sous un stimulus.

Dans le but de développer des applications, plusieurs caractéristiques clés de la dynamique de paroi de domaines dans les fils devraient être soigneusement quantifiées. Le contrôle des propriétés des systèmes, telles que la stabilité de la paroi, sa vitesse sous un stimulus, et l'existence de l'instabilité de Walker, est crucial pour le fonctionnement optimal de dispositifs basés sur le mouvement de parois de domaines. Dans un dispositif réel, la position des parois de domaines doit être contrôlée précisément. Cela peut être réalisé en élaborant, par exemple, des centres de piégeage bien définis, que ce soit en changeant la composition du fil [19] ou en introduisant des inhomogénéités géométriques durant le processus de fabrication [20–25]. Dans le dernier cas, les modulations de diamètre de fils, synthétisées par électrodéposition, peuvent être utilisées pour contrôler la position d'une paroi de domaines en réduisant localement l'énergie de la paroi dans des régions de plus petites sections. Ainsi, les modulations de diamètres jouent le rôle de barrières de potentiel ce qui implique qu'une certaine force seuil doit être appliquée pour franchir ces barrières.

Pour les parois transverse-vortex et point de Bloch dans un fil cylindrique, des comportements très différents sous un champ ou un courant appliqué sont attendus. La dynamique de la paroi transverse-vortex est similaire à celle de la paroi transverse dans un ruban plat au-dessus de l'instabilité de Walker [11, 26, 27], avec une mobilité réduite à cause de la précession autour de l'axe du fil. En revanche, il est attendu que la paroi point de Bloch s'affranchit de l'instabilité de Walker, ce qui permet d'atteindre une vitesse de paroi de domaine très haute [28]. L'instabilité de Walker n'apparait pas dans le cas d'une paroi point de Bloch, puisque cela requerrait une énergie d'origine dipolaire trop importante.

Plusieurs études analytiques et micromagnétiques, existant dans la littérature, traitent des aspects variés du comportement de paroi de domaines dans un fil cylindrique. Ainsi, de nombreuses études ont considéré des modulations de diamètre et de composition pour le piégeage de paroi de domaines, numériquement [29–32] et analytiquement [33]. Cependant, aucun modèle théorique quantifiant clairement la force directrice de seuil comme une fonction des paramètres géométriques n'a été rapporté jusqu'à récemment. D'autres simulations micromagnétiques décrivent le comportement de la paroi point de Bloch dans des fils cylindriques parfaits sous l'action d'un champ [26, 34] ou d'un courant [35] appliqué. Certaines d'entre elles ont relevé l'existence d'un seuil au-delà duquel la circulation de la paroi point de Bloch se renverse, rendant ces structures instables sous certaines conditions particulières. Cependant, récemment, nous avons montré que la situation expérimentale est drastiquement différente [28]. Les parois point de Bloch restent stables, avec une vitesse supérieure à 600m/s, inscrivant un record expérimental pour le cas conduit purement par transfert de spin. Dans cette étude, la circulation résultante était étroitement liée au champ Œrsted généré par le courant appliqué. Ainsi, la raison de la robustesse de la paroi point de Bloch dans les expériences est attribuée au champ Œrsted azimutal, un ingrédient complétement négligé dans les simulations précédentes.

Etant donné le manque de descriptions théoriques de phénomènes critiques dans les nanofils cylindriques, dans ma thèse, j'ai fait l'effort de combiner des simulations micromagnétiques avec des descriptions analytiques, pour fournir une vue d'ensemble des paramètres clés, utiles à la prédiction et la compréhension des expériences.

Ce manuscrit est divisé en 4 chapitres incluant la description du contexte théorique, la description de notre logiciel numérique et deux chapitres résumant les résultats originaux obtenus durant ma thèse.

Le chapitre 1 introduit les notions de base de la théorie micromagnétique et l'équation Landau-Lifshitz-Gilbert (LLG) qui décrit l'évolution en temps de l'aimantation avec des termes supplémentaires correspondant aux effets induits par le courant : les effets du transfert de spin et le champ Œrsted. Le chapitre décrit aussi les deux types de paroi de domaines (paroi transverse-vortex et paroi point de Bloch) qui peuvent exister dans des nanofils magnétiquement doux et cylindrique. Enfin, il résume quelques résultats théoriques récents sur le mouvement de paroi de domaines sous l'influence d'un champ ou d'un courant appliqué connus de la littérature.

Le chapitre 2 introduit notre logiciel micromagnétique basé sur les éléments finis, feeLLGood (Finite ElEment Landau-Lifshitz-Gilbert object oriented development), et les mathématiques sous-jacentes. Le chapitre discute aussi des limites du micromagnétisme numérique.

Le chapitre 3 est dédié à l'étude analytique et numérique de la dynamique sous champ magnétique et la dynamique sous courant d'une paroi de domaines transverse dans un nanofil à section circulaire avec une modulation de diamètre. Il commence avec une description plus en profondeur du contexte du piégeage de paroi de domaines, suivi de dérivations analytiques et d'estimations numériques du champ critique et du courant critique nécessaire pour que la paroi de domaine franchisse la modulation.

Le chapitre 4 est dédié à l'étude de la dynamique sous courant d'une paroi point de Bloch dans des nanofils à section circulaire et des tubes épais. Pour motiver cette étude, un résumé bref du travail expérimental effectué dans notre laboratoire est présenté dans ce chapitre. Il s'en suit une analyse de l'instabilité d'une paroi transverse-vortex sous un courant appliqué et sa transformation en une paroi point de Bloch. Enfin, le chapitre quantifie l'impact du champ Œrsted sur la stabilité de la circulation de la paroi point de Bloch et sur la dynamique de la paroi sous un courant appliqué.

Chapitre 1

Ce chapitre décrit les éléments théoriques que j'ai utilisés pour effectuer l'étude des sujets précédemment introduits ainsi que quelques résultats généraux sur la dynamique de parois de domaines dans des nanofils.

La théorie micromagnétique repose sur l'hypothèse que l'aimantation, la densité de moment magnétique d'un matériau magnétique, peut être décrite par une fonction continue l'espace que l'on appelle champ d'aimantation $\mathbf{M}(\mathbf{r}, t)$. Il est assumé que la configuration magnétique doit varier lentement à l'échelle atomique et que la norme d'aimantation est supposée égale à l'aimantation spontanée qui dépend uniquement de la température $\|\mathbf{M}\| = M_{\mathrm{s}}(T)$. Pour trouver les configurations d'aimantation à l'équilibre, le micromagnétisme est basé sur un principe variationnel où une fonctionnelle d'énergie libre est minimisée. Cette fonctionnelle est composée de plusieurs termes dont le nombre se limitera, dans le cadre de cette thèse, à ceux jouant un rôle prédominant dans les matériaux magnétiquement doux. Une énergie d'échange qui décrit une tendance des moments magnétiques à s'aligner localement. Elle est minimale lorsque l'aimantation locale est uniforme. Une énergie démagnétisante, qui provient de l'interaction entre l'aimantation locale et le champ dipolaire associé au champ d'aimantation. Cette énergie est minimale lorsque les moments magnétiques forment une fermeture du flux magnétique. Une énergie Zeeman, qui provient de l'interaction entre l'aimantation locale et un champ magnétique appliqué (tel qu'un champ magnétique extérieur ou bien le champ Œrsted généré par un courant appliqué). Cette énergie est minimale lorsque l'aimantation locale est alignée avec le champ.

Afin de décrire la dynamique de textures magnétiques telles que des parois, on utilise une équation qui décrit l'évolution de l'aimantation, appelée équation de Landau-Lifshitz-Gilbert. Cette équation est composée de deux termes. Un premier terme décrivant un mouvement de précession de l'aimantation locale autour d'un champ effectif dérivé de la fonctionnelle d'énergie introduite précédemment. Un deuxième terme décrivant un mouvement d'amortissement de l'aimantation locale vers le champ effectif. Cette équation a été généralisée au cas d'un courant appliqué en considérant l'effet de transfert de spin, par l'ajout de deux termes appelé terme adiabatique et non-adiabatique. Cette équation a été utilisée afin de prédire les textures magnétiques stables, ainsi que leur comportement sous l'influence d'un champ magnétique et/ou d'un courant électrique. Dans mon cas, on s'intéresse la dynamique de parois de domaines dans des nanofils magnétiquement doux à section circulaire.

Il a été prédit théoriquement et observé expérimentalement qu'il existe deux types de parois dans ces fils dont la stabilité et la métastabilité dépend du diamètre du fil. Sous un seuil d'environ sept fois la longueur d'échange, la configuration la plus stable est une paroi transverse ou transverse-vortex. Cette paroi est caractérisée par une aimantation transverse par rapport à l'axe du fil, ce qui en fait un analogue de la paroi transverse dans un nanoruban plat, spécifiquement dans des petits diamètres. Pour des diamètres un peu plus larges, cette paroi commence à acquérir une vorticité par rapport à sa composante transverse. Au-dessus du diamètre seuil précédemment mentionné, la configuration la plus stable est la paroi point de Bloch, aussi appelée paroi vortex. Cette paroi est caractérisée par une vorticité de l'aimantation autour de l'axe du fil. Cette configuration donne lieu à un point de Bloch, où l'aimantation est évanescente. C'est la seule singularité tridimensionnelle connue dans le micromagnétisme et c'est aussi un défaut topologique du point de vue de la topologie. En raison de sa vorticité, la paroi point de Bloch est caractérisée par une circulation qui peut influencer son comportement sous un stimulus.

Sous l'influence d'un champ magnétique, la paroi-transverse vortex est dans un régime précessionnel dès que le champ est appliqué. Il a été prédit qu'elle se propage à une vitesse $v \propto \alpha\Delta H_{app}$ où α est l'amortissement Δ la largeur de paroi et H_{app} le champ appliqué. Pour la paroi point de Bloch, son comportement sous champ va dépendre de sa circulation. Si la circulation initiale est favorisée par le champ appliqué, alors sa vitesse est proportionnelle à $1/\alpha$. Si la circulation initiale est défavorisée, la paroi passera par une transformation qui résultera en une paroi point de Bloch avec la circulation favorisée.

Sous l'influence d'un courant, la paroi transverse-vortex est dans un régime précessionnel dès que le courant est appliqué, dans le cas où $\beta \neq \alpha$. Il a été montré à travers des simulations micromagnétiques que la vitesse de propagation a un comportement linéaire par rapport au courant appliqué (i.e. $v \propto u$). Pour une paroi point de Bloch, la circulation de la paroi influence le comportement sous courant de la paroi. Dans le cas où la circulation est favorisée par le courant, le mouvement de la paroi est stationnaire. Dans ce régime la vitesse $v \propto \frac{\beta}{\alpha}u$. Pour la circulation opposée, la paroi point de Bloch va d'abord ajuster sa configuration, résultant en un mouvement de recul. Après transformation, la paroi est maintenant caractérisée par la circulation favorisée, ce qui induit le même mouvement stationnaire prédit précédemment. Comme cela sera montré dans le chapitre 4, ce phénomène de changement de circulation peut se produire dans des fils plus gros ($> 7\ \ell_{\mathrm{ex}}$) à cause de la présence du champ Œrsted.

Chapitre 2

Ce chapitre introduit le logiciel FeLLGood que j'ai utilisé pour obtenir mes résultats. L'idée est de résoudre l'équation Landau-Lifshitz-Gilbert afin de trouver des configurations magnétiques à l'équilibre et de décrire leur dynamique sous l'influence d'un champ magnétique ou d'un courant appliqué. Cependant, pour la plupart des systèmes considérés, il n'y a pas de solution analytique au problème posé, ce qui nécessite l'usage de méthodes numériques pour le résoudre. Dans ce chapitre, j'aborde trois points: la discrétisation du problème en espace et en temps, le calcul du champ démagnétisant et la problématique liée au traitement numérique d'un point de Bloch.

D'abord, pour utiliser les méthodes numériques, le problème doit être discrétisé en espace et en temps. Pour la discrétisation en espace, il existe deux méthodes très utilisées, appelées méthodes aux différences finies et méthodes aux éléments finis respectivement. Ici je ne mentionne que la méthode des éléments finis. La méthode des éléments finis est utilisée pour résoudre des problèmes impliquant des équations différentielles. Elle est basée sur une reformulation sous forme faible du problème. C'est à dire qu'au lieu de résoudre directement l'équation Landau-Lifshitz-Gilbert, cette équation va être projetée sur une base de fonctions test, puis intégrée sur tout le domaine. Les fonctions test sont choisies de manière à préserver les propriétés du problème. Dans notre cas, la norme de l'aimantation doit être préservée. C'est pour cette raison que le mathématicien Alouges a proposé de choisir l'espace des fonctions test comme étant le plan tangent à l'aimantation [36]. Pour résoudre le problème, il va donc falloir évaluer des intégrales sur tout le domaine. Pour cela, la méthode repose sur une discrétisation spatiale en sous-domaines appelés éléments finis. On distingue les éléments de volumes des éléments de frontières. Ces éléments sont généralement des tétraèdres qui permettent de bien approximer des formes curvilinéaires tel que des fils ou des tubes ainsi que des formes plus complexes telles que des modulations géométriques. La solution du problème est approximée par une fonction résultant de l'interpolation de fonctions de base (dans notre cas des polynomes de Lagrange dit P1) définies sur chaque élément. Il en résulte que l'intégrale sur le domaine peut être décomposée en une somme d'intégrales élémentaires sur chaque élément. On considère ici des éléments dits affines, que l'on peut transformer en un élément de référence. En transformant chaque élément (ainsi que les fonctions de bases qui leur sont associées) en cette élément de référence, nous pouvons évaluer chaque intégrale élémentaire en utilisant la quadrature de Gauss-Legendre. Il en résulte un système d'équations linéaires (un pour chaque élément) qui est transformé sous forme matricielle. Les matrices élémentaires sont ensuite assemblées de telle sorte qu'elles forment une matrice creuse. Il en résulte donc un système d'équations linéaires représentant le système entier qui est résolu en utilisant la méthode itérative du gradient bi-conjugué.

Pour la discrétisation en temps, l'idée est de diviser le temps de simulation en pas de temps k. Ce pas de temps peut être fixe ou adaptatif. L'aimantation est ensuite calculée à chaque pas de temps. On note $\mathbf{m}^n$ et $\mathbf{m}^{n+1}$ le champ d'aimantation évalué aux instants nk et $(n+1)k$ respectivement. Le calcul de $\mathbf{m}^{n+1}$ peut être fait en utilisant un développement de Taylor tronqué au terme d'ordre p au temps nk ce qui donne $\mathbf{m}^{n+1} = \mathbf{m}^n + O(k^p)$. On dit alors que ce schéma temporel est précis jusqu'à l'ordre p avec une erreur locale $O(k^{p+1})$. C'est pourquoi afin de calculer $\mathbf{m}^{n+1}$, nous devons estimer la dérivée temporelle qui au premier ordre correspond à $\partial_t \mathbf{m}^n$ qui est obtenue en résolvant le problème de l'équation Landau-Lifshitz-Gilbert. Il est souvent intéressant d'essayer d'augmenter l'ordre du schéma temporel afin de pouvoir utiliser un pas de temps plus grand en ayant la même précision, réduisant le temps de simulation. Cependant, l'augmentation de l'ordre du schéma peut être difficile, car le schéma peut devenir instable. L'augmentation vers l'ordre deux du schéma temporel de FeeLLGood n'est pas décrite en détail dans cette thèse mais est exposée dans l'article [37]. Plus de détails sur le logiciel sont exposés sur le site [38].

Ensuite, il y a le calcul du champ démagnétisant. La méthode de calcul du champ démagnétisant implémentée dans le logiciel est la méthode multipolaire rapide. L'idée est de créer une structure en arbre où l'on va diviser successivement le domaine de calcul en sous-domaines appelés boites (quatre pour le cas 2D et huit pour le cas 3D) jusqu'à un niveau appelé niveau feuille. Le nombre de niveaux est déterminé par le nombre de noeuds du maillage (ici les sommets des tétraèdres). L'idée est alors de calculer pour chaque niveau, le potentiel magnétostatique généré au centre de chaque boite dite cible par des boites dites sources, bien-séparées (un minimum d'une boite d'écart avec la boite cible), en utilisant l'approximation du champ lointain. On exprime alors le potentiel comme une expansion multipolaire. L'idée est alors de récupérer le calcul du potentiel pour chaque niveau en utilisant des translations d'expansions inter-niveaux afin de réduire la complexité de l'algorithme.

Enfin, il y a la problématique liée au traitement numérique d'un point de Bloch. Le micromagnetisme est basée sur la définition du champ continu d'aimantation dont la norme est supposée constante. Il n'est donc pas possible mathématiquement de décrire une singularité telle que le point de Bloch où l'aimantation est évanescente. Dans la méthodes des éléments finis, la contrainte sur la norme de l'aimantation est imposée aux noeuds du maillages. Dans chaque éléments de volumes, l'aimantation est interpolée linéairement, avec une norme pouvant être grandement réduite. Cela permet l'existence d'un point de Bloch à l'intérieur d'un élément. Ainsi sous l'influence d'un champ ou d'un courant, le point de Bloch va pouvoir se déplacer d'éléments en éléments moyennant un coup en énergie qui se manifeste par une force de friction artificielle qui dépend de la taille du maillage. Cela peut provoquer le piégeage du point de Bloch dans le maillage. Pour cette raison, j'ai considéré deux cas: celui d'un fil et celui d'un tube épais. Strictement parlant, il n'y a plus de point de Bloch au sein du tube épais pour une paroi point de Bloch, c'est pour cela que nous le référons à paroi pseudo point de Bloch. Ce type de paroi est appelé paroi vortex dans la littérature. La différence principale entre cette paroi et la paroi point de Bloch est l'absence du point de Bloch dans le cas du tube. J'ai comparé leur structure et leur dynamique. Il en résulte que leur structure à la surface est très similaire mais à l'intérieur du volume, elles diffèrent.

Chapitre 3

Ce chapitre concerne l'étude du piégeage d'une paroi transverse dans un nanofil à section circulaire présentant une modulation de diamètre. Cela s'inscrit dans le contexte du contrôle de la position de parois de domaines dans des nanofils pour les applications mémoires. En effet, il est possible de modifier le paysage énergétique du fil afin de créer des régions agissant comme des puits de potentiel dans lesquels les parois vont se stabiliser, appelées sites de piégeages. Cela éviterait que lorsque les parois sont déplacées elles ne s'annihilent entre elles, ce qui conduirait à des pertes de données.

Il existe essentiellement deux manières de créer ces sites de piégeage. La première consiste à créer des modulations géométriques comme une variation locale de diamètre ou, plus exotique, une variation comme l'alternance de fils et de tubes. La seconde consiste à créer une alternance de matériaux. Cette thèse se restreint à l'étude d'une modulation de diamètre d'un fil.

Il existe dans la littérature des études micromagnétiques de modulations de diamètres. Cependant, les processus de nucléation aux bords du fil et de passage de la paroi à travers la modulation ne sont pas étudiés séparément, décrivant succinctement le dernier. Dans cette étude, je présente une dérivation de modèles analytiques pour décrire comment une paroi de domaines pourrait franchir la modulation de diamètre dans un nanofil à section circulaire, sous l'influence d'un champ magnétique ou d'un courant polarisé en spin. Les lois d'échelles obtenues dans ce chapitre pourraient guider les expérimentateurs dans l'élaboration de modulations ayant les propriétés désirées.

J'ai examiné deux cas: une modulation abrupte et une modulation douce. Pour chaque cas, j'ai calculé analytiquement la valeur seuil du champ magnétique appliqué et du courant appliqué comme une fonction des paramètres géométriques. La pertinence de ces résultats analytiques a été confirmée par des simulations micromagnétiques, qui révèlent un accord quantitatif pour chaque modulation géométrique. J'ai obtenu des expressions de courants seuils qui sont proportionnelles aux champs seuils, à la largeur de paroi Δ, au facteur $R^2(z)/R_1^2$ provenant de la conservation du courant, et à l'aimantation spontanée Ms. Indépendamment du type de modulation, le courant critique augmente bien plus rapidement en fonction de la différence des diamètres que le champ critique. Cela est lié à la décroissance de la densité locale de courant, ainsi que l'augmentation de la taille de la paroi. De plus, si nous comparons les modulations abruptes et douces, les seuils critiques dans le premier cas augmente plus rapidement que dans le deuxième cas. En d'autres termes, le piégeage semble plus efficace avec une modulation abrupte.

Chapitre 4

Nous avons rapporté récemment le rôle clé joué par le champ Œrsted dans des nanofils cylindriques, magnétiquement doux, dans la stabilisation des parois point de Bloch atteignant une vitesse $> 600\,\mathrm{m}\cdot\mathrm{s}^{-1}$ sous l'influence du transfert de spin [28].

Utilisant des simulations micromagnétiques, j'ai considéré une paroi transverse-vortex sous l'influence du champ Œrsted et montré qu'il se transforme en une paroi point de Bloch avec la même circulation que le champ. Cette transformation est caractérisée par le mouvement du vortex et de l'anti-vortex qui constitues la paroi, de l'un vers l'autre. Il s'en suit alors leur annihilation qui injecte un point de Bloch (préservant la polarité de la paroi) à l'intérieur du volume. Le courant seuil qui déclenche cette transformation est d'un ordre de grandeur inférieur à celui des courants utilisés dans l'expérience [28]. Cela montre que le champ Œrsted stabilise la paroi point de Bloch.

J'ai considéré une paroi point de Bloch sous l'influence du champ Œrsted pour chaque circulation. Pour chaque cas, l'aimantation dans les domaines tend à s'aligner avec le champ. Lorsque la circulation de la paroi point de Bloch est la même que le champ, la largeur de la paroi augmente jusqu'à atteindre un maximum. Lorsque la circulation est opposée à celle du champ, la paroi se contracte jusqu'à ce qu'elle atteigne une largeur minimale. Si le courant est supérieur à un seuil, la paroi se transforme en une paroi point de Bloch avec une circulation opposée. Nous avons montré que le courant seuil est du même ordre que celui de l'expérience [28], ce qui montre que le champ Œrsted joue le rôle principale dans le phénomène de renversement de circulation observé. Ce seuil semble suivre une dépendance en $1/R^3$ et devrait s'appliquer pour les matériaux doux.

Concernant, le mécanisme de renversement de circulation, il ne s'agit pas d'un renversement cohérent du champ d'aimantation, mais il implique la création et l'annihilation de paires vortex-anti-vortex et de points de Bloch. Malgré cette complexité, le type des objets qui apparaissent durant la transformation doit respecter une certaine règle topologique résultant de la continuité du champ d'aimantation. Ce qui veut dire, que le changement du nombre d'enroulement associé à la surface correspond au changement du nombre d'enroulement associé au volume.

Par ailleurs, le renversement de circulation se produit également pour la paroi pseudo point de Bloch pour un courant seuil légèrement plus haut que celui de la paroi point de Bloch. Le mécanisme de renversement est plus complexe à cause à la présence de la surface interne du tube qui permet la création et l'annihilation de pairs vortex-anti-vortex et de points de Bloch.

Finalement, concernant la vitesse de la paroi de domaine, elle est largement déterminée pas l'effet de transfert de spin pour le cas d'une paroi point de Bloch avec la même circulation que celle du champ Œrsted.

Conclusion et perspectives

Pour conclure, ce manuscrit présente une étude théorique sur la dynamique sous courant de parois de domaines, et leurs phénomènes critiques associés, dans deux types de nanofils à section circulaire. J'ai combiné des calculs analytiques et des simulations micromagnétiques réalisées avec notre propre logiciel FeeLLgood. Le chapitre 3 est focalisé sur le comportement d'une paroi transverse dans la région de plus petit diamètre d'un nanofil présentant une modulation locale de diamètre. Une telle modulation agit comme une barrière de potentiel, ce qui implique qu'une force motrice seuil doit être appliquée pour franchir la barrière. Nous avons calculé analytiquement la valeur seuil à la fois pour un champ magnétique appliqué et pour un courant appliqué, comme une fonction des paramètres géométriques. Le modèle analytique développé est une simple loi d'échelle, qui pourrait être utile dans la résolution de problèmes expérimentaux et de nanofabrications.

Alors que le chapitre 3 traite une seule modulation (une partie d'une protrusion géométrique) pour établir la base du phénomène de piégeage, des investigations plus approfondies devraient être focalisées sur une protrusion et plusieurs protrusions, ce qui serait pertinent pour les applications. Dans un travail récent, concernant juste un champ appliqué avec une protrusion [39], nous avons montré que la longueur de la protrusion est un paramètre clé supplémentaire qui pourrait influencer les conditions de piégeage. Cette étude devrait être poursuivie et généralisée pour le cas d'un courant appliqué.

Alors que le contrôle de la position d'une paroi de domaines peut être fait en utilisant des modulations géométriques étudiées dans ce manuscrit, d'autres alternatives et des contraintes de nanofabrication sont discutées dans la littérature. Par exemple, plusieurs études sont dédiées à des fils segmentés avec une alternance de matériaux ferromagnétiques différents ou des géométries cylindriques comme une alternance de segments de tube et de fil. Chaque situation offre une liste de questions ouvertes devant être étudiées théoriquement. Une généralisation plus approfondie impliquerait des fils avec plusieurs protrusions et parois de domaines, et un réseau de ces nanofils. Il a été montré pour les nanorubans que les parois de domaines interagissent entre elles quand elles sont soit dans des fils adjacents soit dans le même fil. Aussi, le champ Œrsted généré par les fils adjacents devrait être considéré. La considération de ces aspects est nécessaire pour atteindre de hautes densités de stockage dans les applications mémoires.

Un autre phénomène devant être considéré serait le comportement des parois point de Bloch en présence de modulations de diamètre et de paramètres matériaux. Ces textures magnétiques, naturellement plus stable dans les fils à larges diamètres, sont particulièrement intéressante pour la réduction du champ de fuite généré, un effet non désirable dans les réseaux denses de fils. De plus, la paroi point de Bloch démontre une dynamique rapide, cruciale pour des enregistrements à haute vitesse et inaccessible dans des systèmes avec des paroi transverses tel que les fils à section circulaire de petits diamètres. Cependant, le diamètre minimum requis pour stabiliser la paroi point de Bloch ($> 7\ \ell_{\mathrm{ex}}$), implique qu'un compromis doit être trouvé entre la densité de stockage et la vitesse d'opération de l'application mémoire. Le chapitre 4 présente une étude théorique de l'impact du champ d'Œrsted et du transfert de spin sur une paroi point de Bloch dans un fil cylindrique. Cette étude a partiellement été motivée par notre travail récent [28], dans lequel nous rapportons le rôle clé joué par le champ d'Œrsted dans la stabilisation des parois point de Bloch, qui sont capable t'atteindre des vitesses jusqu'à $> 600\,\mathrm{m}\cdot\mathrm{s}^{-1}$ sous un courant appliqué.

Durant cette thèse, j'ai utilisé des simulations micromagnétiques, de la modélisation analytique et des arguments de topologie pour comprendre en détail et quantitativement les phénomènes sous-jacents. En particulier le renversement de circulation de négative à positive d'une paroi point de Bloch par rapport au courant appliqué. Le résultat principal est la dépendance en $1/R^3$ du courant seuil de renversement, avec R le rayon du fil, avec l'effet du champ Œrsted qui prédomine pour un rayon au-dessus de 30 nm. Inversement, la vitesse des parois reste largement déterminée par le transfert de spin seul, dans un régime stationnaire (sous courant de Walker). Grace à la renormalisation des longueurs et des densités de courant, le résultat peut être appliqué pour des fils fait d'un matériau magnétiquement doux.

Nous sommes conscients que la dynamique des points de Bloch dans les simulations micromagnétique doit être traitée avec prudence. Une manière de redéfinir le traitement numérique de la dynamique de point de Bloch pourrait être l'usage d'un modèle multi-échelle où les approches atomistiques et continues sont fusionnées. La comparaison entre chaque méthode numérique pourrait aider à quantifier les limites de la modélisation purement micromagnétique de la dynamique sous courant d'une paroi point de Bloch.

Un autre problème important est lié à l'imagerie expérimentales des parois point de Bloch (et autres textures magnétiques). Par exemple, plusieurs méthodes pour la caractérisation nanoscopique dans l'espace direct (i.e. l'image) sont en développement à SPINTEC (X-ray Magnetic Dichroism, Magn. Force Imaging, Electron Holography etc) et utilisant des équipements internationaux (Time-resolved X-ray imaging, Vectorial Field tomography with electrons). Jusqu'à maintenant, chaque développements (les outils théoriques sophistiqués et les instruments expérimentaux couteux) ne profitent pas efficacement de chacun d'eux et de comparaisons précises. Dans ce contexte, des efforts devraient être fait pour convertir les sorties usuelles de FeLLGood en sorties compatibles avec celles des expériences d'imageries en utilisant un module extérieur à notre logiciel.

En plus des fils fait d'un matériau, le progrès continu de la nanofabrication donne lieu à une nouvelle variété de géométries cœur-coquille multicouches. Dans le cas d'un cœur fait de métal lourd avec un couplage spin-orbite fort, l'injection directe d'électrons polarisés en spin à l'intérieur de la coquille, ferromagnétique, due à l'effet Hall de spin permettrait la possibilité de combiner l'efficacité du couple spin-orbite avec les hautes vitesses de paroi de domaines à l'intérieur du même objet. Ce type de système requerra l'extension du modèle physique utilisé dans la version actuelle de notre logiciel.

Contents

List of Abbreviations

BPW	Bloch-Point Wall
DW	Domain wall
FM	Ferromagnet(ic)
LLG	Landau-Lifshitz-Gilbert
STT	Spin-transfer torque
TVW	Transverse Vortex Wall
XMCD	X-ray magnetic circular dichroism
PEEM	photo-emission electron microscopy

List of Symbols

A	Exchange constant	$\mathrm{J\ m^{-1}}$
E_d	Demagnetizing energy	J
E_ex	Exchange energy	J
$E_\mathrm{Œ}$	Œrsted energy	J
E_tot	Total energy	J
E_z	Zeeman energy	J
$\mathbf{H}_\mathrm{d}$	Demagnetizing field	$\mathrm{A \cdot m^{-1}}$
$\mathbf{H}_\mathrm{eff}$	Effective field	$\mathrm{A \cdot m^{-1}}$
$\mathbf{H}_\mathrm{ex}$	Exchange field	$\mathrm{A \cdot m^{-1}}$
$\mathbf{H}_\mathrm{ext}$	External field	$\mathrm{A \cdot m^{-1}}$
$\mathbf{H}_\mathrm{K}$	Anisotropy field	$\mathrm{A \cdot m^{-1}}$
$\mathbf{H}_\mathrm{Œ}$	Œrsted field	$\mathrm{A \cdot m^{-1}}$
$\mathbf{J}$	Current density	$\mathrm{A \cdot m^{-2}}$
J_c	Critical current density	$\mathrm{A \cdot m^{-2}}$
K_{eff}	Effective anisotropy constant	$\mathrm{J\ m^{-3}}$
K_u	Uniaxial anisotropy constant	$\mathrm{J\ m^{-3}}$
ℓ_ex	Exchange length	m
$\mathbf{M}$	Magnetization	$\mathrm{A \cdot m^{-1}}$
$\mathbf{m}$	Reduced magnetization	$\mathrm{A \cdot m^{-1}}$
M_s	Spontaneous magnetization	$\mathrm{A \cdot m^{-1}}$
N_{sk}	Topological charge or skyrmion number	
P	Spin polarization rate	
p	Core polarity number	
w_{S^1}	Winding number	
w_{S^2}	Winding number	
α	Gilbert damping	
β	Non-adiabatic term	
γ_0	Gyromagnetic ratio	$\mathrm{Hz \cdot T^{-1}}$
Δ	Domain wall width	m
ε_d	Demagnetizing energy density	$\mathrm{J \cdot m^{-3}}$
ε_ex	Exchange energy density	$\mathrm{J \cdot m^{-3}}$
$\varepsilon_\mathrm{Œ}$	Œrsted energy density	$\mathrm{J \cdot m^{-3}}$
ε_tot	Total energy density	$\mathrm{J \cdot m^{-3}}$
ε_z	Zeeman energy density	$\mathrm{J \cdot m^{-3}}$
μ_B	Bohr magneton	$\mathrm{J \cdot T^{-1}}$
μ_0	Vacuum magnetic permeability	$4\pi \times 10^{-7}\ \mathrm{T\ A^{-1}\ m}$
e	Electron charge	C
m_e	Electron mass	kg
τ_c	Characteristic time of BPW circulation switching	s

Introduction

Context

Over the last decades, a great interest has arisen for magnetic conduits in the field of spintronics. These structures allow the study of a variety of phenomena such as magnetic textures formation, magnetization dynamics under applied current and spin-waves propagation. Due to the interaction between magnetization and electron spins, these conduits are good candidates for the development of applications such as magnetic memory [1], spin logic [2] and more recently, neuromorphic devices [3].

One of the most investigated phenomenon in spintronics, both experimentally and theoretically, is the domain wall motion. The initially considered domain wall motion under an applied magnetic field [4, 5] has been extended since the early 2000's to the current-driven cases, based on the spin-transfer effects [6], and more recently to spin-orbit-torques-driven cases [7] and other effects such as heat gradients [8], strain [9], spin waves [10] etc. Common features of motion under both field and current are the steady-state propagation under low stimulus as well as a precessional regime above a threshold, with a crossover process called the Walker breakdown. This regime leads to undesirable magnetization oscillations or to chaotic changes of the internal degrees of freedom of domain walls.

Until recently, flat nanostrips with domain walls have been the most investigated type of conduits, due to well-established fabrication techniques such as lithography. Extensive studies were conducted on the motion of the domain walls inside magnetically soft patterned nanowires under applied field or current [11, 12]. However, technological constraints related to the integration of such 2D nanostructures into a real device raise an interest for natural 3D nanostructures [13], for example cylindrical nanowires and tubes. These geometries are now available for experimental studies due to the advances in fabrication techniques [14].

The extension of 2D nanostructures into three dimensions gives rise to unconventional spin textures, in which novel physical effects related to geometry, topology and chirality are involved. For instance, two types of domain walls are found to be stable or metastable depending on the wire diameter [15]. Below a threshold of about seven times the exchange length, the most stable configuration is found to be a transverse or transverse-vortex wall. This wall is characterized by a transverse magnetization component with respect to the wire axis, making it analog to the transverse wall in a flat strip, specifically at low diameters. For slightly larger diameters, this wall starts to acquire a curling with respect to its transverse component. Above the previously mentioned diameter threshold, the most stable configuration is the Bloch-point wall (BPW) [15], also called vortex wall [16]. This wall is characterized by a curling of magnetization around the wire axis. This configuration leads to the presence of a Bloch-point [17, 18], where the magnetization vanishes. It is the only three-dimensional singularity known in micromagnetism and is also a topological defect from the point of view of topology. Due to its curling, the BPW is characterized by a circulation which may dictates its behavior under a stimulus.

In order to develop applications, several key features of the domain wall dynamics in the wires should be carefully quantified. The control of system properties such as the domain wall stability, its speed under the external stimulus, and the existence of the Walker breakdown, is crucial for the optimal functioning of the domain-wall-based device. In a real device, the domain wall position must also be precisely controlled. This can be achieved for example by designing well-defined pinning centers, whether by changing the composition of the wire [19] or by introducing geometrical inhomogeneities during the fabrication process [20–25]. In the latter case, diameter modulations of the nanowire synthesized by electrodeposition can be used to control the domain wall position by locally reducing its magnetostatic and exchange energies in the smaller cross-sectional parts. Thus, diameter modulations play the role of a potential barrier which implies that some threshold driving force must be applied to overcome the barrier.

Transverse-vortex walls and Bloch-point walls in a cylindrical wire are expected to have very different behaviors under an applied field or an applied current. The dynamics of the transverse-vortex wall is similar to that of a transverse wall in a flat strip above the Walker breakdown [11, 26, 27], with a low mobility due to its precession around the wire axis. In contrast, the Bloch-point wall is expected to prevent the usual Walker breakdown, and thus enable a very high domain wall speed [28]. The Walker breakdown does not occur in the case of the Bloch-point wall, as it would require too large a dipolar-origin energy.

Several analytical and micromagnetic studies exist in the literature which treat various aspects of the domain wall behavior in a cylindrical wires. Thus, several studies considered diameter and composition modulations for the domain wall pinning numerically [29–32] and analytically [33]. However, no theoretical model quantifying clearly the threshold driving force as a function of geometric parameters has yet been reported until recently. Other micromagnetic simulations described the Bloch-point wall behavior in perfect cylindrical nanowires under an applied field [26, 34] or current [35]. Some of them have pointed out the existence of the threshold above which the Bloch-point wall circulation switch making these structures unstable under some particular conditions. However, recently, we showed that the experimental situation is drastically different [28]. Bloch-point walls remain stable and with speed exceeding 600m/s, setting an experimental record for a purely spin-transfer-driven case. In this study, the resulting circulation was closely related to the Oersted field generated by the applied current. Thus, the reason for the robustness of the BPW in the experiments was attributed to the azimuthal Œrsted field, an ingredient completely disregarded in previous simulations.

Given the lack of theoretical description of critical phenomena in cylindrical nanowires, in my PhD thesis I made an effort to combine micromagnetic simulations with analytical descriptions, to provide an overview of key parameters, useful in predicting and understanding experiments.

Manuscript outline

This manuscript is divided into 4 chapters including the description of the theoretical background, the description of our numerical software and two chapters summarizing original results obtained during my thesis.

Chapter 1 introduces the basic notions of the micromagnetic theory and the so-called Landau-Lifshitz-Gilbert (LLG) equation describing the magnetization evolution in time with additional terms corresponding to the current-induced effects: spin-transfer effects and the Œrsted field. The chapter also describes the two types of the domain wall (transverse-vortex wall and Bloch-point wall) that may exist inside magnetically soft cylindrical nanowires. Finally, it summarizes some recent theoretical results on the domain wall motion under either an applied magnetic field or an applied current knowing from the literature.

Chapter 2 introduces our micromagnetic finite element based software feeLLGood (Finite ElEment Landau-Lifshitz-Gilbert object oriented development) and the underlying mathematics. The chapter also discusses the limits of numerical micromagnetism.

Chapter 3 is dedicated to the analytical and micromagnetical study of the magnetic field-driven dynamics and current-driven dynamics of a transverse domain wall in a circular cross section nanowire with a single modulation in diameter. It starts with a more in-depth description of the context of domain wall pinning and follows with the analytic derivations and numerical estimations of both the critical field and the critical current necessary for the domain wall to pass the modulation.

Chapter 4 is dedicated to the study of the current-driven dynamics of a Bloch-point wall in circular cross section nanowires and thick-walled nanotubes. As a motivation of this study, a brief summary of the experimental work done in our laboratory presented in this chapter. It is followed by an analysis of the instability of the transverse-vortex wall under the applied current and its transformation into a Bloch-point wall. Finally, chapter quantifies the impact of the Œrsted field on the BPW circulation stability and BPW dynamics under applied current.

Chapter 1

Micromagnetism and domain walls

1.1 Elements of micromagnetism

Ferromagnetic materials exhibit a wide variety of phenomena. One of them is the existence of magnetic domains separated by boundaries, also called domain walls. At first, these domain walls were considered as objects with no thickness in the framework of the domain theory. Later, Brown showed the limits of this theory, which is unable to describe the internal structure of the magnetic domain walls [40]. He initiated the micromagnetic theory which gives us a framework to study these magnetic structures at the sub-micrometer scale. Because domain walls are characterized by a width which generally extends to tens of nanometers, the atomic scale is not relevant for the study of the motion of domain walls. Hence, this theory relies on the continuum approximation which discards the atomic structure. The magnetic configuration of a ferromagnet is therefore described by a continuous vector field $\mathbf{M}(\mathbf{r}, t)$ whose the norm corresponds to the local average of magnetic moments, the magnetization. This magnetization field is constrained by certain assumptions: The magnetic configuration should be varying slowly at the atomic scale and the norm is supposed to be equal to the spontaneous magnetization which depends only on temperature, thus $\|\mathbf{M}\| = M_\mathrm{s}(T)$. For convenience, we define the unit magnetization field as $\mathbf{m}(\mathbf{r}, t) = \mathbf{M}(\mathbf{r}, t)/M_\mathrm{s}$.

1.1.1 Micromagnetic energies

In order to find the equilibrium configurations of magnetization, micromagnetism is based on a variational principle where a free-energy functional is minimized. This energy functional is composed of several terms. In this section, we limit ourselves to the definition of the energy densities that play a predominant role in magnetically soft materials.

Exchange energy

In a ferromagnet, neighboring spins tend to align along the same direction. This is due to Coulomb's repulsion of two neighboring electrons, usually on neighboring atoms, acting in conjunction with Pauli's principle, which forbids the two electrons to enter the same quantum state. The exchange energy is derived from the Heisenberg exchange model [41] using classical vectors in the limits of infinitesimal rotations of spins. The resulting energy density is

$$\varepsilon_\mathrm{ex} = A \sum_i \left(\boldsymbol{\nabla} m_i\right)^2 , \tag{1.1}$$

where $i = x, y, z$. This energy density is minimized when the magnetization is locally aligned along one direction.

Demagnetizing energy

Magnetization generates a magnetic field over the whole space. This magnetic field can be separated into two contributions. A field defined inside the material, usually called demagnetizing field $\mathbf{H}_\mathrm{d}$, and a field defined outside the material, usually called stray field. The former got its name from the fact that this field tend to be opposed to the magnetization field. From classical electrodynamics, we define the demagnetizing energy as follows:

$$\varepsilon_\mathrm{d} = -\frac{\mu_0 M_\mathrm{s}}{2}\,\mathbf{H}_\mathrm{d} \cdot \mathbf{m}. \tag{1.2}$$

The factor 1/2 is here to avoid counting interactions twice. This energy is considered to be the hardest to calculate since the demagnetizing field is non local. The expression for the field is derived from the following Maxwell equations:

$$\nabla \cdot \mathbf{B} = 0, \tag{1.3}$$

$$\nabla \times \mathbf{H} = 0, \tag{1.4}$$

where $\mathbf{B}$ is the magnetic induction which is related to the magnetic field $\mathbf{H}$ by:

$$\mathbf{B} = \mu_0(\mathbf{H} + \mathbf{M}). \tag{1.5}$$

We can solve equation (1.5) and (1.4) with:

$$\mathbf{H} = -\nabla \varphi_m, \tag{1.6}$$

where φ_m is a scalar potential, we call magnetostatic potential, which is the solution to the equation:

$$\Delta \varphi_m = \nabla \cdot \mathbf{M}. \tag{1.7}$$

One common way to write this potential is to use the concept of fictious magnetic charge densities where $\rho_\mathrm{m} = -\nabla \cdot \mathbf{M}$ is the volume charge density and $\sigma_\mathrm{m} = \mathbf{M} \cdot \mathbf{n}$ is the surface charge density (where $\mathbf{n}$ is the outward-pointing normal to the surface of the system) [42]. This gives the following expression:

$$\varphi_\mathrm{m}(\mathbf{r}) = \int \frac{\rho_\mathrm{m}(\mathbf{r}')}{4\pi|\mathbf{r} - \mathbf{r}'|} d^3\mathbf{r}' + \oint \frac{\sigma_\mathrm{m}(\mathbf{r}')}{4\pi|\mathbf{r} - \mathbf{r}'|} dS'. \tag{1.8}$$

In simple cases, this energy density can be minimized using the pole avoidance principle. It states that magnetization will tends to avoid the formation of magnetostatic charges. This is usually achieved by the formation of a flux closure distribution.

Zeeman energy

When a magnetic moment interacts with an external magnetic field $\mathbf{H}_\mathrm{ext}$, it tends to align with it [42]. The resulting energy density often called Zeeman energy density is:

$$\varepsilon_\mathrm{z} = -\mu_0 M_\mathrm{s}\,\mathbf{H}_\mathrm{ext} \cdot \mathbf{m}. \tag{1.9}$$

This energy density is minimized when the magnetization is aligned with the magnetic field.

Œrsted energy

In the present thesis, we consider an electric current passing through the wire. It generates a magnetic field $\mathbf{H}_{\text{Œ}}$ also called Œrsted field. Its expression can be derived from the integral form of the Maxwell-Ampere equation

$$\oint_{\partial\Sigma} \mathbf{H}_{\text{Œ}} \cdot \mathrm{d}\ell = \iint_{\Sigma} \mathbf{J}_{\mathrm{f}} \cdot \mathrm{d}\mathbf{S}, \tag{1.10}$$

where $\mathbf{J}_{\mathrm{f}}$ is the free current passing through the surface Σ and $\partial\Sigma$ is the contour of this surface. In a system with cylindrical symmetry (a tube or a wire for example), we define the cylindrical coordinates (ρ, φ, z) with respect to its vector base $\{\hat{\mathbf{e}}_\rho, \hat{\mathbf{e}}_\varphi, \hat{\mathbf{e}}_z\}$. Since the system has a rotational invariance, the Œrsted field is oriented along the azimuth which corresponds to the $\hat{\mathbf{e}}_\varphi$ direction. As a result:

$$\mathbf{H}_{\text{Œ}} = H_{\text{Œ}} \hat{\mathbf{e}}_\varphi. \tag{1.11}$$

Considering a uniform and steady current, the Œrsted field expression for a tube of internal radius R_{i} and external radius R is:

$$H_{\text{Œ}}(\rho) = \frac{J\rho}{2}\left(1 - \frac{R_{\mathrm{i}}^2}{\rho^2}\right), \tag{1.12}$$

for $R_{\mathrm{i}} < \rho < R$. From this field we can also define an Œrsted energy density similar to a Zeeman energy density

$$\varepsilon_{\text{Œ}} = -\mu_0 M_{\mathrm{s}} \mathbf{H}_{\text{Œ}} \cdot \mathbf{m}. \tag{1.13}$$

Thus, this energy density is minimized when the magnetization is aligned with the Œrsted field.

1.1.2 Equilibrium conditions

In order to find the equilibrium configurations, one way is to first define an energy functional for the system resulting from the previous energies. In our case we consider magnetically soft materials such as permalloy for 1D structure, thus any source of anisotropy is considered neglectable compare to the dipolar energy. As a result the energy functional reads as:

$$E_{\mathrm{tot}}[\mathbf{m}] = \int \left(A \sum_i (\boldsymbol{\nabla} m_i)^2 - \mu_0 M_{\mathrm{s}} \mathbf{H}_{\text{Œ}} \cdot \mathbf{m} - \frac{\mu_0 M_{\mathrm{s}}}{2} \mathbf{H}_{\mathrm{d}} \cdot \mathbf{m} \right) \mathrm{d}V. \tag{1.14}$$

The equilibrium state corresponds to the configuration of magnetization field that minimizes locally this energy functional:

$$\delta E[\mathbf{m}] = 0 \tag{1.15}$$

$$\delta^2 E[\mathbf{m}] > 0. \tag{1.16}$$

1.2 Magnetization dynamics

In this section we introduce the equation that drives magnetization under the influence of either a magnetic field or a spin polarized current.

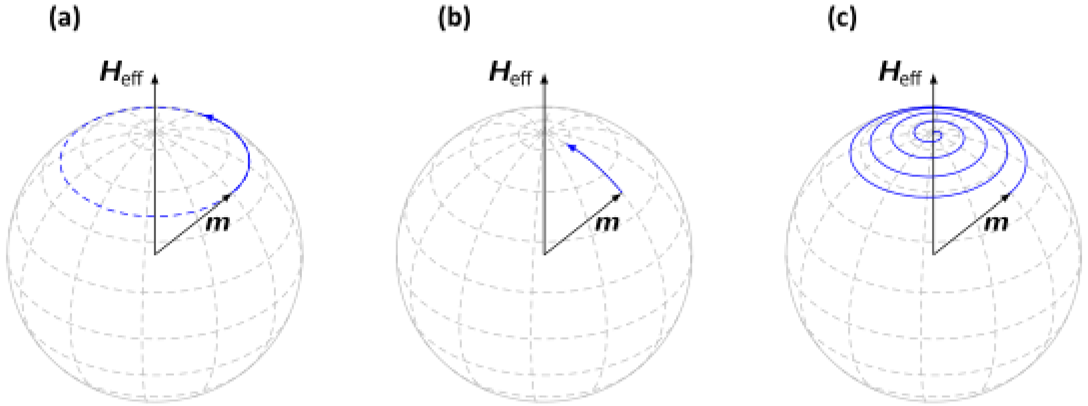

Figure 1.1: Evolution of local magnetization described by the Landau-Lifshitz-Gilbert equation. (a) The precession around the effective field, (b) the damped motion toward the effective field and (c) the motion including both precession and damping. Adapted from [43].

1.2.1 Magnetic field-driven dynamics

The equation that governs the magnetization dynamics is the Landau-Lifshitz-Gilbert equation [44]:

$$\frac{\partial \mathbf{m}}{\partial t} = -\gamma_0 \mathbf{m} \times \mathbf{H}_{\text{eff}} + \alpha \mathbf{m} \times \frac{\partial \mathbf{m}}{\partial t}, \tag{1.17}$$

where $\gamma_0 = \mu_0|\gamma|$ with γ, the gyromagnetic ratio, and α, the Gilbert damping parameter.

The first term referred as "precessional term" corresponds to the precession of magnetization around an effective field (Fig. 1.1 (a)). This effective field is derived from the total energy density ε by the relation

$$\mathbf{H}_{\text{eff}} = -\frac{1}{\mu_0 M_{\text{s}}} \frac{\delta \varepsilon}{\delta \mathbf{m}}. \tag{1.18}$$

The second term introduced phenomenologically takes into account the energy dissipation of the system that manifests as a damped motion of the magnetization toward the effective field (Fig. 1.1 (b)). It is often referred as "damping term". The combination of these two terms gives the kind of motion represented Fig. 1.1 (c).

The LLG equation has an interesting property with respect to energy. The time derivative of the total energy reads as:

$$\dot{E}_{tot} = \int \frac{\delta \varepsilon}{\delta \mathbf{m}} \cdot \frac{\partial \mathbf{m}}{\partial t} \, dV, \tag{1.19}$$

which corresponds to

$$\dot{E}_{tot} = -\frac{\alpha \mu_0 M_{\text{s}}}{\gamma_0} \int \left(\frac{\partial \mathbf{m}}{\partial t} \right)^2 dV. \tag{1.20}$$

This expression shows that it always reduces the total energy over time. This is the reason why the LLG equation can be used to find equilibrium states by starting with a reasonable guess. This is what has been done in this thesis. It also shows that if there is no dissipation ($\alpha = 0$), the energy will be conserved :

$$\dot{E}_{tot} = 0. \tag{1.21}$$

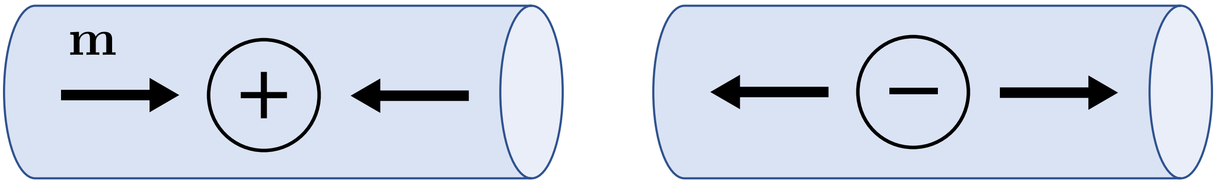

Figure 1.2: Schematic of the domain wall polarity for (left) a head-to-head wall and (right) a tail-to-tail wall with their respective volume magnetostatic charge.

1.2.2 Current-driven dynamics

From the early works of Slonczewski [45], it has been predicted that an electric current can induce a torque on magnetization through an exchange s-d interaction. As a result, this spin transfer effect can cause the motion of domain walls. This effect has been introduced in the LLG equation through the addition of two terms [46, 47]:

$$\frac{\partial \mathbf{m}}{\partial t} = -\gamma_0 \mathbf{m} \times \mathbf{H}_{\text{eff}} + \alpha \mathbf{m} \times \frac{\partial \mathbf{m}}{\partial t} - (\mathbf{u} \cdot \boldsymbol{\nabla})\mathbf{m} + \beta \mathbf{m} \times (\mathbf{u} \cdot \boldsymbol{\nabla})\mathbf{m}, \tag{1.22}$$

where

$$\mathbf{u} = -\frac{g\mu_{\text{B}} P}{2eM_{\text{s}}}\mathbf{j} \tag{1.23}$$

is the velocity field, with g the gyromagnetic factor, μ_{B} the Bohr magneton, P the polarization ratio of the spins of flowing conduction electrons, e the elementary charge and $\mathbf{j}$ the electric current density. The first additional term describes the adiabatic process of the non-equilibrium conduction electrons. It is often called "adiabatic" term. The second additional term is related to the spatial mistracking of spins between conduction electrons and local magnetization. It is often called "non-adiabatic" term.

1.3 Domain walls in magnetically soft nanowires with a circular cross section

In this thesis, we consider only magnetically soft materials. This implies that the magnetic structures are largely determined by magnetostatics. Hence, for conduit such that cylindrical nanowires, the magnetization field tends to be aligned along the wire axis in order to minimize the demagnetizing energy. It results that domain walls carry a magnetostatic charge which is defined by the domains. If the magnetization field in both domains points towards (resp. outwards from) the center of the wall, we call this domain wall a head-to-head (resp. tail-to-tail) domain wall. We call this property the wall polarity (Fig. 1.2). This magnetostatic charge is discussed in more details in the appendix A.1 using a 1D model.

So far we did not discuss on the inner structure of such domain walls. In what follows, we describe the two types of domain walls that were found to be stable or metastable depending on the wire diameter [15].

1.3.1 Transverse(-vortex) wall

For diameters inferior to about 7 ℓ_{ex} (where $\ell_{\text{ex}} = \sqrt{\frac{2A}{\mu_0 M_{\text{s}}^2}}$ is the exchange-dipolar length), the most stable type of wall is called a transverse wall. The transverse wall is characterized

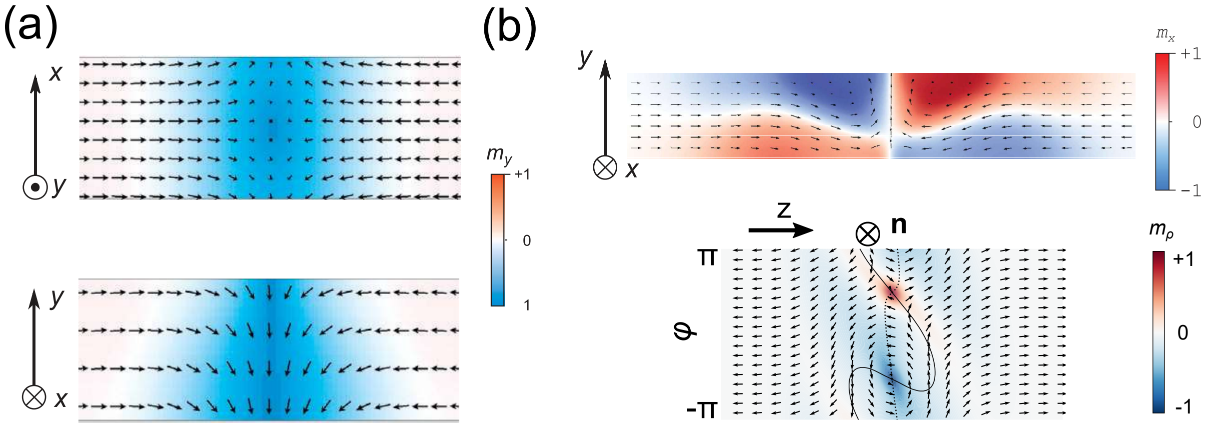

Figure 1.3: (a) Sections of a transverse wall. (b) Section of a transverse-vortex wall (top). Unrolled map of surface magnetization (bottom). The color codes the radial component m_ρ. The dashed lines correspond to $m_\varphi = 0$ and the solid lines correspond to $m_z = 0$. V and A highlight surface vortex and antivortex, respectively. The images (a) and (b) (top) are adapted from [15].

by a magnetization which is mostly transverse to the wire axis (Fig. 1.3(a)). However, when the diameter is larger (up to about 7 ℓ_{ex}), the magnetization acquires a curling feature at its center (Fig. 1.3 (b)(top)) which forms a vortex and an anti-vortex, diametrically opposed (Fig. 1.3 (b)(bottom)). These topological objects preserve the transverse aspect of the wall by having opposite polarities . This wall has been called transverse-vortex wall in [15] but also asymmetric transverse wall in the work [16].

From a topological aspect, we can continuously deform the transverse-vortex wall to obtain a transverse wall and conversely. However, we can not deform this wall and obtain a Bloch-point wall as it will be discussed more in details in section 4.2.

1.3.2 Bloch-point wall

When the diameter is above $7\ell_{\text{ex}}$, another wall has been found to be more stable than the transverse wall. As opposed to the transverse(-vortex) wall, it is characterized by a curling of the magnetization field around the wire axis, which led to the "vortex wall" denomination by some authors [48, 49]. This can be explained by the fact that this configuration creates a flux closure, which reduces the magnetostatic energy.

It has been demonstrated by Feldtkeller [17] that because of the curling, the magnetization field at the center of the wall should vanish. This is incompatible with the constraint on the norm of the magnetization field that must be constant everywhere. As a result, this point where magnetization is null is a singularity (the only one in three dimensions) which is called a Bloch-point. This is why it has been called a Bloch-point Wall (BPW) [11]. Strictly speaking, the micromagnetism is not suitable to describe such singularity. This matter has been discussed in the case of the reversal of a vortex core in a permalloy disc [50]. It has been shown that despite this, micromagnetics can still be used to gain insight into physics.

The presence of a Bloch-point induces a small radial component to the magnetization field which depends on the wall polarity. If we consider a head-to-head (resp. tail-to-tail) wall, the radial component will point outwards (resp. inwards) (see Fig. 1.4 (a) and Appendix A.1).

Due to the curling of magnetization, the BPW is characterized by a circulation (Fig. 1.4

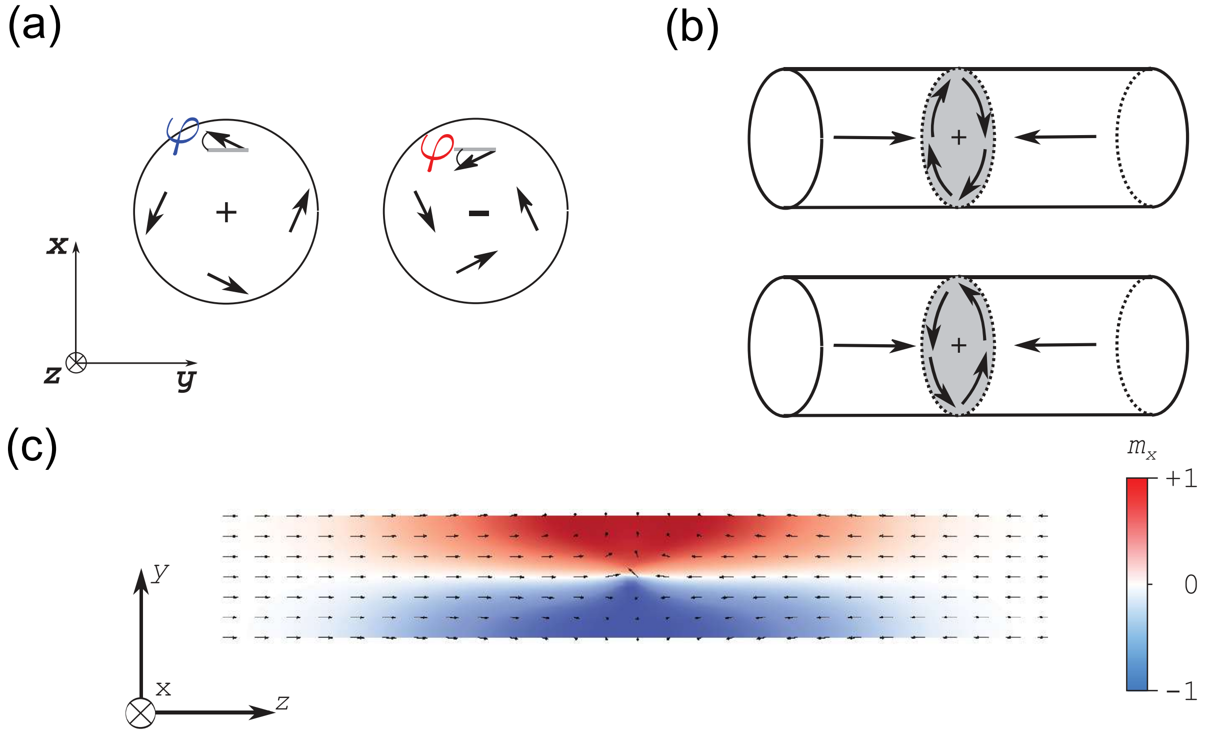

Figure 1.4: (a) Schematics of the radial tilt of a head-to-head (left) and a tail-to-tail domain wall (right). (b) Schematics of a Bloch-point wall with: a negative circulation (top) and a positive circulation (bottom) with respect to the wire axis z. (c) Longitudinal section of a nanowire of 80 nm diameter of with a BPW. Adapted from [15].

(b)). In this thesis, it will be defined as positive or negative with respect to either, the wire axis, or the current direction. Despite their differences, all these configurations (head-to-head or tail-to-tail with positive or negative circulation) are degenerated in energy for the static equilibrium state. We will show in the next section and the chapter 4 that when we consider a stimulus, such as a field or a current, it is no longer the case.

1.3.3 Domain walls motion

The domain wall motion has been extensively studied in nanostrips both theoretically and experimentally. In cylindrical nanowires wires, the motion of domain walls has been theorytically investigated by using analytical 1D models and micromagnetic simulations. In this section, we briefly show the main results on domain wall motion under field and applied current.

Motion under an applied magnetic field

The field-driven domain wall motion of transverse wall was first studied in nanowires with square section [11]. For the transverse wall, contrary to the case of nanostrips, the wall directly moves in a corck-screw regime with a linear propagation speed with respect to the applied field. Its behavior is really well described by the 1D model in which are defined the collective coordinates q, the wall position and ϕ the tilt angle that the transverse wall has with respect to a reference plan (e.g. (x-z) plan). This model gives an expression for the propagation speed

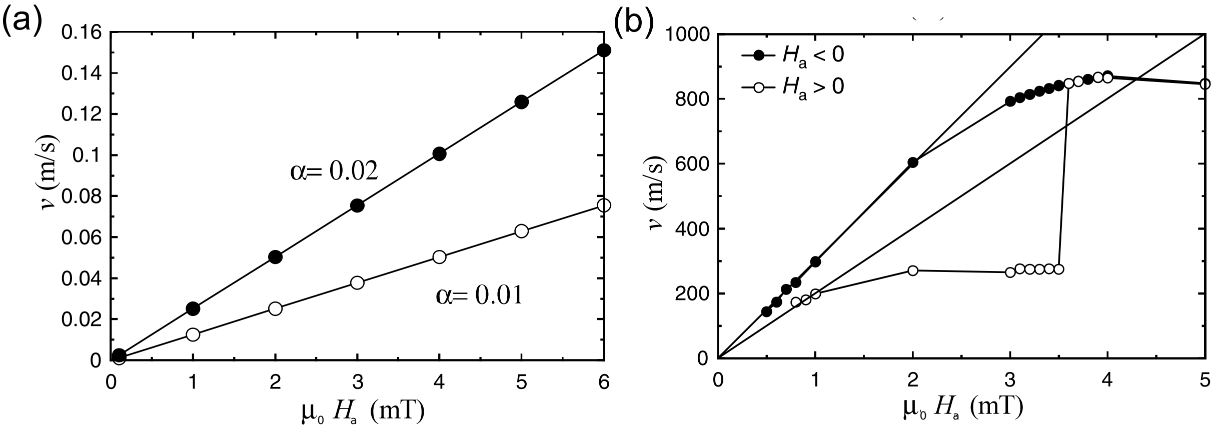

Figure 1.5: (a) Transverse-wall speed in a square nanowire (edge size 5 nm, mesh size 5 nm). (b) Simulation of a Bloch-point wall in a permalloy nanowire with square cross section of 40 nm. The wall average speed for two different circulation. Black dot for positive circulation and white dot for negative circulation. The field H_a is applied along the wire axis. Adapted from [11].

$$\dot{q} = \frac{\gamma_0}{1+\alpha^2}\alpha\Delta H_a, \tag{1.24}$$

where Δ is the wall width parameter, and the angular speed

$$\dot{\phi} = \frac{\gamma_0}{1+\alpha^2}H_a. \tag{1.25}$$

The BPW dynamics has been studied in square section nanowires [11] and later in circular section [26]. We have seen in the previous section, that a BPW is characterized by a radial tilt whose sign depends on the wall polarity. Under an applied field, this tilt will be modified depending on the orientation of the applied field. Hence, in the presence of a BPW with a certain circulation and an applied field along the nanowire , we expect a different behavior of the magnetization field, depending on the sign of the field. The resulting speed is presented Fig. 1.5 (b). It results that the motion of the Bloch-point under field is dependent on the initial circulation. At low field, the speed of the BPW with the favored circulation shows a linear behavior with respect to the applied field and is proportional to $1/\alpha$. However, as we increase the field, the speed of the BPW with the opposite circulation reaches a plateau. It is followed by an abrupt change toward the speed of the BPW with the favored circulation. Thus, there exist a threshold field for which the BPW with the unfavored circulation will change its circulation. At higher fields, the speed saturates, which correspond to a magnonic regime [26].

Motion under an applied spin-polarized current

Micromagnetic simulations have been performed using Eq. (1.22) for flat strips (see review [12]). In flat strips, different regimes exist. A stationary regime, where the domain propagates without distorsions and the speed is proportional to the current. Beyond a certain threshold, the wall enters a transient regime called the Walker breakdown where the domain wall structure no longer holds resulting in the propagation of vortex anti vortex leading to a drastic reduction of the wall speed. In cylindrical nanowires, it has been shown that such breakdown does not exist [35, 51].

For the transverse wall, it is analogous to say that it is already in a precessional regime as soon as the current is applied in the case $\beta \neq \alpha$ [51]. It is shown throught micromagnetic

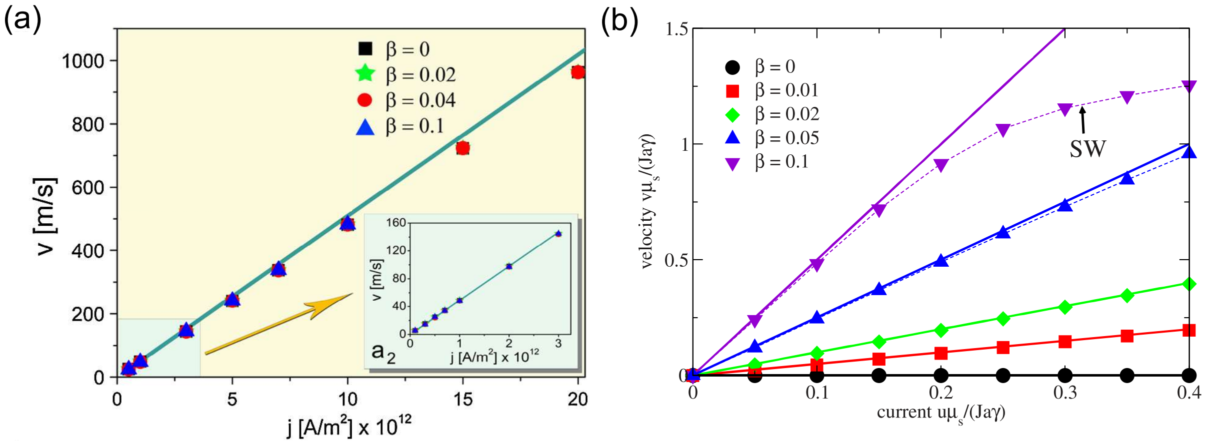

Figure 1.6: (a) Simulated TW velocity as a function of the current density j for four different values of β in the case of a 10 nm round Py wire (damping parameter $\alpha = 0.02$). The solid line comes from (1.26) (b) Simulation of a vortex wall (a BPW) in a cylindrical permalloy nanowire of $8d_2$ diameter where d_2 is the next nearest-neighbor distance. The damping parameter $\alpha = 0.02$. Adapted from [27, 35].

simulations that the propagation speed (Fig. 1.6 (a)) have a linear behavior with respect to the applied current density, which is well predicted by the 1D model through the expression

$$\dot{q} = -\frac{1+\alpha\beta}{1+\alpha^2}u, \tag{1.26}$$

The speed of precession is given by

$$\dot{\phi} = \frac{\beta-\alpha}{1+\alpha^2}\frac{u}{\Delta}. \tag{1.27}$$

We will briefly talk about this precession in the section 3.4.1 in a different context (pinned state).

For a Bloch-point wall, similar to the field-driven case, its dynamics is circulation dependent. It as been shown in [35], for the favored circulation, the wall's motion is steady (Fig. 1.6 (b)). It is analogous to say that the Walker current tends towards infinity. In this regime, the speed of the domain wall is given by

$$v = \frac{\beta}{\alpha}u. \tag{1.28}$$

For the other circulation, the BPW will react by adjusting first its configuration, resulting in a slightly backward motion [35]. After its transformation, the BPW has the favored circulation, which result in the steady propagation previously described. As it will be shown in the chapter 4 of this thesis, this phenomenon of circulation switching will also occur in wider nanowires ($> 7\ \ell_{\text{ex}}$) due to the presence of the Œrsted field.

Chapter 2

The Finite elements based software *feeLLGood*

Considering a micromagnetic system, one is generally interested into the problems of finding the equilibrium states (magnetic textures) and describing their dynamics under a magnetic field or/and an electric current for example. One way to find the equilibrium states is to solve an energy minimization problem i.e. involving an energy functional like the one previously introduced in section 1.1.2. An other way is to integrate the LLG equation. In our case, the latter is more suitable because we study the domain walls dynamics which is obtained by solving this LLG equation. Moreover, it allows us to take into account additional terms that can't be derived from an energy. However, for most of systems, these problems lack of analytical solutions. Hence, we need to reformulate (approximate) these problems in order to use numerical methods to solve them. These methods that rely on computers can only solve a discrete form of the problems. In our case, the LLG equation implies a discretization both in time and space.

The idea of time discretization (leading to a time scheme) is first to divide the simulation time into time steps k. This time step can either be fixed or adaptive. Second, the magnetization field is computed at a later time (usually one step further) from an initial configuration. We note $\mathbf{m}^n$ and $\mathbf{m}^{n+1}$ the magnetization field evaluated at instants $t = nk$ and $t = (n+1)k$ respectively. Computation of $\mathbf{m}^{n+1}$ can be done using a truncated Taylor expansion up to order p at time nk which gives $\mathbf{m}^{n+1} = \mathbf{m}^n + O(k^p)$. This scheme is said to be accurate up to the p-order with a local error $O(k^{p+1})$. Hence, to calculate $\mathbf{m}^{n+1}$ we needs to estimate its time derivatives which up to order one $(\partial_t \mathbf{m}^n)$ is obtained by solving the LLG problem. Usually, it is interesting to increase the order of a scheme, since it allows the use of a larger time step for the same accuracy, hence reducing the simulation time. The increase of order however can be challenging since it can destabilize the scheme. This problem will be tackled in the section 2.2 of the chapter.

Existing numerical methods involve different approach of space discretization. Two of the most used methods are the finite differences and the finite elements methods (FEM). The finite differences method is based on a direct approximation of the differential operators using Taylor series expansions. The domain is usually approximated by a regular mesh. The advantage of this method is that it is easily implemented, can be really fast and accurate. However, for a system with a curvilinear geometry, the lattice symmetries will introduce an artificial anisotropy inside the system.

The finite element method is used to solve problems involving partial differential equations in their weak form. It is based on a discretization of the domain into finite subdomains called finite elements which do not overlap. We make the distinction between volume elements and boundary elements. These elements are usually polyhedron (tetrahedrons in our case) that allows to approximate nicely any complex geometries. This why this method has been chosen since we are interested into curvilinear geometries such has wires or tubes. The solution is approximated by a function resulting from the interpolation of basis functions (in our case Lagrange polynomials P1) defined on each element. As a result, the integral over the domain can be decomposed into a sum of integrals over each element (elementary integrals). It is important to note that each element is affine-equivalent to a reference element. By transforming each element (and their respective basis functions) to this reference element, one can evaluate the previous elementary integrals using the Gauss-Legendre quadrature(or method) on the reference element integral. It results a linear system of equation (one per element) that is conveniently transformed into its matrix form. Then each elementary matrices are assembled in such way that it forms a sparse matrix. The result is a linear system of equation representing the whole system that will be solved using the iterative method of bi-conjugate gradient.

The power of FEM is what motivated the creation of the software called FeeLLGood (Finite element Landau-Lifshitz-Gilbert object oriented development). In this thesis all the results have been obtained with it, so we will describe how the problem has been implemented. Complementary informations can be found on the website [38].

2.1 Notion of weak formulation of the LLG equation

The weak form of the micromagnetic problem involving the LLG equation is obtained by projecting this equation on a basis of a test function space. The term weak comes form the fact that this form weakened the condition of differentiability of the solution. The unknown of the LLG equation is $\partial_t \mathbf{m}$. A solution of LLG should belong to a function space that respects the boundary conditions and the magnetization properties. For instance since $|\mathbf{m}| = 1$, $\partial_t \mathbf{m}$ must be orthogonal to $\mathbf{m}$. Hence, $\mathbf{v} = \partial_t \mathbf{m}$ must belong to the space

$$K_{\mathbf{m}} = \left\{ \mathbf{v} = \sum_i \mathbf{v}_i \phi_i : \forall i, \mathbf{v}_i \cdot \mathbf{m}_i = 0 \right\} \tag{2.1}$$

where ϕ_i are basis function P^1 linear in each element, m_i are the values of magnetization at each nodes. This space (tangent plane) has been proposed by Alouges [36].

In the same work, Alouges suggested to transform the LLG equation (1.17) to a form similar to a diffusion equation. He proposed to do the cross-product between $\mathbf{m}$ and the LLG equation. We obtain the following strong form:

$$\alpha \frac{\partial \mathbf{m}}{\partial t} + \mathbf{m} \times \frac{\partial \mathbf{m}}{\partial t} = \gamma_0 \left(\mathbf{H}_{\text{eff}} - (\mathbf{m} \cdot \mathbf{H}_{\text{eff}}) \mathbf{m} \right) \tag{2.2}$$

Then this equation is projected on test functions that belong to $K_{\mathbf{m}}$. Indeed, in the Galerkin method, both the test functions space and the solution space are the same. In order to keep the formalism simple $\gamma_0 = 1$. We get the following weak form

$$\alpha \int_\Omega \mathbf{v} \cdot \boldsymbol{\Psi} d\mathbf{x} + \int_\Omega (\mathbf{m} \times \mathbf{v}) \cdot \boldsymbol{\Psi} d\mathbf{x} = \int_\Omega \mathbf{H}_{\text{eff}}(\mathbf{m}) \cdot \boldsymbol{\Psi} d\mathbf{x} - \int_\Omega (\mathbf{m} \cdot \mathbf{H}_{\text{eff}}) \mathbf{m} \cdot \boldsymbol{\Psi} d\mathbf{x} \tag{2.3}$$

where the last term is null when both $\mathbf{m}$ and $\boldsymbol{\Psi}$ are evaluated at the same time.

The effective field can be decomposed in two terms:

$$\mathbf{H}_{\text{eff}} = \mathbf{H}_{\text{ex}} + \mathbf{H}_r \tag{2.4}$$

where $\mathbf{H}_{\text{ex}} = \frac{2A}{\mu_0 M_s}\Delta\mathbf{m}$ and $\mathbf{H}_r$ contain other contributions (demagnetizing field, external field etc...). For simplicity, the factor in front of the laplacian is considered to be equal to 1 and $\mathbf{H}_r$ is discarded. Replacing the effective field by the exchange field in (2.3) we get

$$\alpha \int_\Omega \mathbf{v} \cdot \mathbf{\Psi} d\mathbf{x} + \int_\Omega (\mathbf{m} \times \mathbf{v}) \cdot \mathbf{\Psi} d\mathbf{x} = \int_\Omega \Delta\mathbf{m} \cdot \mathbf{\Psi} d\mathbf{x} \tag{2.5}$$

Integrating by part the exchange term allows us to consider both the domain and its boundary

$$\int_\Omega \Delta\mathbf{m} \cdot \mathbf{\Psi} d\mathbf{x} = -\int_\Omega \nabla\mathbf{m} \cdot \nabla\mathbf{\Psi} d\mathbf{x} + \int_{\partial\Omega} (\nabla\mathbf{m} \cdot \mathbf{n}) \cdot \mathbf{\Psi} \tag{2.6}$$

where $\mathbf{n}$ is the normal to the surface. This allows us to include directly the boundary conditions, called Brown conditions:

$$\frac{\partial\mathbf{m}}{\partial\mathbf{n}} = 0 \tag{2.7}$$

leading to the weak form

$$\alpha \int_\Omega \mathbf{v} \cdot \mathbf{\Psi} d\mathbf{x} + \int_\Omega (\mathbf{m} \times \mathbf{v}) \cdot \mathbf{\Psi} d\mathbf{x} = -\int_\Omega \nabla\mathbf{m} \cdot \nabla\mathbf{\Psi} d\mathbf{x} \tag{2.8}$$

2.2 Temporal scheme

The problem needs to be discretized in time. Considering a simulation duration T, we divide it into time intervals k. In the following, we note $\mathbf{m}^n$, the magnetization configuration and $\mathbf{v}$ the magnetization evolution at the instant nk. Hence, the weak form (2.8) at instant nk writes:

$$\alpha \int_\Omega \mathbf{v} \cdot \mathbf{\Psi} d\mathbf{x} + \int_\Omega (\mathbf{m}^n \times \mathbf{v}) \cdot \mathbf{\Psi} d\mathbf{x} = -\int_\Omega \nabla\mathbf{m}^n \cdot \nabla\mathbf{\Psi} d\mathbf{x} \tag{2.9}$$

This is an explicit scheme where magnetization $\mathbf{m}^{n+1}$ at time (n+1)k is obtained by a Taylor expansion up to the first order :

$$\mathbf{m}^{n,1} = \mathbf{m}^n + k\mathbf{v} \tag{2.10}$$

Due to the constraint $\mathbf{m} \cdot \partial_t \mathbf{m} = 0$, whatever the scheme which is used, the resulting $\mathbf{m}^{n,1}$ must be normalized:

$$\mathbf{m}^{n+1} := \frac{\mathbf{m}^n + k\mathbf{v}}{|\mathbf{m}^n + k\mathbf{v}|} = \frac{\mathbf{m}^n + k\mathbf{v}}{\sqrt{1 + k^2 v^2}} \tag{2.11}$$

The stability of a scheme is determined by the evolution of the energy. Previously, it has been seen that the energy should always decrease. Hence, a stable scheme means that it preserve this dissipation process. This explicit scheme is stable under the condition that k/h^2 is bounded, where h is greatest mesh element size (see Fig. 2.1). There is a compromise to be found between the time step and the greatest mesh element size. As it has been said previously, h cannot be higher than ℓ_{ex} and a too small time step can lead to a high increase of the calculation time.

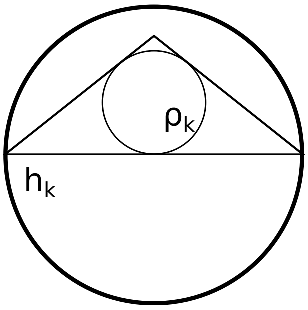

Figure 2.1: 2D triangle element k and the two characteristic lengths: h_k the element size and ρ_k the diameter of an inscribded circle centered at the intersection of the three internal angle bissectors.

2.2.1 Order 1

This is the reason why a θ-scheme has been implemented. This scheme is usually used with the heat diffusion problem. The idea is to replace $\mathbf{m}^n$ in the exchange term by an intermediate configuration $\mathbf{m}^{n,\theta} = \mathbf{m}^n + \theta k \mathbf{v}$ where $\theta \in [0,1]$ where $\mathbf{v}$ is evaluated at time $(n+\theta)k$. Adding this term is equivalent to add a sort of filter that will attenuate the noise propagation thus stabilize the scheme. Although the tangent plane and $\mathbf{v}$ are no longer evaluated at the same time, the last nonlinear term of the expression (2.3) is deliberately discarded. The resulting weak form writes

$$\alpha \int_\Omega \mathbf{v} \cdot \boldsymbol{\Psi} d\mathbf{x} + \int_\Omega (\mathbf{m}^n \times \mathbf{v}) \cdot \boldsymbol{\Psi} d\mathbf{x} + \theta k \int_\Omega \nabla \mathbf{v} \cdot \nabla \boldsymbol{\Psi} d\mathbf{x} = - \int_\Omega \nabla \mathbf{m}^n \cdot \nabla \boldsymbol{\Psi} d\mathbf{x} \tag{2.12}$$

Note that we could have considered the replacement of $\mathbf{m}^n$ in the last term of (2.3). However, it produces a non linear term v^2 which can't be properly treated. This problem will be approached in the section 2.2.2.

The stability of this scheme is determined by calculating the energy difference between two time steps. The trick is that (2.12) is valid for any $\boldsymbol{\Psi}$ so we can chose $\boldsymbol{\Psi} = \mathbf{v}$ since they belong to the same space. Thus, we get the dissipated power:

$$\alpha \int_\Omega \mathbf{v} \cdot \mathbf{v} d\mathbf{x} + \theta k \int_\Omega \nabla \mathbf{v} \cdot \nabla \mathbf{v} d\mathbf{x} = - \int_\Omega \nabla \mathbf{m}^n \cdot \nabla \mathbf{v} d\mathbf{x} \tag{2.13}$$

We define the exchange energy difference between instant (n+1)k and nk after normalization by :

$$\Delta E = \int_\Omega (\nabla \mathbf{m}^{n+1})^2 - (\nabla \mathbf{m}^n)^2 \tag{2.14}$$

It has been demonstrated by Bartels [52] that for element with angles inferior to $\pi/2$, the normalization reduces the exchange energy:

$$\int_\Omega (\nabla \mathbf{m}^{n+1})^2 \leq \int_\Omega (\nabla \mathbf{m}^{n,1})^2 \tag{2.15}$$

As a result the difference in exchange energy between instant (n+1)k and nk after normalization is smaller:

$$\Delta E \leq \int_\Omega (\nabla \mathbf{m}^{n,1})^2 - (\nabla \mathbf{m}^n)^2 \tag{2.16}$$

In order to see how the θ parameter affects the stability of the scheme, we need to expand the first term of the right hand side

$$\int_{\Omega} (\nabla \mathbf{m}^{n,1})^2 = \int_{\Omega} (\nabla \mathbf{m}^n)^2 + 2k \nabla \mathbf{m}^n \cdot \nabla \mathbf{v} + k^2 (\nabla \mathbf{v})^2 \tag{2.17}$$

Replacing the second member of the right hand side using (2.13) and using (2.16) we finally get

$$\Delta E \leq -2k\alpha \int_{\Omega} \mathbf{v} \cdot \mathbf{v} d\mathbf{x} - (2\theta - 1)k^2 \int_{\Omega} \nabla \mathbf{v} \cdot \nabla \mathbf{v} d\mathbf{x} \tag{2.18}$$

As a result, we see that the stability is determined by θ.

- For $\theta > 1/2$, the energy decreases and the scheme is unconditionally stable.
- For $\theta < 1/2$, we are in the case where the scheme is stable under a condition.
- For $\theta = 1/2$, the scheme seems to be the most stable and has been chosen.

We know that the renormalization procedure prevents us from perfectly reaching order 2 but its effect remains minor in the limit of small time steps compared to the nonlinear term of the expression (2.3) which has been removed in the formulation (2.12). Its reintroduction will be the subject of the next paragraph.

2.2.2 Toward order 2

Increasing to the order 2 would allow the use of even bigger time steps for the same accuracy. Therefore, the previous scheme has been modified in the work [37] and will be briefly introduced here. So far, we have just modified the magnetization for the exchange term by replacing $\mathbf{m}^n$ with $\mathbf{m}^{n,\theta}$. We need to consider directly $\mathbf{m}^{n,\theta}$ starting from (2.3):

$$\alpha \int_{\Omega} \mathbf{v} \cdot \mathbf{\Psi} d\mathbf{x} + \int_{\Omega} (\mathbf{m}^{n,\theta} \times \mathbf{v}) \cdot \mathbf{\Psi} d\mathbf{x} = \int_{\Omega} \mathbf{H}_{\text{eff}}(\mathbf{m}^{n,\theta}) \cdot \mathbf{\Psi} d\mathbf{x} - \int_{\Omega} (\mathbf{m}^{n,\theta} \cdot \mathbf{H}_{\text{eff}}) \mathbf{m}^{n,\theta} \cdot \mathbf{\Psi} d\mathbf{x}. \tag{2.19}$$

To simplify again, we consider only the exchange field. Discarding the terms in v^2, the last term gives one term similar to the damping α term:

$$\int_{\Omega} (\alpha - \theta k (\nabla \mathbf{m}^n)^2) \mathbf{v} \cdot \mathbf{\Psi} d\mathbf{x} + \int_{\Omega} (\mathbf{m}^n \times \mathbf{v}) \cdot \mathbf{\Psi} d\mathbf{x} + \theta k \int_{\Omega} \nabla \mathbf{v} \cdot \nabla \mathbf{\Psi} d\mathbf{x} = - \int_{\Omega} \nabla \mathbf{m}^n \cdot \nabla \mathbf{\Psi} d\mathbf{x}. \tag{2.20}$$

The damping term $(\alpha - \theta k (\nabla \mathbf{m}^n)^2)$ leads to two problematic situations. First, it can be negative which means the positive definiteness and unicity of the solution is threatened. Second, if this damping is too big, this might destabilise the scheme. Hence, this term needs to be bounded. By posing $X = (\nabla \mathbf{m}^n)^2$ and $C = 2\alpha r/k$ where r is set to 0.1, we get

$$\varphi(\mathbf{m}) = \begin{cases} \frac{\alpha}{1 + \frac{k}{2\alpha} min(-X, C)} & X < 0 \\ \alpha + min(X, C) & X \geq 0 \end{cases} \tag{2.21}$$

However, this is not sufficient to transform this scheme into an unconditionably stable one. Thus, the second highest order term is modified by adding a function $\rho(k)$:

$$\int_\Omega \varphi_M(\mathbf{m}^n)\mathbf{v}\cdot\mathbf{\Psi}d\mathbf{x}+\int_\Omega(\mathbf{m}^n\times\mathbf{v})\cdot\mathbf{\Psi}d\mathbf{x}+\theta k\int_\Omega(1+\rho(k))\nabla\mathbf{v}\cdot\nabla\mathbf{\Psi}d\mathbf{x}=-\int_\Omega\nabla\mathbf{m}^n\cdot\nabla\mathbf{\Psi}d\mathbf{x}. \tag{2.22}$$

Until now we considered only the contribution from the exchange for the sake of demonstration. This scheme has been extended to the total effective field leading to the true implementation:

$$\begin{aligned}\int_\Omega \varphi_M(\mathbf{m}^n)\mathbf{v}\cdot\mathbf{\Psi}+\mathbf{m}^n\times\mathbf{v}^n\cdot\mathbf{\Psi}d\mathbf{x}+\frac{k}{2}\int_\Omega(1+\rho(k))\frac{\partial\mathbf{H}_{\text{eff}}}{\partial\mathbf{m}}(\mathbf{v})\cdot\mathbf{\Psi}\\ =\int_\Omega\mathbf{H}_{\text{eff}}(\mathbf{m})\cdot\mathbf{\Psi}d\mathbf{x}.\end{aligned} \tag{2.23}$$

2.3 Coupling LLG with transport

In order to consider the effect of the current, we used the model introduced in section 1.2.2. The additional terms have been added using an explicit scheme. Hence, by doing the vector product of magnetization and the form (1.22) we obtain the following strong form:

$$\alpha\frac{\partial\mathbf{m}}{\partial t}+\mathbf{m}\times\frac{\partial\mathbf{m}}{\partial t}=\gamma_0\mathbf{H}_{\text{eff}}-(\mathbf{m}\cdot\mathbf{H}_{\text{eff}})\mathbf{m}-\mathbf{m}\times(\mathbf{u}\cdot\boldsymbol{\nabla})\mathbf{m}-\beta(\mathbf{u}\cdot\boldsymbol{\nabla})\mathbf{m}. \tag{2.24}$$

By considering the previously derived weak form, the one that has been implemented in the code is

$$\begin{aligned}\int_\Omega \varphi_M(\mathbf{m}^n)\mathbf{v}^n\cdot\mathbf{\Psi}+\mathbf{m}^n\times\mathbf{v}^n\cdot\mathbf{\Psi}d\mathbf{x}+\frac{k}{2}\int_\Omega(1+\rho(\mathbf{m}))\frac{\partial\mathbf{H}_{\text{eff}}}{\partial\mathbf{m}}(\mathbf{v})\cdot\mathbf{\Psi}\\ =\int_\Omega\mathbf{H}_{\text{eff}}(\mathbf{m})\cdot\mathbf{\Psi}d\mathbf{x}+\int_\Omega(\mathbf{m}^n\times(\mathbf{u}\cdot\nabla)\mathbf{m}^n)\cdot\mathbf{\Psi}+\beta(\mathbf{u}\cdot\nabla)\mathbf{m}^n\cdot\mathbf{\Psi}d\mathbf{x}\end{aligned} \tag{2.25}$$

I have contributed to the implementation of the Œrsted field introduced in section 1.1.1.

2.4 Demagnetizing field computation: The Fast Multipole Method

As previously introduced in section 1.1.1, the demagnetizing field is derived from a magnetostatic potential φ_m. Again, in order to solve this magnetostatic problem we need to discretize it. The first step consist in transforming the continuous charge densities ρ and σ into a discrete distribution of N point charges. This formulation corresponds then to a N-body problem. Such a pair-wise problem shows a complexity of $\mathcal{O}(N^2)$ which induces a significant simulation time. It is a real challenge when it comes to reduce the computation times. Different existing methods are able to reduce the complexity. The FEM is able to reduce it down to $\mathcal{O}(N^{4/3})$. The Fast-Fourier Transform in a NFFT algorithm [53] for rectangular system decreasing complexity down to $\mathcal{O}(NlogN)$. For our systems, the hierarchical multipole method and its improved version, the Fast Multipole Method (FMM), reduces the complexity down to $\mathcal{O}(NlogN)$ and $\mathcal{O}(N)$ respectively. This last method is the one that has been implemented in the code and hence will be introduced in this section.

2.4.1 The multipoles expansion

The magnetostatic potential φ generated by N sources at the target point $\mathbf{r}$ writes:

$$\varphi(\mathbf{r}) = \sum_{i}^{N} G(\mathbf{r}, \mathbf{r}')\, q_i \tag{2.26}$$

where q_i correspond to the charge at the i^{th} node and $\mathbf{r}'$ its position and G the previously introduced Green function (also called a kernel). The equation (2.26) in its matrix form clearly shows that its direct computation has a complexity of $\mathcal{O}(N^2)$ ($N \times N$ matrix). We will now introduce the hierarchical multipole method by presenting a 2D case being simpler and also intuitive than the 3D case. This allows us to use the complex plan which simplifies the notations. Hence, the magnetic potential at affixe z generated by one point charge at affixe z_i writes

$$\varphi_i(z) = \ln|z - z_i|\, q_i \tag{2.27}$$

This can be expanded the follow:

$$\varphi_i(z) = q_i \log z - q_i \sum_{k=1}^{\infty} \frac{1}{k} \left(\frac{z_i}{z}\right)^k \tag{2.28}$$

The total potential is obtained by a multipole expansion

$$\varphi(z) = R \log z + \sum_{k=1}^{\infty} \frac{a_k}{z^k} \tag{2.29}$$

where

$$R = \sum_{i=1}^{m} q_i, \quad \text{and} \quad a_k \sum_{i=1}^{m} \frac{-q_i z_i^k}{k} \tag{2.30}$$

The error verifies

$$\left| \sum_{k=p+1}^{\infty} \frac{a_k}{z^k} \right| \leq A \sum_{k=p+1}^{\infty} \frac{r^k}{k|z|^k} \tag{2.31}$$

with $A = \sum_i |q_i|$. This term itself is majored by

$$\frac{A}{p+1} \sum_{k=p+1}^{\infty} \left(\frac{r}{|z|}\right)^k = \frac{A}{(p+1)(1 - r/|z|)} \left(\frac{r}{|z|}\right)^{p+1} \tag{2.32}$$

We see that the error decreases with p faster the lower is $r/|z|$. In other words, it decreases with p faster the further the target point is from the sources. To sum up, all the contributions from m sources can be expressed by a multipole expansion at the center of a ball that contains all the sources. If the target point is faraway, we can take a larger ball, thus taking into account more sources with the same accuracy.

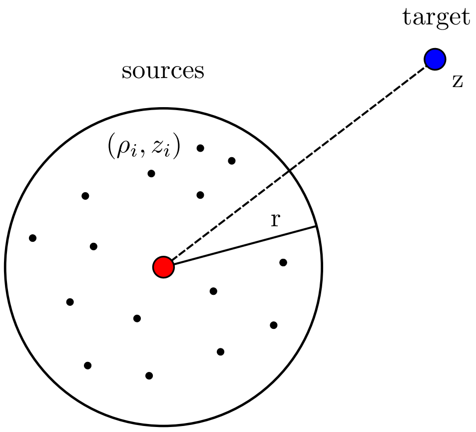

Figure 2.2: Schematic of a discrete distribution of charges.

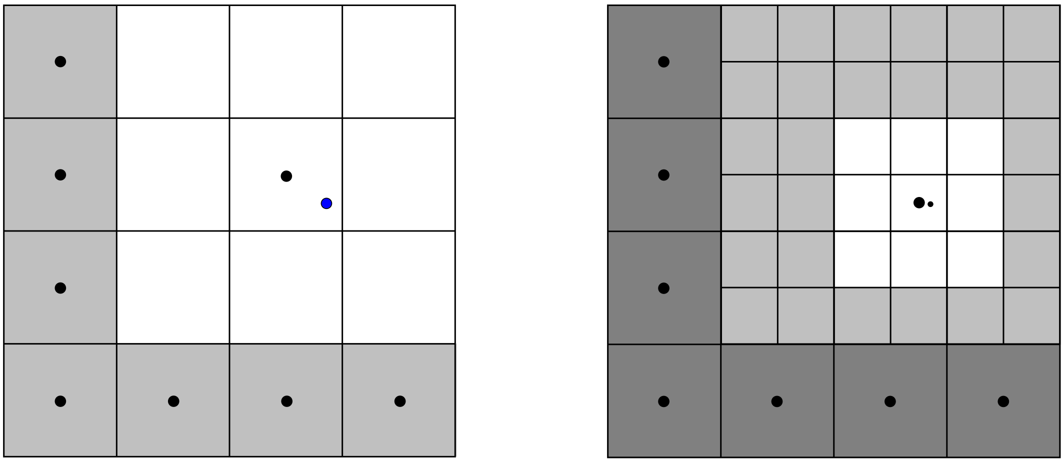

Figure 2.3: The level 2 (left) and a combination of the level 2 and 3 (right) of the tree. The light gray boxes correspond to the well separated boxes that needs to be calculated. The dark gray boxes correspond to the well separated boxes that are already calculated. The white boxes correspond to the near neighbors of the box that contain the target.

2.4.2 The hierarchical Multipoles Method

The idea is to generate a tree structure by subsequently dividing the computational domain. The 0^{th} level is the computational domain which as an example is a box. It is divided into four parts called children and the children follows the same process. The last refinement level called the leaf is obtained by limiting the number of particles (here nodes) that it contains.

Two boxes that are at the same level and share boundary points are called near neighbors. On the contrary, boxes of the same level that are not near neighbors are said to be well separated.

The idea is to consider clusters of particles that interacts. For each level, the calculation is performed only for well separated boxes. For level 0 and 1, this situation does not occur. It starts with the level 2 shown in Fig. 2.3 (left) with the well separated boxes are the light gray ones.

Hence if we wants to calculate the contributions for the neighboring boxes we need to reach the next level Fig. 2.3 (right). The source charges are gathered to form clusters. These clusters are divided into two groups the source and the target.

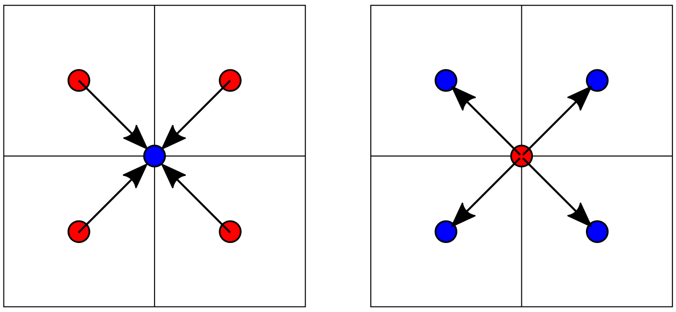

Figure 2.4: Expansion translation from children to parent (left), from parent to children (right).

2.4.3 The Fast Multipoles Method

It is possible to decrease further the complexity down to $O(N)$. The idea is to keep the computation by translating the expansions (Fig. 2.3). Thus, an expansion calculated at the center of a box can be translated to the center of its parent. Hence the expansions are computed by translation of children's expansion without having to calculate again from the sources. The translation from point z_0 to origin is based on

$$\frac{1}{(z-z_0)^k} = \sum_{l=k}^{\infty} C_{l-1}^{k-1} \frac{z_0^{l-k}}{z^l} \tag{2.33}$$

If the initial expansion is valid outside a ball of radius r, the translated one is valid outside a ball of radius $|z_0|+r$, which include the first one. The error done by truncation up to order p is

$$\left(\frac{|z_0|+r}{|z|}\right)^{p+1} \tag{2.34}$$

for a target in z. Each term of the translated expansion is obtained in p operations over the terms of the initial expansion. The total cost of the translation is then p^2. All the boxes of the system that gives their expansion to their parent, and supposing there are s sources per leaf boxes for a total of about M/s boxes, the expansions of all the boxes are calculated in time $Mp^2/s = O(N)$. The previous method was in $O(NlogN)$. However, there were an other problem in $O(NlogN)$, the evaluation. For each target, 27 expansion for each levels needed to be evaluated. The idea is the follow: we would like to evaluate the expansions of only one level, the last one, plus one expansion that come from the parent which accumulates information from inferior levels. We are interested is the sequence of boxes that contain the target and the well separated boxes. The contributions from the well separated boxes can not be summed directly. We can convert them in Taylor expansion in the self-contained sequence where they are summed in one expansion until the current level and transmitted to the children for the next level. The conversion of a multipolar expansion in a "local" Taylor expansion is based on

$$\frac{1}{(z-z_0)^k} = \frac{1}{(-z_0)^k}\left(\frac{1}{1-\frac{z}{z_0}}\right)^k \tag{2.35}$$

$$\frac{1}{(z-z_0)^k} = \frac{1}{(-z_0)^k} \sum_{l=k}^{\infty} C_{l-1}^{k-1} \frac{z_0^{l-k}}{z^l} \tag{2.36}$$

This two expansions are respectively valid in two separated balls of same radius r. One can show that the error done by truncation of the local expansion to p order is in $(r/d)^{p+1}$,d being the distance of the local ball to the center of multipole expansion z_0. Each term of the local expansion is obtained in p operations over the terms of multipole expansion, cost of conversion is p^2. All the boxes, convert their expansions to their 27 well separated neighbors, their local expansion of all the boxes are calculated in $27Mp^2/s$. After what starting from the first level, the $M/4s$ boxes transmit their expansions to their children in Mp^2s. Only the expansion of the last level are evaluated at the targets in Np and the calculations in near field are always $O(N)$. The Fast Multipole Method is then an accelerated version of the previous method thanks to translation and conversion operators. The 3D case is similar but is based on octrees (one box is divided into 8 boxes) and the expansion are spherical harmonics with p^2 terms instead of p. The translations are done in p^4 and can be reduced p^3 by combining them with rotation of coordinate systems [54].

2.5 Limits of numerical micromagnetism

A key hypothesis of the micromagnetic theory [40] is the description of magnetization with a continuous vector field of uniform and constant modulus. It is therefore not suitable mathematically to describe a Bloch point, involving a singularity in the vector field. In numerical micromagnetism, this mismatch induces artefacts like the pinning on the discrete numerical lattice during magnetization dynamics, or the logarithmic convergence of magnetization processes such as nucleation [50]. For example, in the finite element approach, the constraint on the magnetization norm is imposed at the mesh nodes. Within every volume element magnetization is interpolated linearly, with its norm possibly greatly reduced, allowing a magnetic object resembling a Bloch point to be centered inside. This magnetic object may move from one volume element to a neighboring one, however over an energy barrier, inducing a numerical frictional force that depends on the mesh size [34].

An atomistic model obviously provides an improvement, the mesh being scaled down to the ultimate size of atoms. However, due to the logarithmic convergence mentioned above, an intrinsic pinning field remains on the lattice, of the order of a few mT [55]. This effect may be responsible for the excitation of helical instabilities sometimes evidenced during motion of the BPW under a large driving force [56]. The question may arise, to which extent this reflects experimental physics. Indeed, in the atomistic models implemented so far, the magnetic moments keep a fixed magnitude on every lattice site. This is not realistic for band magnetism such as for Fe, Co, Ni and their alloys, for which one expects a local reduction of band splitting and thus atomic moment, allowing to reduce the total energy of the system [57].

The Landau-Lifshitz-Bloch (LLB) formalism aims to describe such situations, allowing for a spatial variation of magnetization by introducing a longitudinal susceptibility [58]. The Bloch point has been described by a LLB model, down to a cell size of 0.5 nm [59], however the impact on pinning has not been evaluated. Also, from a fundamental point of view, it is not clear to which extent the fitting of LLB parameters to macroscopic quantities such as the Curie temperature, adequately reflects sub-nm physics with strong gradients of magnetization in the case of band magnetism.

Thus, at this stage we consider that it remains an open question, to which extent Bloch points may be described suitably by simulation, especially regarding their motion.

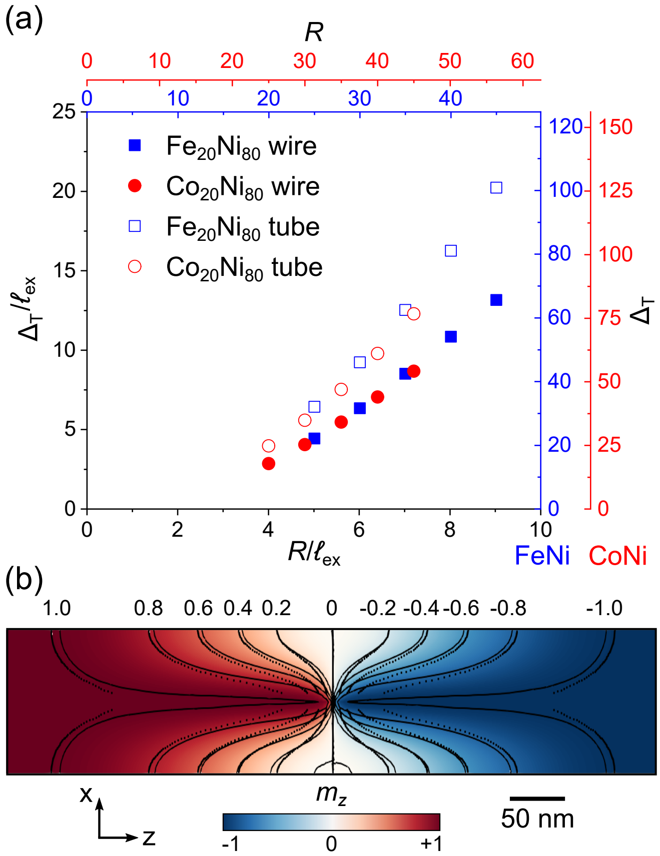

Figure 2.5: (a) Domain wall width (Thiele definition) versus the external radius, expressed in real length (top and right axis) and normalized with the dipolar exchange length ℓ_{ex} (bottom and left axis) (b) Section in the xz plane of the wire. The colors represent the z component of the normalized magnetization. The contour lines represent isovalues of m_z. The solid lines correspond to the wire, the dotted lines to the tube. Adapted from [62].

The thick-walled tube ansatz

In the course of the present report we sometimes consider and compare two situations: that of a wire, and that of a thick-wall tube (*i.e.*, a wire with an empty core of very small radius, 5 nm). Strictly speaking there is no more Bloch point in a thick-walled tube for a BPW at rest, so that in the manuscript we refer to the wall as pseudo-Bloch-point wall (PBPW). This type of wall in a nanotube is often called a vortex wall, in the literature.

Qualitatively, the physics of domain walls in wires and tubes indeed displays many similarities, such as the possible absence of Walker breakdown and the magnonic regime [11, 60]. Quantitatively, features of tubes tend to converge to wires, when the thickness of the tubes is increased [61]. Below we compare the two situations at equilibrium, to provide a basis for our ansatz.

We characterized both walls through their width, following Thiele definition:

$$\Delta_{\mathrm{T}} = \frac{2S}{\int_{\mathcal{V}}(\frac{\partial \mathbf{m}}{\partial z})^2 \mathrm{d}\mathcal{V}}\,, \tag{2.37}$$

where S is the section of the nanowire or nanotube. Fig.2.5a shows that Δ_{T} increases with radius R for both situations. This graph is plotted with lengths scaled to ℓ_{ex}, to provide a material-independent curve. First, note that while different materials fall on the same curve for wires, a slight shift exists for tubes. This arises as through normalizing with ℓ_{ex}, the inner radius kept constant to 5 nm converts in a slightly different geometry. However, the main point in this plot is the sizable difference of width between a BPW and a PBPW, although the difference in section S is only a few percent. To understand this, we examine the micromagnetic distribution of both walls in the xz plane (Fig.2.5b). The two walls share a similar configuration near the outer surface, while they differ significantly close to the axis. Indeed, the absence of Bloch point in the tube removes the need for the pinching of magnetization, explaining a larger width there. It is because the Thiele definition puts a larger weight on locations with a large magnetization gradient, that the resulting width is significantly different although the volume with significant differences is rather small. The similarity of the two maps of magnetization on the outer part of the structure, where the Œrsted field driving the dynamics is largest, makes us confident that a thick-walled tube is a reasonable ansatz for a wire.

Chapter 3

Current-driven dynamics of a transverse wall in a modulated cylindrical nanowire

This chapter focuses on the current-driven transverse domain wall dynamics in a circular cross-section nanowire presenting a single modulation in diameter. On my arrival to SPINTEC my colleagues have been working on the domain wall dynamics induced by the applied magnetic field in these modulated geometries. Quite naturally, my first experience with massive micromagnetic calculations followed in the footsteps of my predecessor J. Fernandez-Roldan [63]. In the frame of my thesis I went beyond the field-induced case and studied micromagnetically the current-induced behavior of the domain wall, as well as developed simplified analytical description of this situation. The text of this chapter is largely adapted from a chapter to which I contributed, namely *Domain wall pinning in a circular cross-section wire with modulated diameter* of the book *Magnetic Nano- and Microwires* (Elsevier 2020) [39]. The text published previously has been completed here by more details in most of the sections (except the section 3.1) such as a more detailed 1D model under current 3.4.1 and new results with the abrupt modulation of the current-driven case 3.4.2.

3.1 Motivation

3.1.1 Fundamental and technological motivations for domain wall pinning

The interest for domain walls in one-dimensional conduits is both for the sake of physics and for technological concepts. As regards physics, considering domain walls in nearly one-dimensional systems allows one to reduce the number of internal degrees of freedom to a minimum. In the limit of cylindrical wires with a diameter typically below seven times the dipolar exchange length $l_{\mathrm{ex}} = \sqrt{2A_{\mathrm{ex}}/\mu_0 M_{\mathrm{s}}^2}$, with A_{ex} the exchange stiffness and M_{s} spontaneous magnetization, one can neglect variations of magnetization across the wire section, boiling down the description of the domain wall to a one-dimensional problem [11]. In any case, compared with extended thin films this reduces the possible complexity of the wall, obviously easing the understanding of any phenomenon related with domain-wall motion, *e.g.* precessional dynamics and spin-torques. As regards technology, domain walls have been proposed as means to store [64–66], transport and process information

[2, 67].

It may be desirable to modulate the energy landscape of a domain-wall in such a one-dimensional conduit. This may include potential barriers or potential wells. On the applied side, such modulations can allow to repeatedly initialize the system with a domain wall at a precise location. This is especially useful to implement time-resolved measurements in a pump-probe scheme, which requires the averaging of reproducible events, including the preparation of a given type of domain wall [68]. Also, energy barriers may be used to confine a domain wall in a segment of finite length to ease its investigation [69]. On the applied side, a digital memory device requires that bits of information are allocated a specific physical location. Thus, domain walls may be forced to remain in potential wells, or conversely, be separated by energy barriers. Among others, this prevents that successive walls in a conduit merge together, which would induce the loss of information. Also, similar to the argument given above for fundamental devices, defining a precise starting position can be helpful to clock circuits, for instance in the case of logic functions involving several domain walls.

The modulation of potential along the conduit has been largely developed and exploited in planar strips based on thin film and lithography technologies. Most are based on the modulation of geometry, which is easily achievable with lithography. This includes notches [68, 70], protrusions [71] or more complex designs such as connection to other magnetic pads [72]. Other means have been demonstrated, such as stray field from neighboring magnetic pads [73] or domain walls [74], ion irradiation [75, 76] or reprogrammable electric-field gating [77].

3.1.2 Types of pinning for nanowires

In the present chapter we focus on cylindrical conduits, which we will call nanowires. Magnetic nanowires have been synthesized routinely for several decades, mostly by *e.g.* electroplating in polymer or anodized aluminum templates [78–80]. This synthesis methods presents constraints to design modulations of the potential for domain walls, however also offers opportunities, with respect to flat strips. There exist essentially two designs, which have been developed experimentally and considered theoretically in the past ten years.

The first route for creating a potential landscape, is through the geometry of the wire, involving the longitudinal modulation of the diameter (Fig. 3.1). Indeed, the energy of a domain wall sensitively depends on the wire (local) diameter, involving changes in both exchange and dipolar energy. The most commons means to achieve such a modulation are multistep anodization [80, 81] or pulsed anodization [82] of aluminum. While the versatility is lower than with lithography for strips, a large variety of designs has been demonstrated. More exotic routes exist, such as pulsed plating followed by etching [31], or the alternation of wire and tubes [83, 84]. The focus of the present work is restricted to the diameter modulation of a plain wire.

The second route for creating a potential landscape, is through the longitudinal modulation of the material. While this is analogous to strips processed with local irradiation or gating, it is more straightforward and versatile to achieve in nanowires, by changing the growth conditions during synthesis. The ways to achieve this are multibath anodization for more versatility, or pulsing the plating potential in a bath with several metal salts, for a faster implementation [85, 86]. Note that one may use various magnetic materials, especially varying the composition of compounds [32], or non-magnetic materials such as

Cu [86, 87].

3.1.3 Existing theories and experiments

The one-dimensional landscape model for domain walls is probably one of the earliest problems tackled in magnetism to explain the physics of coercivity, as described by the Becker-Kondorski model [88–91]. A key conclusion is that while domain walls are found at the bottom of energy wells at rest, the depinning field is associated with local maxima of slope of the potential, themselves coinciding with inflection points of the potential curve. We will see that this concept is still applicable for the more specific theories developed in our contribution. Later on, the one-dimensional landscape model was used again in specific cases by A. Aharoni and followers, again in the context of the physic of coercivity. Potential wells and steps [92], slopes [93] and others, were introduced and described. These effective models have been made more specific to the geometry of a nanowire, highlighting the local slope

A number of micromagnetic simulations have been made, considering linear modulations [29], sharp single modulations [30], sharp constrictions [31], smooth modulations of various length [32]. However, often the processes of domain-wall nucleation at a wire's end and the process of going through the modulation are not studied separately, thus not well describing the latter. Besides, some detailed models of walls at modulations have been proposed [33], however their complexity does not allow to shed a general picture on the phenomenon of pinning. Overall, the existing literature shows interesting features, however does not provide a comprehensive view. This lack has been driven the present work, to deriving simple analytical scaling laws, and compare the field-driven and current-driven cases.

Finally, note that experimental reports of the interaction of domain walls at modulations of diameter are still scarce and incomplete. Letting aside reports of magnetometry of large assemblies of wires still in a matrix, or experiments on single wires, however not separating the physics of nucleation from the one of going through the modulation, only a handful of reports exist of domain-walls in diameter-modulated single wires [21]. These do not provide a comprehensive quantitative picture at present

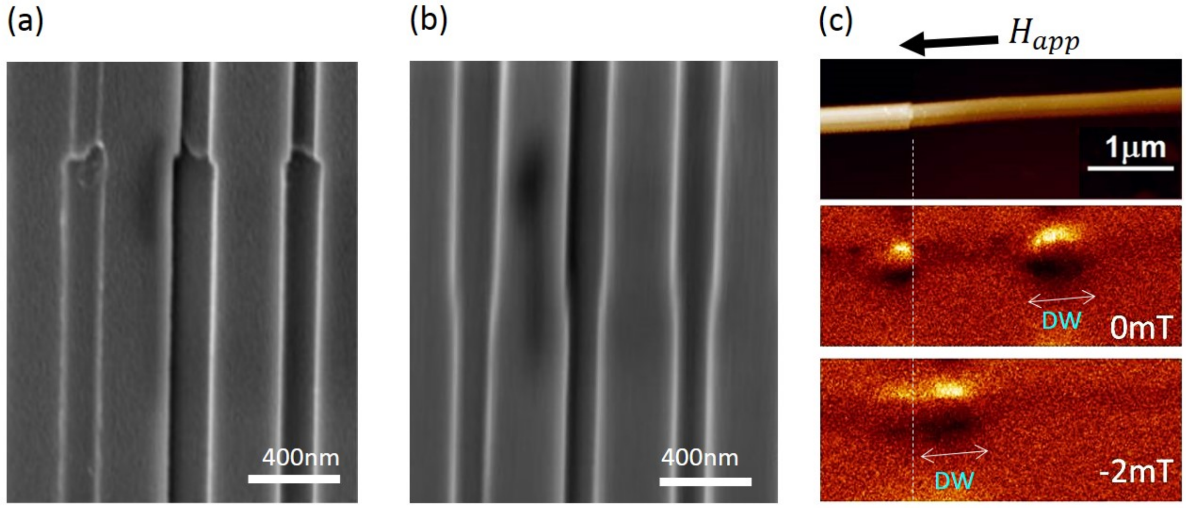

Figure 3.1: (a) and (b) Scanning electron micrographs illustrating the existence of two different diameter transition geometries in the multisegmented aluminum oxide membranes from [69] and [94]. (c) Topography of isolated multisegmented nanowire and magnetic force microscopy image showing the domain wall displacement after application of *dc* field [94]. Adapted from [39].

3.2 Theoretical background

In the following section, we introduce the framework we use to derive the analytical models of the dynamics of a transverse wall passing through a single modulation of diameter. For the simulations we considered a wire of $\mathrm{Fe_{20}Ni_{80}}$ (permalloy) with the exchange stiffness $A_{\mathrm{ex}} = 1 \times 10^{-11}\,\mathrm{J \cdot m^{-1}}$ and the spontaneous magnetization $M_{\mathrm{s}} = 8 \times 10^{5}\,\mathrm{A \cdot m^{-1}}$. The dipolar exchange length $l_{\mathrm{ex}} = \sqrt{2A_{\mathrm{ex}}/\mu_0 M_{\mathrm{s}}^2}$ is about 5 nm. The tetrahedrons that compose the meshes have a characteristic length of 2 nm, which is inferior to the exchange length. We considered a spin polarization rate $P = 0.7$.

3.2.1 Geometry of modulation and potential barrier

In presence of a domain wall inside a cylindrical nanowire, the internal energy of the system increases with the radius (Fig. 3.2). Hence, a modulation of diameter induces a variation of the internal energy of the system which depends on the position of the domain wall z_{w}. In the following, we study two types of modulation, which connect a smaller cross section with radius R_1, to a larger cross section with radius R_2: the abrupt modulation and the circular-based (smooth) modulation shown in Fig. 3.3(a).

The abrupt modulation is modeled by the simple step-function

$$R(z) = \begin{cases} R_1, & z < 0, \\ R_2, & z \geq 0. \end{cases} \tag{3.1}$$

The circle-based profile allows for a smooth transition between smaller and larger cross section parts

$$R(z) = \begin{cases} R_1, & z < -\lambda/2, \\ y_1 - \sqrt{R_{\mathrm{mod}}^2 - (z+\lambda/2)^2}, & -\lambda/2 < z < 0, \\ y_2 + \sqrt{R_{\mathrm{mod}}^2 - (z-\lambda/2)^2}, & 0 < z < \lambda/2, \\ R_2, & z > \lambda/2, \end{cases} \tag{3.2}$$

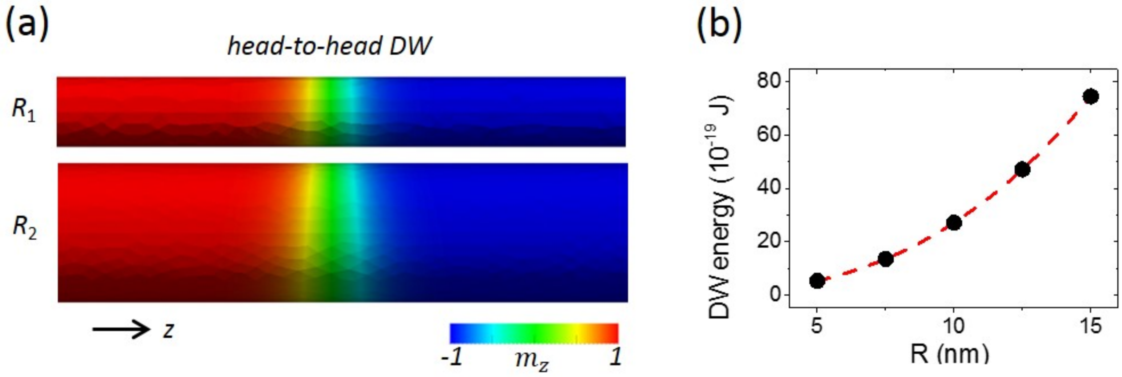

Figure 3.2: (a) Micromagnetic distribution of longitudinal magnetization for the transverse-like head-to-head domain wall for radius $R_1 = 5\,\text{nm}$ and $R_2 = 10\,\text{nm}$, obtained numerically using equation (1.17). (b) Simulated domain wall energy vs. diameter, in a straight wire. The dashed curve corresponds is a third-order polynomial fit serving as a guide to the eye. Adapted from [39].

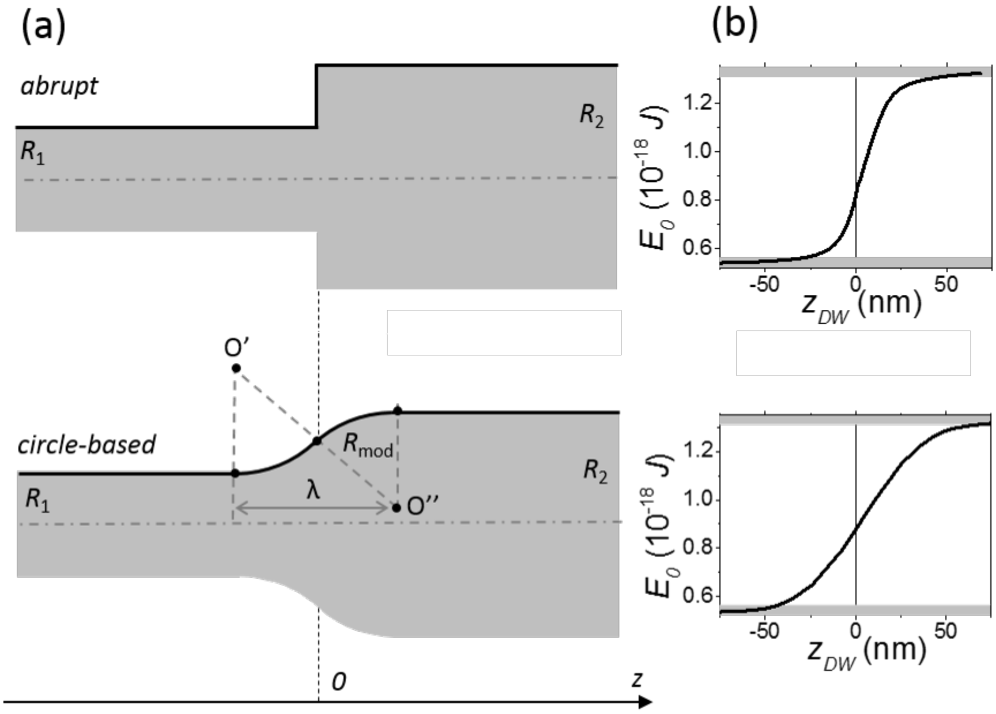

Figure 3.3: (a) Type of modulation geometry considered and (b) corresponding internal energy vs. its position z_w, from micromagnetic simulations. Parameters used for the energy plots are $R_1 = 5\,\text{nm}$, $R_2 = 7.5\,\text{nm}$, $\lambda = 100\,\text{nm}$ and $\mu_0 M_\text{s} = 1\,\text{T}$. Grey horizontal lines correspond to the energy of a straight wire with $R = 5\,\text{nm}$ and $R = 7.5\,\text{nm}$. Adapted from [39].

where λ is the modulation length,

$$\begin{aligned} R_{\text{mod}} &= [(R_2 - R_1)^2 + \lambda^2]/[4(R_2 - R_1)] \\ y_1 &= (R_2^2 + 2R_1R_2 - 3R_1^2 + \lambda^2)/[4(R_2 - R_1)] \\ y_2 &= (3R_2^2 - 2R_1R_2 - R_1^2 - \lambda^2)/[4(R_2 - R_1)]. \end{aligned}$$

It has been used in subsections 3.3.2 and 3.4.3 for the micromagnetic simulations. For the analytic calculations, the circle-based wire profile was approximated by the tanh-based profile

$$R(z) = [R_1 + R_2 + (R_2 - R_1)\tanh(4z/\lambda)]/2. \tag{3.3}$$

This is an analytic function which approximates well the circle-based profile in the case of the gently sloping modulations ($(R_2 - R_1) << \lambda$) studied in 3.3.2 and 3.4.3.

To illustrate the energy modification induced by the modulation, we show Fig. 3.3(b) the internal energy E_0 as a function of the position of the domain wall. These curves were obtained by solving the LLG equation (1.17) numerically for domain walls drifting from the broader part toward the thinner part of the wire in the absence of any external driving force. In that case we used $\alpha = 1$, to approach a quasistatic situation. Far from the modulation, the value of E_0 corresponds to the one of a straight wire, as depicted by horizontal grey lines. One can see that in both abrupt and smooth cases, the energy shows a smooth transition. While it can be expected for the smooth modulation case, one could expect a step-like behavior for the abrupt modulation. We explain this smooth transition from the fact that the domain wall is characterized by a certain width. In the abrupt case, the width of the transition seems to correspond approximately to the width of the domain wall. In the smooth modulation case the width of the transition between the lower and upper values of E_0 seems to correspond approximately to the modulation length λ.

3.2.2 Magnetic charges

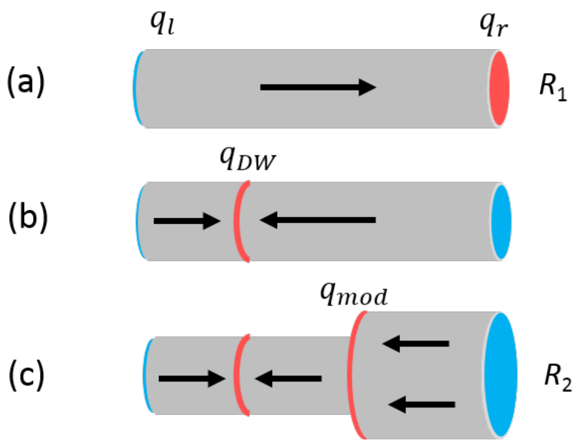

Figure 3.4: Schematics of magnetic charges distribution in (a) uniformly magnetized cylindrical wire, (b) cylindrical wire with head-to-head domain wall and (c) modulated diameter nanowire with head-to-head domain wall placed in the thinner part. Red color corresponds to the positive magnetic charge and blue one to the negative magnetic charge. Adapted from [39].

By analogy with electrostatics based on Maxwell's equations, the magnetic volume and surface charges $\rho_{\text{m}} = -M_{\text{s}}\nabla\cdot\mathbf{m}$ and $\sigma_{\text{m}} = M_{\text{s}}\,(\mathbf{m}\cdot\mathbf{n})$, may be introduced as a source

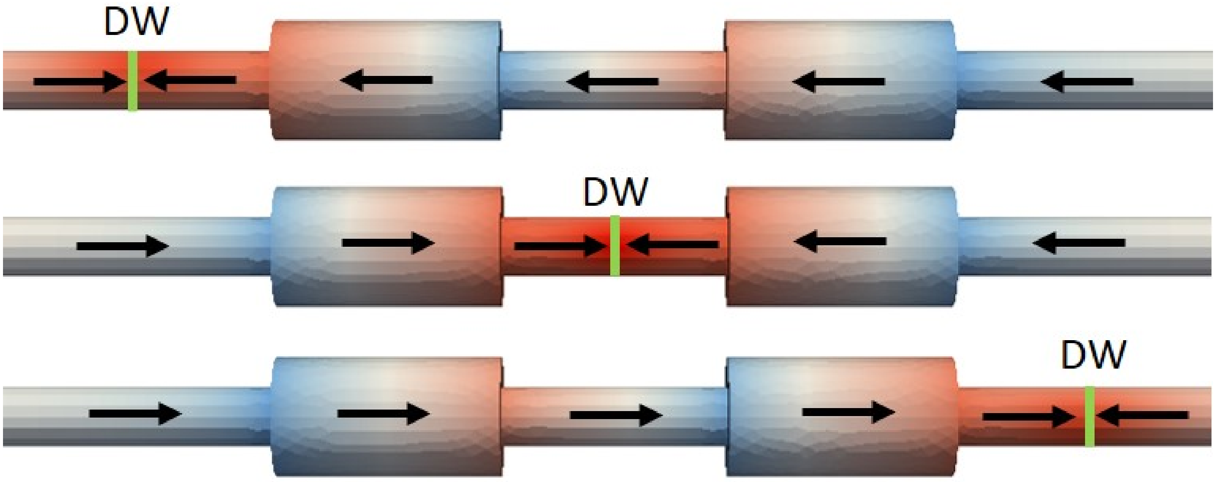

Figure 3.5: Magnetic potential ϕ_m distribution for different positions of the head-to-head domain wall. Red (resp. blue) color corresponds to positive (resp. negative) values of ϕ_m. Adapted from [39].

of the dipolar field H_d [41, 95], where $\mathbf{n}$ is the outward-pointing unit vector normal to the system surface. The expression for the dipolar field reads:

$$\mathbf{H}_\mathrm{d}(\mathbf{r}) = \int \frac{\rho_\mathrm{m}(\mathbf{r}')(\mathbf{r}-\mathbf{r}')}{4\pi|\mathbf{r}-\mathbf{r}'|^3} d^3\mathbf{r}' + \oint \frac{\sigma_\mathrm{m}(\mathbf{r}')(\mathbf{r}-\mathbf{r}')}{4\pi|\mathbf{r}-\mathbf{r}'|^3} dS'. \tag{3.4}$$

where $\mathbf{r}'$ is the position vector of a source and $\mathbf{r}$ is the position vector of the target point. In the case of the uniformly magnetized cylindrical wire (Fig. 3.4 (a)), each of the wire's end possesses the magnetic charge $q_1 = \pm\pi M_\mathrm{s} R_1^2$ leading to a total charge of zero. In the case of a head-to-head domain wall in a cylindrical nanowire (Fig. 3.4 (b)), the wire's ends carry the same charge $q_1 = -\pi M_\mathrm{s} R_1^2$. Hence the wall bears a magnetic charge which is largely determined by these boundaries and tend to neutralizes them. In fact, in the general case, the lateral surface can add a certain contribution. By neglecting the contribution from the lateral surface, the volume charge carried is approximately $q_\mathrm{DW} = 2\pi M_\mathrm{s} R_1^2$. It is exact in the special case of 1D transverse wall where the total surface charge carried by the wall is 0 (see Appendix A.1). Note that it does not mean that the dipolar field generated by these surface charges is zero. In the case of a modulation of diameter, the two end charges are different: $q_1 = -\pi M_\mathrm{s} R_1^2$ and $q_2 = -\pi M_\mathrm{s} R_2^2$. Considering for instance the case where the domain wall is clearly in the smaller-diameter part, the volume charge $q_\mathrm{DW} = 2\pi M_\mathrm{s} R_1^2$. Given this configuration, the modulation carries a charge $q_\mathrm{mod} = \pi M_\mathrm{s}(R_2^2 - R_1^2)$ (Fig. 3.4 (c)). At this stage, we did not discuss which type of charge (volume or surface) contributes to this charge. An example of distribution of the magnetic potential ϕ_m related to the charge distribution ($\mathbf{H}_\mathrm{d} = -\nabla\phi_\mathrm{m}$) is given in Fig. 3.5. Most notably, the modulation charge q_mod gives rise to a magnetic field H_mod, which we calculate in the next section. We show that it tends to move the domain wall away from the modulation.

3.2.3 Magnetic field generated by the modulation

The goal is to calculate the magnetic field generated by the modulation. While the total charge of the modulation is fixed, its distribution over surface and volume contributions is not straightforward. Thus, some approximation that conserves the total charge of the modulation should be done. We assume that the magnetization field in the modulation is uniform in the section and is aligned along wire axis ($\mathbf{m}(\mathbf{r}') = \pm\hat{\mathbf{e}}_z$). This simplification limits the magnetic charge of the modulation to the surface charge σ_m only, while volume charges are zero i.e $\rho_\mathrm{m} = 0$. The surface charge approximation allows us to estimate the amplitude of the magnetic field generated by the modulation analytically in some specific cases. This field can be seen as a subset of the closed surface integral of the dipolar field (3.4). With these assumptions, we write the field generated by the modulation as:

$$\mathbf{H}_\mathrm{mod}(\mathbf{r}) = \int_{S_\mathrm{mod}} \frac{\sigma_\mathrm{m}(\mathbf{r}')(\mathbf{r}-\mathbf{r}')}{4\pi|\mathbf{r}-\mathbf{r}'|^3} dS' \tag{3.5}$$

If we consider the presence of a head-to-head domain wall, the sign of the surface charge density σ_m will depends on the position of the domain wall z_w such that $\mathbf{m}(\mathbf{r}') = \mathrm{sgn}(z_\mathrm{w} - z')\hat{\mathbf{e}}_z$ where $\mathrm{sgn}(z_\mathrm{w}-z') = |z_\mathrm{w}-z'|/(z_\mathrm{w}-z')$. This approximation is suitable if: the domain wall is far away from the modulation and the modulation is abrupt or really smooth (slowly varying). It is incorrect when the domain wall hits or is inside the modulation. We can find a simple analytic expression for the field evaluated on the wire axis (i.e where $\mathbf{r} = z\hat{\mathbf{e}}_z$). Hence for simplicity, we assume the average field over a section to be equal to the field amplitude at the center (overestimation). The distance vector between a surface charge element and the target point $(\mathbf{r}-\mathbf{r}') = -\rho'\cos\varphi'\hat{\mathbf{e}}_x - \rho'\sin\varphi'\hat{\mathbf{e}}_y + (z-z')\hat{\mathbf{e}}_z$. On the wire axis, the axial symmetry implies that integration over the angle φ' vanish i.e. $H_x = H_y = 0$. Hence, $\mathbf{H}_\mathrm{mod}(z) = H_z(z)\hat{\mathbf{e}}_z$. For convenience we rename H_z into H_mod. The field expression writes

$$H_\mathrm{mod}(z) = \frac{M_\mathrm{s}}{4\pi}\int_{S_\mathrm{mod}} \frac{\mathrm{sgn}(z_\mathrm{w}-z')n_z(\mathbf{r}')(z-z')}{(\rho'^2+(z-z')^2)^{3/2}} dS' \tag{3.6}$$

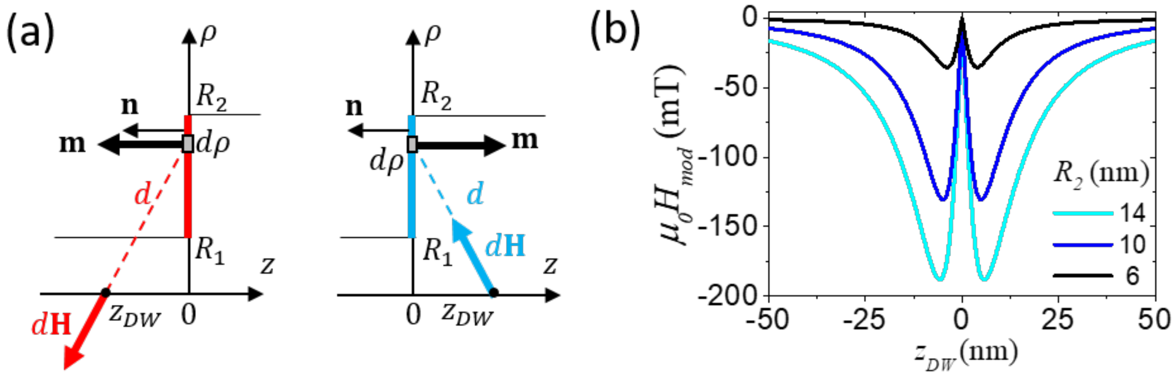

Figure 3.6: (a) Sketch of the magnetic field generated by the elements of the magnetically charged axisymmetric surface in the presence of the head-to-head domain wall at the position z_w for abrupt modulation. Red color corresponds to the positive surface charge and blue color to the negative one. d is the distance $|\mathbf{r}-\mathbf{r}'|$. (b) Magnetic field generated by the abrupt modulation $\mu_0 H_\mathrm{mod}$ vs. domain wall position z_w for several values of R_2. Parameters used for this plot are $R_1 = 5\,\mathrm{nm}$ and $\mu_0 M_\mathrm{s} = 1\,\mathrm{T}$. Adapted from [39].

Abrupt modulation. Besides being close to applicable in some experimental cases, the abrupt modulation is a text-book case, from which the general features of the impact of a modulation on domain-wall motion can be easily illustrated. The abrupt modulation is described by Eq. (3.1). Thus, the normal vector is aligned with the wire axis i.e. $n_z(\mathbf{r}') = -1$. The situation for a head-to-head wall is shown Fig. 3.6(a). Also the surface element $dS' = \rho' d\rho' d\varphi'$. If the modulation is centered at 0, $z' = 0$ and $\mathbf{m}(\mathbf{r}') = \operatorname{sgn}(z_\mathrm{w})\hat{\mathbf{e}}_z$, the expression of the field writes:

$$H_\mathrm{mod}(z) = -\frac{M_\mathrm{s}\operatorname{sgn}(z_\mathrm{w})z}{2}\int_{R_1}^{R_2}\frac{\rho'}{(\rho\prime^2 + z^2)^{3/2}}\,d\rho'. \tag{3.7}$$

giving

$$H_\mathrm{mod}(z) = -\frac{M_\mathrm{s}\operatorname{sgn}(z_\mathrm{w})z}{2}\left(\frac{1}{\sqrt{R_1^2+z^2}} - \frac{1}{\sqrt{R_2^2+z^2}}\right) \tag{3.8}$$

Evaluating the field at the domain center position (i.e. $z = z_\mathrm{w}$) we get

$$H_\mathrm{mod}(z_\mathrm{w}) = -\frac{M_\mathrm{s}|z_\mathrm{w}|}{2}\left(\frac{1}{\sqrt{R_1^2+z_\mathrm{w}^2}} - \frac{1}{\sqrt{R_2^2+z_\mathrm{w}^2}}\right) \tag{3.9}$$

which is plotted in Figure 3.6(b). The H_mod always opposes the head-to-head domain wall movement to the right, being negative for all z_w. In other words, the charges at the modulation tend to favor motion towards the part with smaller radius, similar to the energy of the domain wall itself.

Charged surface with arbitrary profile. While the main physics is captured by the abrupt modulation, it is associated with an unphysical cusp of H_mod at the very center of the modulation. Besides, it may not be realistic for slowly-varying modulations such as found in some experimental cases. The present paragraph intends to describe such situations. Following the same method and assuming only surface charges, let us calculate the magnetic field generated by the modulation with an arbitrary profile given by the smooth function $R(z')$. As shown in Figure 3.7(a) the corresponding modulation surface is charged positively to the right of the head-to-head domain wall and negatively to the left of it. We may assume a stepwise jump of surface charges across the domain-wall, in the case of gentle modulations. The differential element $dS' = |\partial_{\varphi'}\mathbf{r}' \times \partial_{z'}\mathbf{r}'|d\varphi' dz'$. The normal unit vector is defined:

$$\mathbf{n}(\mathbf{r}') \equiv \frac{\partial_{\varphi'}\mathbf{r}' \times \partial_{z'}\mathbf{r}'}{|\partial_{\varphi'}\mathbf{r}' \times \partial_{z'}\mathbf{r}'|} \tag{3.10}$$

and gives

$$\mathbf{n}(\mathbf{r}') = \left(1 + (\partial_{z'}R(z'))^2\right)^{-\frac{1}{2}}(\cos\varphi'\hat{\mathbf{e}}_x + \sin\varphi'\hat{\mathbf{e}}_y - \partial_{z'}R(z')\hat{\mathbf{e}}_z) \tag{3.11}$$

Replacing it into (3.6), the expression of field and evaluating it at $z = z_\mathrm{w}$:

$$H_\mathrm{mod}(z_\mathrm{w}) = -\frac{M_\mathrm{s}}{2}\int_{-\infty}^{\infty}\frac{|z_\mathrm{w} - z'|\partial_{z'}R(z')R(z')}{(R^2(z') + (z_\mathrm{w} - z')^2)^{3/2}}dz' \tag{3.12}$$

Figure 3.7(b) depicts H_mod for a tanh-based profile given by the formula (3.3). Similar to the case of abrupt modulation, H_mod opposes the head-to-head domain wall movement to the right. However, there is now no more cusp at $z_\mathrm{w} = 0$, and the maximum magnitude of H_mod is now found at the center of the modulation. Note that this maximum decreases sharply with increasing modulation length λ.

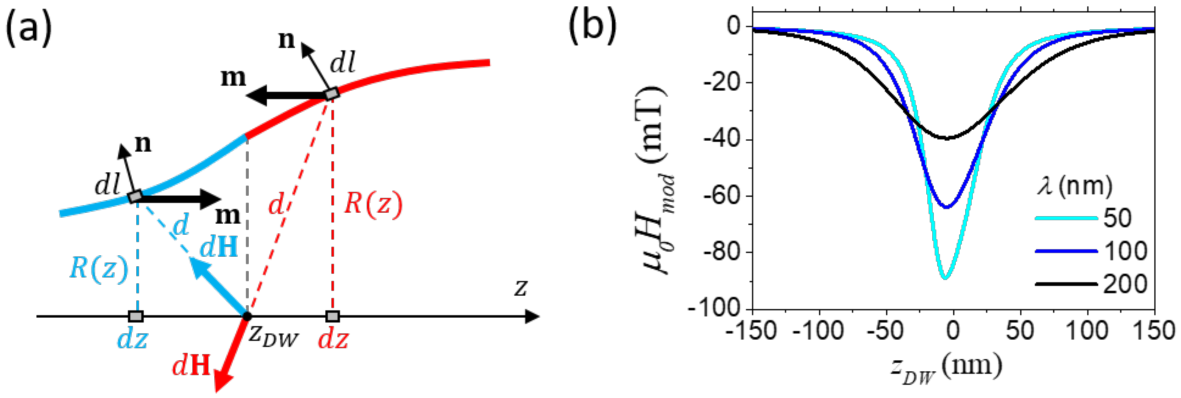

Figure 3.7: (a) Sketch of the magnetic field generated by the elements of the magnetically charged axisymmetric surface in the presence of the head-to-head domain wall at the position z_{w} for the modulation of arbitrary profile given by the continuous function $R(z)$. Red color corresponds to the positive surface charge and blue color to the negative one. d is the distance $|\mathbf{r}-\mathbf{r}'|$. (b) Magnetic field generated by the tanh-based profile modulation of the length λ vs. domain wall position z_{w} for several values of λ. Parameters used for this plot are $R_1 = 5\,\mathrm{nm}$, $R_2 = 10\,\mathrm{nm}$ and $\mu_0 M_{\mathrm{s}} = 1\,\mathrm{T}$. Adapted from [39].

3.2.4 Domain wall energy

The micromagnetic energy has been introduced in section 1.1.1. It is composed of the exchange energy, the demagnetizing energy and the Zeeman energy. This energy can be approximated by a reformulation of the problem. We define a domain wall internal energy E_{int} that depends on the wall position z_{w}. It can be viewed as a subset of the internal energy of the system. It is therefore composed of the exchange energy and of the dipolar energy that originate from the wall only (that will be detailed in subsection 3.3.2). In addition to that we define the energy of interaction between the wall and the field generated by the modulation charges. Hence this energy will be defined as a Zeeman energy. As a result this leads to the following total energy expression

$$E = E_{\mathrm{int}} + E_{\mathrm{z}} + E_{\mathrm{mod}} \tag{3.13}$$

The derivative of energy with respect to the wall position, can be written under the form of an effective field. The one associated with the supplementary energy term E_{mod} is reads, for an axisymmetrical wire:

$$\frac{\partial E_{\mathrm{mod}}}{\partial z_{\mathrm{w}}} = -\mu_0 q_{\mathrm{DW}} H_{\mathrm{mod}}(z_{\mathrm{w}}). \tag{3.14}$$

It is unlikely that E_{mod} has an analytic expression in the case of an arbitrary modulation profile and arbitrary domain wall profile. In contrast, the field distribution $H_{\mathrm{mod}}(z_{\mathrm{w}})$ can be derived analytically by making some assumptions, as shown in subsection 3.2.3. Besides, the z-derivative of energy may be sufficient, for example, to calculate the domain wall depinning field. In this case we do not need the energy E_{mod} expression but only its derivative, as the minimization of the total energy gives the domain wall pinned position.

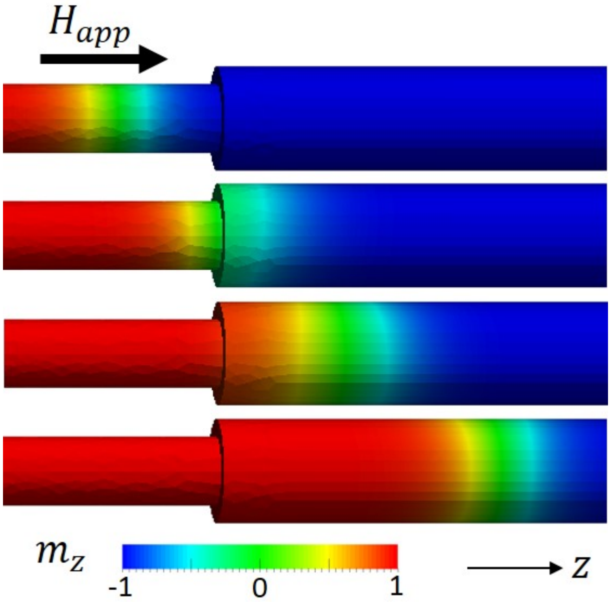

Figure 3.8: Head-to-head domain wall displacement under the applied magnetic field H_{app}. The color scale bar indicates the longitudinal magnetization m_z. Adapted from [39].

3.3 Modulation under applied magnetic field

In this section we focus on the case of domain wall behavior under a magnetic field applied along the wire's axis (Fig. 3.8). In particular we aim to calculate the critical field needed to depin the domain wall. As both the internal and the Zeeman energies are conservative, one may derive the critical field H_{crit} and corresponding critical domain wall position z_{crit} on the basis of the position-dependent domain wall energy. In the majority of cases the purely analytical treatment of this problem is tricky or even impossible. For this reason, below we propose an analytical estimation of the H_{crit} in particular limit cases, which implies a number of simplifying hypothesis. Despite the limitations of the simplified approach, our analytical analysis focuses on the key ingredients and gives a very reasonable estimation of the behavior of the critical depinning field in response to the modulation parameters. The cases for which the assumptions used below are too drastic should be covered by micromagnetic simulations.

3.3.1 Abrupt modulation

In this subsection we estimate the critical applied field H_{crit} needed to depin the domain wall in a wire with an abrupt modulation of diameter, described by equation (3.1) and visualized in Fig. 3.8. The wire axis was taken as the z direction. The modulation was centered at $z = 0$ and L is the total length of the wire. The head-to-head domain wall was prepared in the narrow section of the wire, and driven toward the larger section by applying a magnetic field.

Micromagnetic simulations suggest that for such a modulation, the transition between the two energy levels (or the potential barrier) is relatively sharp (Fig. 3.3(b)). Moreover, magnetization is mostly perpendicular to the modulation surface, which gives the surface charge $\sigma_{\mathrm{m}} = M_{\mathrm{s}}(\mathbf{m} \cdot \mathbf{n})$ and thus generates the large magnetic field of the modulation (Eq. (3.9)) and Fig. 3.6(b)). In this case it is reasonable to assume that

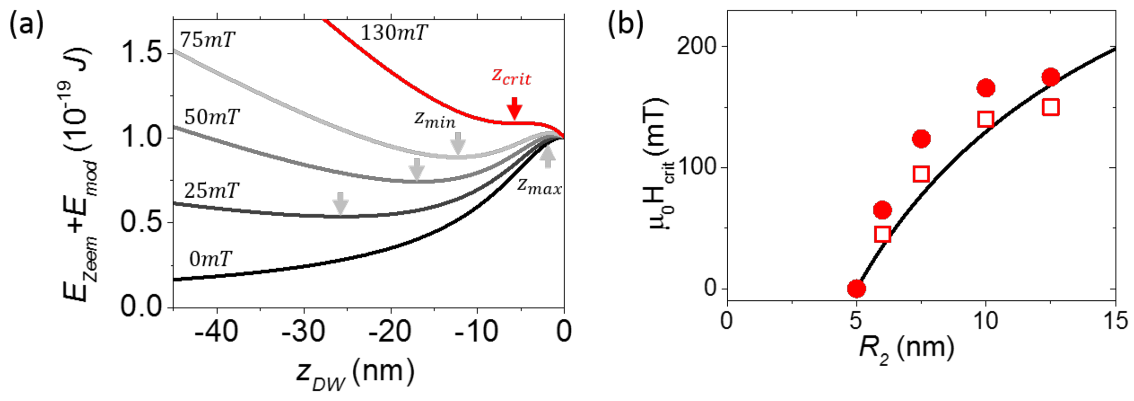

Figure 3.9: (a) Total energy $E_\mathrm{Z} + E_\mathrm{mod}$ versus domain wall position z_w for several values of the applied field and $R_2 = 10\,\mathrm{nm}$. Vertical arrows show the pinned domain wall positions. (b) Critical field value H_crit as a function of the larger radius R_2. Solid line corresponds to the analytic formula (3.17), solid circles and open squares correspond to micromagnetic simulations with $A_\mathrm{ex} = 1 \times 10^{11}\,\mathrm{J \cdot m^{-1}}$ and reduced $A_\mathrm{ex} = 0.25 \times 10^{11}\,\mathrm{J \cdot m^{-1}}$. All curves are plotted for $\mu_0 M_\mathrm{s} = 1\,\mathrm{T}$ and $R_1 = 5\,\mathrm{nm}$. Adapted from [39].

the key ingredient in domain wall pinning is the competition between the applied magnetic field H_app and the magnetic field generated by the modulation H_mod when the wall is not in contact with the modulation. Besides, the abrupt jump of diameter and thus domain wall energy when crossing the modulation, makes that this model can probably not describe realistically the total depinning process. Rather, it is illustrative to describe the rather long-range competition between the applied field contribution $E_\mathrm{Z} = -2\mu_0 M_\mathrm{s} H_\mathrm{app} \pi R_1^2 z_\mathrm{w} + \mathrm{Cste}$ and the energy of interaction between the domain wall and the modulation $E_\mathrm{mod} = -2\mu_0 M_\mathrm{s} \pi R_1^2 \int H_\mathrm{mod}(z) dz + \mathrm{Cste}$. This explains the non-monotonic energy profile with domain wall position z_w, as shown in Fig. 3.9(a). Note also, that we neglected the inner structure of the domain wall to derive these energies, instead we considered two adjacent uniformly magnetized domains on either sides of the domain wall's center position, z_w.

The energy shows two stationary points (i.e. $\partial(E_\mathrm{Z} + E_\mathrm{mod})/\partial z_\mathrm{w} = 0$) a maximum at z_max and a minimum at z_min. The latter corresponds to the domain wall pinned position. Using equations (3.9), (3.14) and applied field contribution, we obtain the expression which relates the applied magnetic field to the energy minimum:

$$H_\mathrm{app} = \frac{M_\mathrm{s}|z_\mathrm{min}|}{2}\left(\frac{1}{\sqrt{R_1^2 + z_\mathrm{min}^2}} - \frac{1}{\sqrt{R_2^2 + z_\mathrm{min}^2}}\right). \tag{3.15}$$

Since $H_\mathrm{app} = -H_\mathrm{mod}$ when a equilibrium is reached, this suggests the existence of a z_min in the large section. This will be discussed later in 3.4.2. However here, in the field driven case, the domain wall always stops before the modulation center. When reaching a critical value of applied field H_crit the inflection point between both extrema z_min and z_max becomes stationary. Hence, the critical position z_crit for which $\partial^2(E_\mathrm{Z} + E_\mathrm{mod})/\partial z_\mathrm{w}^2 = 0$ corresponds to the final pinned position of the domain wall:

$$z_\mathrm{crit} = -\frac{R_1^{2/3} R_2^{2/3}}{\sqrt{R_1^{2/3} + R_2^{2/3}}}, \tag{3.16}$$

and the corresponding H_{crit} needed to depin the domain wall reads

$$H_{\mathrm{crit}} = \frac{M_{\mathrm{s}}|z_{\mathrm{crit}}|}{2}\left(\frac{1}{\sqrt{R_1^2 + z_{\mathrm{crit}}^2}} - \frac{1}{\sqrt{R_2^2 + z_{\mathrm{crit}}^2}}\right). \tag{3.17}$$

Figure 3.9(b) compares formula (3.17) with micromagnetic simulation. This comparison reveals qualitatively and quantitatively similar tendencies. Note that simulations conducted with a value of A_{ex} reduced in comparison to that of the Permalloy-like material, fits slightly better the analytic results. Is may be explained by the more compact domain wall which probably better suits the model assumptions.

3.3.2 Smooth modulation

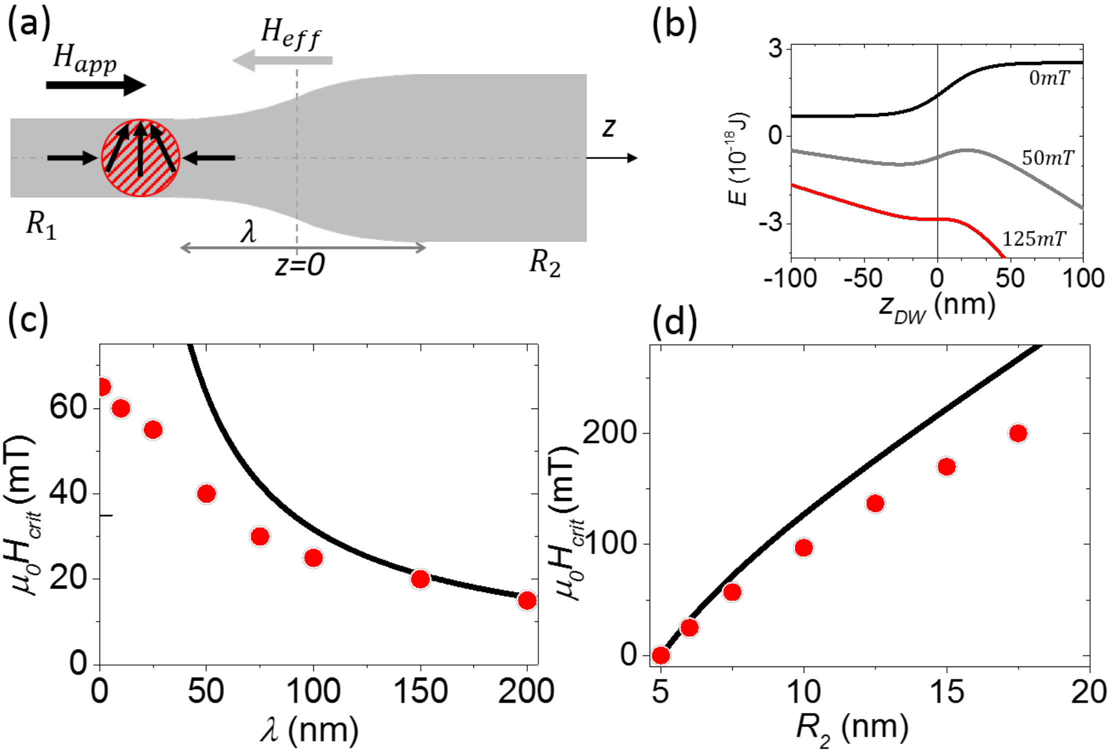

Figure 3.10: (a)Schematic illustration of the uniformly-charged sphere corresponding to the domain wall. (b) Domain wall energy $E_0 + E_{\mathrm{Z}}$ as a function of the domain wall position, for several values of applied magnetic field. (c) Critical field H_{crit} as a function of modulation length λ for $R_2 = 6\,\mathrm{nm}$. (d) Critical field H_{crit} as a function of larger radius R_2 for $\lambda = 100\,\mathrm{nm}$. All curves are plotted for $\mu_0 M_{\mathrm{s}} = 1\,\mathrm{T}$ and $R_1 = 5\,\mathrm{nm}$. Adapted from [39].

In this subsection we estimate the critical applied field H_{crit} needed to depin the domain wall in a smooth diameter modulation described by equation (3.3) and schematized in figure 3.10(a). We show that we can also describe $E(z_{\mathrm{mod}})$ at an arbitrary position including inside the modulation. In practice, the modulation with length λ was centered at $z = 0$, and L is the total length of the wire. The head-to-head domain wall was prepared in the narrow section of the wire and was driven towards the larger section by applying a magnetic field. To determine the qualitative expression for H_{crit}, we considered the domain wall internal and Zeeman energies E_{int} and E_{z} (from section 3.2.4). For simplicity, here we omit the energy of interaction E_{mod} between the domain wall and the field generated by the charges of the modulation. It has been shown in [63] for smooth modulations, that the extension of the present model by including the E_{mod} does not have a qualitative impact, and results only in a slight shift in the total energy minima and maxima. Below, we introduce the approximations that can be used to estimate each energy term. The details of calculation may be found in [63].

For the dipolar energy, we considered that the magnetic charge $q_{\mathrm{DW}} = 2M_{\mathrm{s}}\pi R^2$ [96] carried by the head-to-head wall was uniformly distributed within a plain sphere of radius R, thus with a magnetic charge density $\rho_{\mathrm{m}} = 3q_{\mathrm{DW}}/4\pi R^3$. The real distribution of the magnetic charge is much more complex [16], [56]. Nevertheless, our approximation leads to a compact analytical expression for the different energy terms and gives a reasonable order of magnitude. Note that this magnetic charge depends on the domain wall position z_{w}, through $R(z_{\mathrm{w}})$.

By analogy with electrostatics, a dipolar field H_{d} is generated by the charged plain sphere, with a total magnetostatic contribution $3\pi\mu_0 M_{\mathrm{s}}^2 R^3/5$. This contribution rapidly grows with the wire radius like R^3 which is consistent with the micromagnetic simulations of the domain wall energy plotted in Fig. 3.2(b) as a function of R. The exchange energy contribution can be estimated by applying the one-dimensional spin chain model [95] with slowly varying magnetization. In this case $[\nabla \mathbf{m}(r)]^2 \approx (\pi/2R)^2$, so that the total exchange energy contribution equals $A_{\mathrm{ex}}\pi^3 R/3$. To estimate the Zeeman energy contribution, we neglected the inner structure of the domain wall and considered the Zeeman energy of two adjacent uniformly magnetized domains located at the domain wall's center position, z_{w}. The wall energy excluding the integration constant then becomes:

$$E(z_{\mathrm{w}}) = \frac{3\pi}{5}\mu_0 M_{\mathrm{s}}^2 R^3(z_{\mathrm{w}}) + \frac{A_{\mathrm{ex}}}{3}\pi^3 R(z_{\mathrm{w}}) - 2\mu_0 M_{\mathrm{s}} H_{\mathrm{app}}\pi \int_{-L/2}^{z_{\mathrm{w}}} R^2(z)dz \tag{3.18}$$

and is depicted in figure 3.10(b). Note that is it compulsory analytically to consider the finite length of the wire, so that the Zeeman energy is finite.

Both local minima and local maxima are found using energy minimization $\partial E(z_{\mathrm{w}})/\partial z_{\mathrm{w}}=0$, which gives:

$$\frac{\partial R(z_{\mathrm{w}})}{\partial z_{\mathrm{w}}}\left(\frac{18}{5} + \frac{l_{\mathrm{ex}}^2\pi^2}{3R^2(z_{\mathrm{w}})}\right) - \frac{4H_{\mathrm{app}}}{M_{\mathrm{s}}} = 0 \tag{3.19}$$

with $l_{\mathrm{ex}} = \sqrt{2A_{\mathrm{ex}}/\mu_0 M_{\mathrm{s}}^2}$. For a tanh-based profile and smooth modulation with $(R_2 - R_1)/(R_2 + R_1) << 1$, the coordinates of minimum and maximum of energy reads

$$z_{\mathrm{max,min}} = \pm\frac{\lambda}{4}\mathrm{arctanh}\sqrt{1 - aH_{\mathrm{app}}}, \tag{3.20}$$

where $a = \frac{5\lambda}{9M_{\mathrm{s}}(R_2 - R_1)}\left[1 + \frac{10 l_{\mathrm{ex}}^2\pi^2}{27(R_1+R_2)^2}\right]^{-1}$. The coordinate of the energy minimum z_{min} corresponds to the domain wall pinned position. It corresponds to an internal effective field H_{eff} experienced at this point by the center of the domain wall:

$$H_{\mathrm{eff}} = -H_{\mathrm{app}} = -\frac{1}{a}\left(1 - \tanh^2(\frac{4z_{\mathrm{min}}}{\lambda})\right). \tag{3.21}$$

The domain wall depinning condition, at a given critical applied field value H_{crit}, can be defined as the convergence of two energy extrema at the same point, $z_{\mathrm{min}} = z_{\mathrm{max}}$ (red

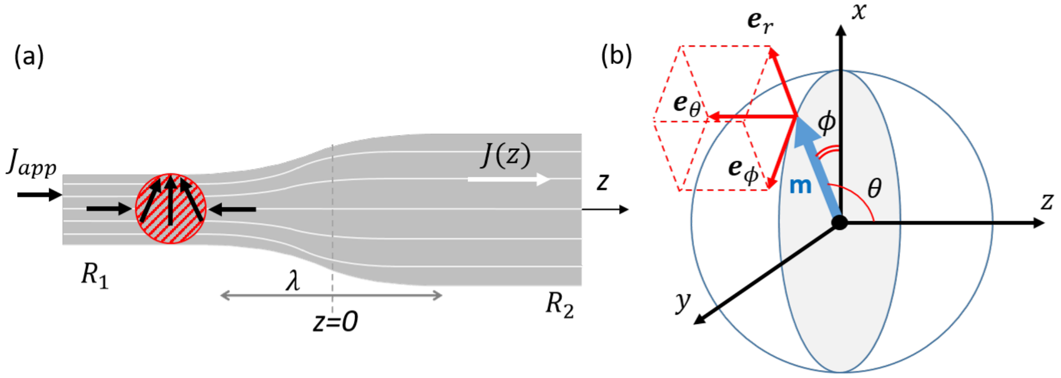

Figure 3.11: (a)Illustration of the domain wall under applied current in a modulated diameter wire. (b) Spherical coordinate basis $\{\mathbf{e}_r, \mathbf{e}_\theta, \mathbf{e}_\phi\}$ for magnetization vector $\mathbf{m}$ and Cartesian spatial coordinates x, y and z. The magnetization vector is drawn in the particular position corresponding to $\theta = \pi/2$, so that $\mathbf{e}_\theta = -\mathbf{e}_z$. Adapted from [39].

curve in figure 3.10(b)). Here we derive $z_{\text{crit}} = 0$ for $(R_2 - R_1)/(R_2 + R_1) << 1$ (the numerical solution of the equation (3.19) without this assumption gives slightly different result [63]). The corresponding critical field H_{crit} reads:

$$H_{\text{crit}} = \frac{9M_{\text{s}}(R_2 - R_1)}{5\lambda}\left(1 + \frac{10 l_{\text{ex}}^2 \pi^2}{27(R_1 + R_2)^2}\right) \tag{3.22}$$

and is depicted in figure 3.10(c) and 3.10(d) as a function of the modulation parameters. The domain wall repulsion from a modulation due H_{mod}, when not negligible, shifts H_{crit} towards higher values. Nevertheless, the analytical formula (3.22) provides a good estimation of H_{crit} and the relation between H_{crit} and geometric parameters. A key finding is that the critical field is proportional to the slope of the modulation $(R_2 - R_1)/\lambda$, with a negligibly small exchange correction for small diameters.

The comparison between analytical formula (3.22) and micromagnetic simulations reveals qualitatively similar tendencies. Moreover, small R_2/R_1 ratios and long λ, corresponding to gently sloping modulations, ensure the best fit between the simulations and the analytical expression. The cases for which the assumptions used in this model are too drastic should be covered by micromagnetic simulations.

3.4 Modulation under applied current

In this section we describe the domain wall behavior under an applied current. As previously mentionned, the motion of a transverse wall in one dimensional structures (flat strips, square and cylindrical section wire) has been described by a 1D model [27, 35, 47]. The idea is to use the same approach as this model to obtain an expression of the critical current necessary to apply in order for the TDW to pass the modulation. Hence, we will consider equilibrium states where the torque responsible for the wall motion induced by the current is exactly compensated by the one induced by the internal field. This approach is linked to the results of the previous section 3.3. We show that despite its simplicity, it succeeds to describe qualitatively and, surprisingly, quantitatively, the behavior of this critical current. We adapted this expression for the two cases of abrupt and smooth modulation previously introduced.

3.4.1 The 1D model

As previously mentionned in section 1.2, the magnetization field under an applied spin-polarized current obeys the LLG equation generalized with the spin torque

$$T_{\mathrm{ST}} = -\frac{P\mu_{\mathrm{B}}}{eM_{\mathrm{s}}}(\mathbf{j}\cdot\nabla)\mathbf{m} + \beta\frac{P\mu_{\mathrm{B}}}{eM_{\mathrm{s}}}\mathbf{m}\times(\mathbf{j}\cdot\nabla)\mathbf{m} \tag{3.23}$$

We consider the current density $\mathbf{j}$ to be stationnary. When there is a geometric modulation, the current density will adapt to it (see current density field lines in Fig. 3.11(a)).For simplicity, we assume that it is constant in a cross section and parallel to the wire axis z i.e. $\mathbf{j} = j_{\mathrm{z}}(z)\hat{\mathbf{e}}_z$. This approximation is suitable for a smooth modulation and valid away from the abrupt modulation center. As a result the LLG equation simplifies to:

$$\dot{\mathbf{m}} = -\gamma_0\mathbf{m}\times\mathbf{H}_{\mathrm{eff}} + \alpha\mathbf{m}\times\dot{\mathbf{m}} - \frac{P\mu_{\mathrm{B}}}{eM_{\mathrm{s}}}j_{\mathrm{z}}\partial_{\mathrm{z}}\mathbf{m} + \beta\frac{P\mu_{\mathrm{B}}}{eM_{\mathrm{s}}}\mathbf{m}\times(j_{\mathrm{z}}\partial_{\mathrm{z}}\mathbf{m}) \tag{3.24}$$

It is convenient to express the magnetization vector using the spherical coordinates (θ,ϕ) (Fig. 3.11(b)) which gives $\mathbf{m} = (\sin\theta\cos\phi, \sin\theta\sin\phi, \cos\theta)$. Hence, with respect to the (local) basis $(\hat{\mathbf{e}}_r, \hat{\mathbf{e}}_\theta, \hat{\mathbf{e}}_\phi)$, $\mathbf{m} = \hat{\mathbf{e}}_r$ and $\mathbf{H}_{\mathrm{eff}} = H_r\hat{\mathbf{e}}_r + H_\theta\hat{\mathbf{e}}_\theta + H_\phi\hat{\mathbf{e}}_\phi$. By using the property $\partial_\mu\mathbf{m} = \partial_\mu\theta\,\hat{\mathbf{e}}_\theta + \sin\theta\partial_\mu\phi\,\hat{\mathbf{e}}_\phi$ with $\mu\in\{x,y,z,t\}$ induced by the constant norm constraint, we get from (3.24) the following equations of motion:

$$\dot{\theta} + \alpha\sin\theta\dot{\phi} = +\gamma_0 H_\phi - \frac{P\mu_{\mathrm{B}}}{eM_{\mathrm{s}}}j_{\mathrm{z}}\partial_{\mathrm{z}}\theta - \beta\frac{P\mu_{\mathrm{B}}}{eM_{\mathrm{s}}}j_{\mathrm{z}}\partial_{\mathrm{z}}\phi\sin\theta \tag{3.25}$$

$$\sin\theta\dot{\phi} - \alpha\dot{\theta} = -\gamma_0 H_\theta - \frac{P\mu_{\mathrm{B}}}{eM_{\mathrm{s}}}j_{\mathrm{z}}\partial_{\mathrm{z}}\phi\sin\theta + \beta\frac{P\mu_{\mathrm{B}}}{eM_{\mathrm{s}}}j_{\mathrm{z}}\partial_{\mathrm{z}}\theta \tag{3.26}$$

where $H_\theta = -\frac{1}{\mu_0 M_{\mathrm{s}}}\frac{\delta\varepsilon}{\delta\theta}$ and $H_\phi = -\frac{1}{\mu_0 M_{\mathrm{s}}\sin\theta}\frac{\delta\varepsilon}{\delta\phi}$. We use the well known ansatz of the 1D model (for a head-to-head wall):

$$\theta(z,t) = 2\tan^{-1}\exp\left(\frac{z - z_{\mathrm{w}}(t)}{\Delta}\right) \tag{3.27}$$

$$\phi(z,t) = \phi_{\mathrm{w}}(t) \tag{3.28}$$

where z_{w}, ϕ_{w} and Δ are the domain wall's position, angle and width respectively. These are the so called collective coordinates [47, 97]. Here we want to emphasize that Δ is usually considered as a "slave coordinate" that depends on $\phi_{\mathrm{w}}(t)$. Here we will instead consider it as a parameter that depends on the wall position (shown later). Using (3.28) one can show (see appendix B.1) that the energy density doesn't change w.r.t. the azimuthal angle ϕ, thus $\partial_\phi\varepsilon = 0$ leading to $H_\phi = 0$. Using this ansatz, we can obtain by substitutions from (3.25) and (3.26) the well known following equations:

$$\dot{\theta} = \frac{\gamma_0}{1+\alpha^2}\alpha H_\theta - \frac{1+\alpha\beta}{1+\alpha^2}\frac{\sin\theta}{\Delta}\frac{P\mu_{\mathrm{B}}}{eM_{\mathrm{s}}}j_{\mathrm{z}}, \tag{3.29}$$

$$\sin\theta\dot{\phi} = -\frac{\gamma_0}{1+\alpha^2}H_\theta + \frac{\beta-\alpha}{1+\alpha^2}\frac{\sin\theta}{\Delta}\frac{P\mu_{\mathrm{B}}}{eM_{\mathrm{s}}}j_{\mathrm{z}}, \tag{3.30}$$

Here we applied the useful property of (3.27) which is $\partial_{\mathrm{z}}\theta = \sin\theta/\Delta$. We are interested only in the equilibrium states where the domain wall settles at a given position z_{eq}, for a given value of applied current J_{app}. Knowing that $\dot{\theta} = -\dot{z}_{\mathrm{w}}\sin\theta/\Delta$, it corresponds to the situation where the wall speed $\dot{z}_\mathrm{w} = 0$, thus $\dot{\theta} = 0$. The current density j_z is related to the applied current density J_app through $j_\mathrm{z} = R_1^2 J_\mathrm{app}/R^2(z)$. When we consider the domain wall at position $z_\mathrm{w} = z_\mathrm{eq}$ and we consider only the center of the wall, i.e. $z = z_\mathrm{w}$ (where the dipolar field is the strongest) we obtain this relation

$$J_\mathrm{app} = \frac{\gamma_0 \alpha}{(1+\alpha\beta)} \frac{e M_\mathrm{s}}{P \mu_\mathrm{B}} \frac{2R^3(z_\mathrm{eq})}{R_1^2} H_\theta(z_\mathrm{eq}) \tag{3.31}$$

where we estimated the size of the wall width $\Delta \approx 2R(z_\mathrm{eq})$ (in concordance with our simulation). Note that at the transverse wall center $\hat{\mathbf{e}}_\theta = -\hat{\mathbf{e}}_z$. In the field driven case, if we consider H_θ as an effective field such as $H_\theta = H_\mathrm{int} + H_\mathrm{app}$, the equilibrium is reached when:

$$H_\mathrm{app} = -H_\mathrm{int}(z_\mathrm{eq}) \tag{3.32}$$

We observed in simulation that the internal energy of the system as a function of the wall position does not change much as function of either the applied field or the current. This is a manifestation of a quasi-rigid motion of the wall in the sens that only geometry will deform the wall. It implies that the $\hat{\mathbf{e}}_\theta$ component of the torque exerted by the internal field H_θ (composed of exchange and dipolar contribution) is the same in both field-driven and current-driven case. It means that we can use the expressions of the applied field (3.17) and (3.22) derived in section 3.3 to estimate using (3.32), the internal field $H_\theta(z_\mathrm{eq})$ in (3.31) at the critical position $z = z_\mathrm{crit}$. This position correspond to the last position where the domain wall is at equilibrium. As a result we obtain

$$J_{crit} = \frac{\gamma_0 \alpha}{(1+\alpha\beta)} \frac{e M_\mathrm{s}}{P \mu_\mathrm{B}} \frac{2R^3(z_c)}{R_1^2} H_\mathrm{crit} \tag{3.33}$$

where $H_\mathrm{crit} \equiv H_\theta(z_c)$. For completeness, we can also obtain using (3.31) in (3.30) an expression for the frequency of rotation of the wall (knowing $\dot{\phi}_\mathrm{w} = 2\pi f$):

$$f(z_\mathrm{eq}) = \frac{P \mu_B}{4\pi e M_\mathrm{s}} \frac{R_1^2 J_\mathrm{app}}{\alpha R^3(z_\mathrm{eq})}. \tag{3.34}$$

Hence when blocked, the transverse domain wall is rotating at a fixed frequency.

3.4.2 Abrupt modulation

In the field driven case for an abrupt modulation, we derived the expression (3.17) of the critical field. It is important to note that the critical position observed in the simulations belong to the small diameter part. That is why we considered only the case where $z_\mathrm{w} < 0$ (region 1) when calculating the energy. If we also consider the case where $z_\mathrm{w} > 0$ (region 2), we obtain the following energies expressions:

$$E_1(z_\mathrm{w}) = -2\mu_0 M_\mathrm{s} H_\mathrm{app} \pi R_1^2 z_\mathrm{w} + \mu_0 M_\mathrm{s}^2 \pi R_1^2 \left(\sqrt{R_2^2 + z_\mathrm{w}^2} - \sqrt{R_1^2 + z_\mathrm{w}^2} \right) + C_1 \tag{3.35}$$

$$E_2(z_\mathrm{w}) = -2\mu_0 M_\mathrm{s} H_\mathrm{app} \pi R_2^2 z_\mathrm{w} + \mu_0 M_\mathrm{s}^2 \pi R_2^2 \left(-\sqrt{R_2^2 + z_\mathrm{w}^2} + \sqrt{R_1^2 + z_\mathrm{w}^2} \right) + C_2 \tag{3.36}$$

where $C_{1,2}$ contain the wall energy E_w and the two constants coming from E_z and E_mod. These energies are represented Fig. 3.12(a) (the constants have been neglected for the sake of lisibility). For an applied field of 20 mT and 50 mT, there exist a minimum and

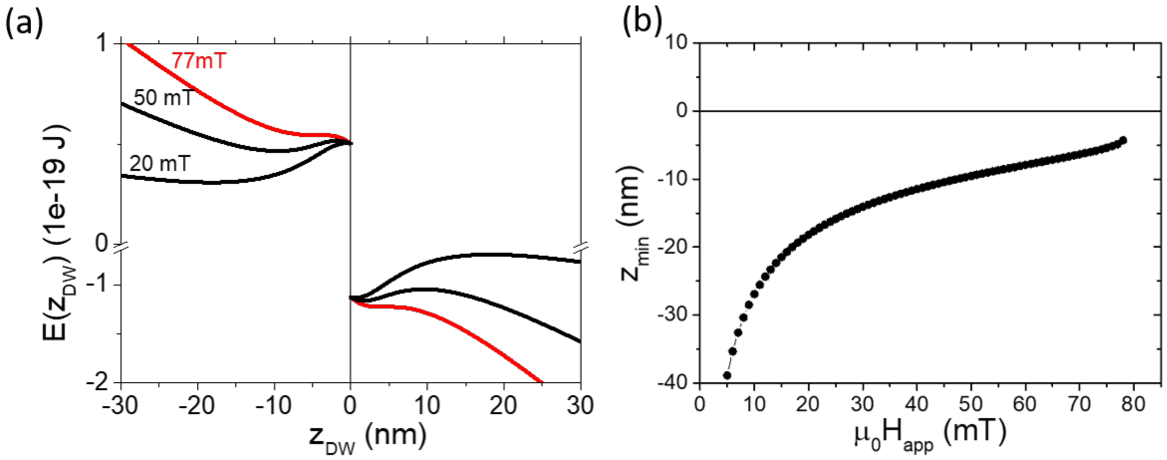

Figure 3.12: (a)Energies (3.35) and (3.36) (without constants) vs wall position for different values of applied magnetic field. The black curves correspond to cases where inflection points of both sides are non-stationary. The red curves correspond to cases where inflection point of the left side become stationary. (b) Position of minimum of energies vs the applied field. The small radius $R_1 = 5\,\mathrm{nm}$ and the large radius $R_2 = 7.5\,\mathrm{nm}$.

an inflection point on the right side as well. However, when the critical field is applied (77 mT) this inflection point also becomes stationary meaning that the domain wall cannot being trapped in the large section. Finding the minima of (3.35), we get the estimated position of the TDW as function of the applied field (shown Fig. 3.12(b)).

Under an applied current it has also been observed in simulations that for low currents, the wall can be trapped in the small section (Fig.3.13(a) top). However, for a higher current, the critical position seems to be located in the largest section region (Fig. 3.13(a) bottom). This is a consequence of the electric charge conservation, which implies a geometric dependence of the current density. Thus, the current density is reduced in the largest diameter part. Qualitatively, this situation can be mimicked using an energetic picture. Using the energies (3.35) and (3.36) we can artificially replace the H_{app} using the expressions (3.31) and (3.32) with $R(z_{\mathrm{w}}) = R_1$ and R_2 respectively. This gives us two expression for the applied field as function of the applied current density

$$H_1 = \frac{(1+\alpha\beta)}{\lambda\gamma_0\alpha}\frac{P\mu_{\mathrm{B}}}{eM_{\mathrm{s}}}\frac{1}{2R_1}J_{\mathrm{app}} \tag{3.37}$$

$$H_2 = \frac{(1+\alpha\beta)}{\lambda\gamma_0\alpha}\frac{P\mu_{\mathrm{B}}}{eM_{\mathrm{s}}}\frac{R_1^2}{2R_2^3}J_{\mathrm{app}} \tag{3.38}$$

The resulting energies are represented in Fig. 3.13(b). For low value of current (black curve), we can see the existence of two minimums, one in both regions (notice also the inflection points). It means that at low currents, the domain wall is expected to be trapped in the small diameter section. For $J = 1.3 \times 10^{11}\,\mathrm{A \cdot m^{-2}}$ (red curve), the first inflection point become stationary, but the second one is still non-stationary (the minimum still exist) which implies that the domain wall should be trapped on the large section part. For the critical current density (blue curve), the second inflection point becomes stationary which suggest the domain wall will pass the modulation. Finding the minimums of (3.35) and (3.36) with the applied fields (3.37) and (3.38) respectively, we get the estimated position of the TDW as function of the applied current density (shown Fig. 3.13(c)).

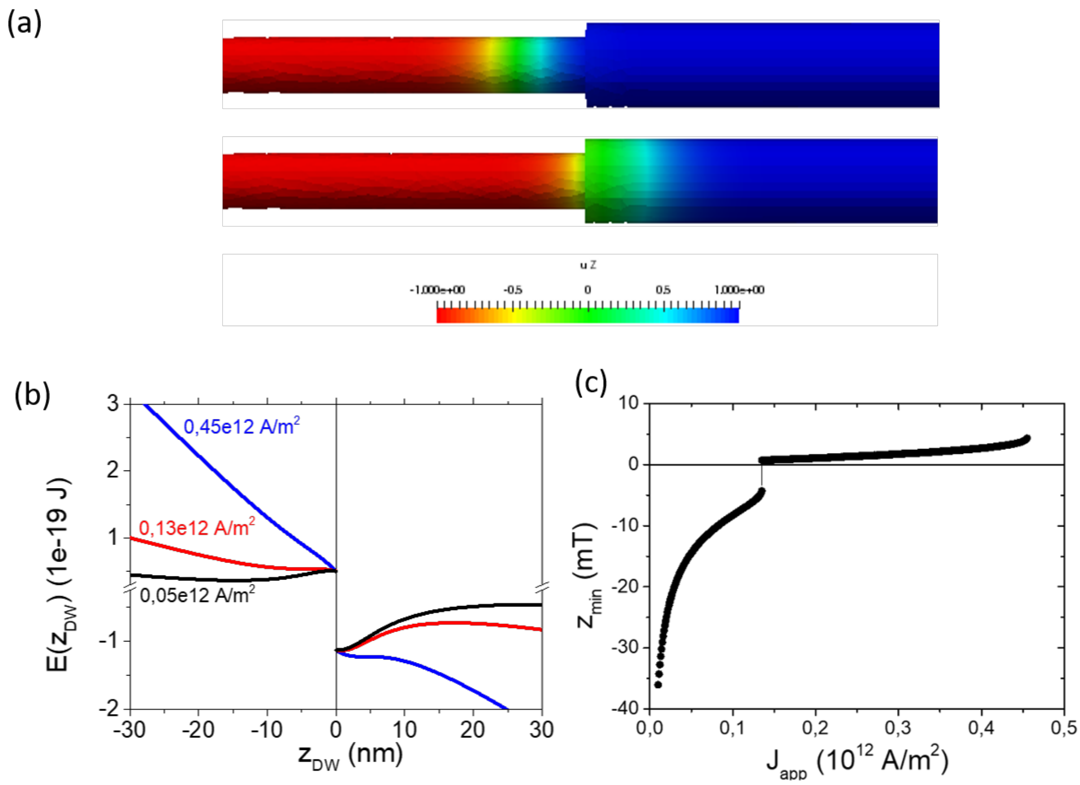

Figure 3.13: (a) TDW trapped in (top) the little section and (bottom) the large section with current density $J = 1 \times 10^{11}\,\mathrm{A \cdot m^{-2}}$ and $J = 5 \times 10^{11}\,\mathrm{A \cdot m^{-2}}$ respectively. The colorcode represent m_z.(b) Energies (3.35) and (3.36) with the applied fields (3.37) and (3.38) respectively vs wall position for different value of applied magnetic field. The black curves correspond to cases where inflection points of both sides are non-stationary. The red curves correspond to cases where inflection point of the left side become stationary. The blue curve correspond to the case where the inflection on the right side become stationary. (c) Position of minimum of energies vs the applied current. The small radius $R_1 = 5\,\mathrm{nm}$ and the large radius $R_2 = 7.5\,\mathrm{nm}$.

Knowing that the critical position of the wall is located in the large section region, we can determine the expression of the critical current for this abrupt modulation case by replacing the critical field in (3.33) by (3.17) with the positive z_{crit} (3.16) and $R(z_{\mathrm{w}}) = R_2$:

$$J_{crit} = \frac{\gamma_0 \alpha}{(1+\alpha\beta)} \frac{e M_{\mathrm{s}}}{P \mu_{\mathrm{B}}} \frac{2R_2^3}{R_1^2} \frac{M_{\mathrm{s}} |z_{\mathrm{crit}}|}{2} \left(\frac{1}{\sqrt{R_1^2 + z_{\mathrm{crit}}^2}} - \frac{1}{\sqrt{R_2^2 + z_{\mathrm{crit}}^2}} \right). \tag{3.39}$$

Comparing this expression with the simulation results (Fig. 3.14) we see a remarkably nice qualitative and quantitative match between the two. However, since we know that the estimation of the critical field seems to not give such a good quantitative match, it seems like the quantitative agreement is the result of a compensation of the errors made with the approximations of both field and current driven models.

3.4.3 Smooth modulation

In the field driven case for a smooth modulation, we derived the expression (3.22) of the critical field. By using it in (3.33), we obtain

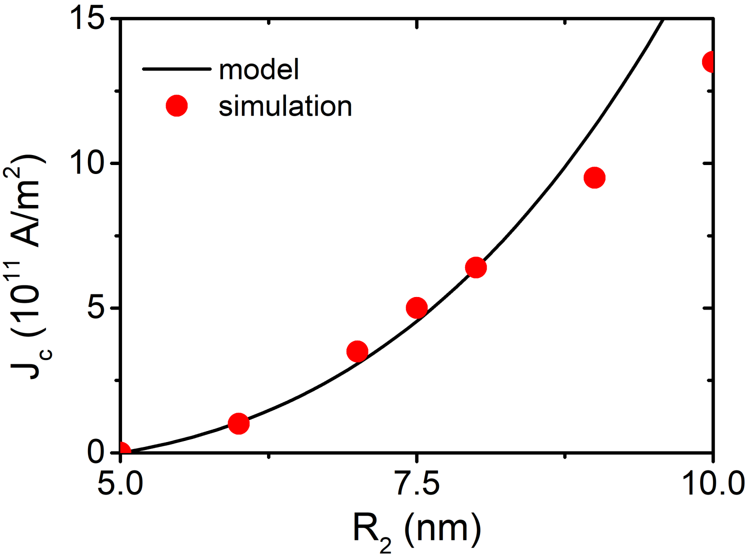

Figure 3.14: Critical current density vs radius of the large section of the abrupt modulation. The simulation results (points), expression (3.39) (solid line). The small radius $R_1 = 5\,\text{nm}$.

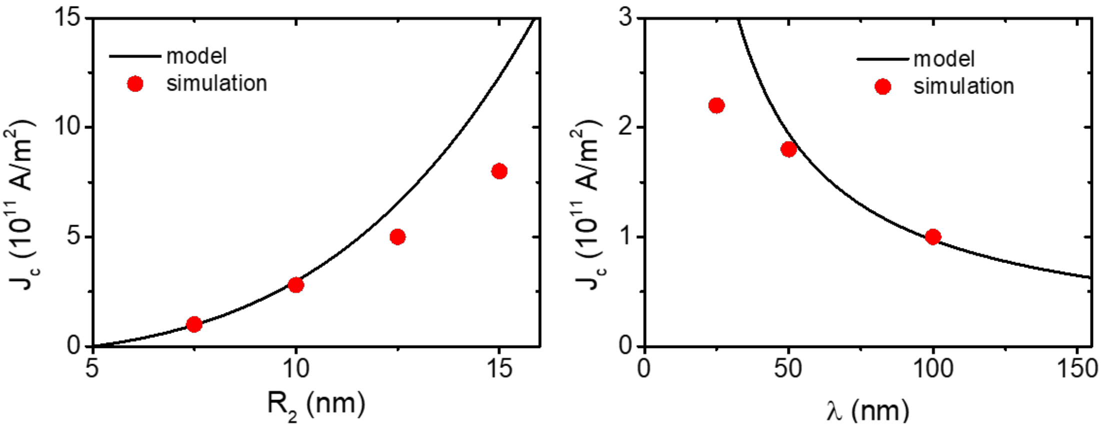

Figure 3.15: Critical current density vs (a) radius of the large section, (b) vs the modulation length. The simulation results (points), expression (3.40) (solid line). The modulation length $\lambda = 100\,\text{nm}$ for (a) and the large radius $R_2 = 7.5\,\text{nm}$ for (b). The small radius $R_1 = 5\,\text{nm}$ and $\mu_0 M_s = 1\,\text{T}$.

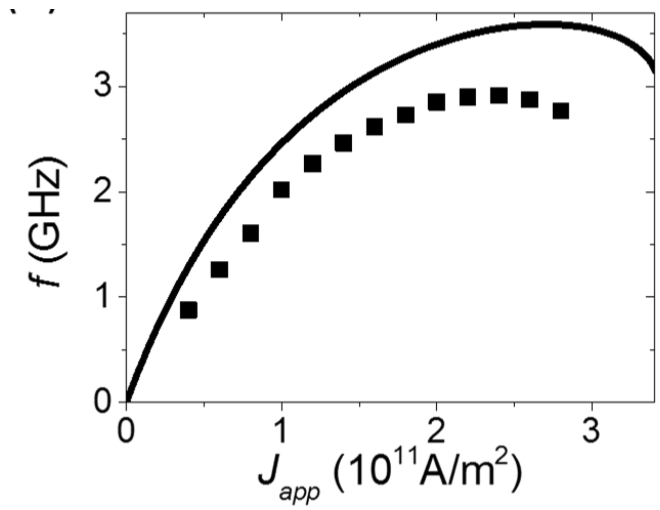

Figure 3.16: Frequencies of rotation of the TDW vs the applied current density. The solid line correspond to the equation (3.34) and the dots correspond to simulation results. The small radius $R_1 = 5\,\mathrm{nm}$, the large radius $R_2 = 7.5\,\mathrm{nm}$ and the modulation length $\lambda = 100\,\mathrm{nm}$. Adapted from [39].

$$J_{\mathrm{crit}} = \frac{9\alpha\gamma_0 e M_{\mathrm{s}}^2}{20 P \mu_{\mathrm{B}}} \frac{(R_1 + R_2)^3 (R_2 - R_1)}{R_1^2 \lambda} \left(1 + \frac{10 l_{\mathrm{ex}}^2 \pi^2}{27 (R_1 + R_2)^2}\right). \tag{3.40}$$

Here, similar to subsection 3.3.2, we have assumed $z_{\mathrm{crit}} \cong 0$, and $\Delta \cong 2R(z_{\mathrm{crit}}) = R_1 + R_2$. If we compare the domain wall behavior under applied field (Fig. 3.10(d)) and under applied current (Fig. 3.15(a)) in a smooth modulation, there is a major difference in the efficiency of the driving force in both cases. The critical field H_{crit} is almost linear with R_2 whereas J_{crit} shows a 4th order polynomial of R_2 dependence. The reason is twofold: the current density decreases and the wall width increases as the section broadens. In other words, the efficiency of spin torque decreases faster with the diameter increase than the torque exerted by an external field.

Figure 3.15 compares the analytical solution with micromagnetic simulations. The tendencies are similar, with even an excellent quantitative agreement in the limit of gentle modulation. This validates the model, and the above conclusion.

The model also predicts the frequency of precession of the transverse component of magnetization of the wall:

$$f = \frac{P \mu_{\mathrm{B}}}{2\pi e M_{\mathrm{s}}} \frac{R_1^2 J_{\mathrm{app}}}{\alpha R^2(z) \Delta}. \tag{3.41}$$

The dominant effect is that of the internal field and not of the non-adiabatic spin torque, resulting in the $1/(\alpha\Delta)$ coefficient in this equation. This frequency is shown is plotted in figure 3.16, for which similar to subsection 3.3.2, we estimated the wall-width parameter Δ as $\Delta \cong 2R(z)$. Again, a good qualitative agreement is found with numerical simulation.

3.5 Conclusion

We have derived analytical models to describe how a magnetic domain wall may go through a modulation of diameter in a cylindrical nanowire, under the stimulus of either a magnetic field or a spin-polarized current. Scaling laws obtained here may guide experimentalists in designing the modulation with desirable properties. We examined two opposite cases: the abrupt (step-like) and gently sloping modulation. For each case, we calculated analytically the threshold value of the applied magnetic field and the applied current as a function of the geometrical parameters. The relevance of the analytical results was confirmed by micromagnetic simulations, which reveal a quantitative agreement for both modulation geometries. We obtained expressions of the threshold currents that are proportional to the threshold fields, the domain wall width Δ, the factor $R^2(z)/R_1^2$ coming from the current conservation, and the spontaneous magnetization M_s. Independently on the modulation type, the critical current increases much faster as a function of the diameter difference in comparison to the critical field. It is related to the decrease of the local current density, and the increase of the domain wall width. Moreover, if we compare abrupt and smooth modulations, the critical thresholds in the first case increase faster than in the second one. In other words, the pinning occurs to be more efficient with an abrupt modulation.

Chapter 4

Œrsted field impact on the current-driven dynamics of a Bloch-point wall

This chapter is focused on the Bloch-point wall behavior in a cylindrical nanowire under applied current including spin-transfer and Oersted field effects. My theoretical work benefited from a tight interaction with experimentalists and in particular from the inputs of M. Schobitz, also a PhD student at SPINTEC. In this context, I took charge of massive micromagnetic simulations, developed a large variety of dedicated post-treatment scripts and methods for micromagnetic data, and contributed to the development of the analytical description of the Bloch-point wall behavior under Oersted field. The text of this chapter is largely adapted from an article published in Physical Review B in which I contributed, namely *Mechanism of fast domain wall motion via current-assisted Bloch-point domain wall stabilization* [62]. The text has been also extended by unpublished details and discussions in sections 4.2 and 4.5.

4.1 Motivation

The existence of the BPW was confirmed experimentally at rest in 2014 [98] using the x-ray magnetic circular dichroism photo-emission electron microscopy (XMCD-PEEM) in shadow mode (Fig. 4.1). However, the first report of its motion under magnetic field was disappointing [99]: unexpectedly, a change of topology occurs between the BPW and the TVW, expected to lead to instabilities and low speed. More recently however, we showed that the situation is drastically different for motion driven with a spin-polarized current [28]. BPWs remain stable and with speed exceeding $600\,\mathrm{m}\cdot\mathrm{s}^{-1}$, setting an experimental record for a purely STT-driven case. We also showed that the circulation of observed BPWs was deterministically linked by the last current pulses (Fig. 4.2 (a) and (b)) for an amplitude superior to a certain threshold. In fact, a BPW with a circulation negative with respect to the current direction will switch its circulation.

The current-induced dynamics of BPWs inside cylindrical nanowire has already been theoretically studied in [35] by considering the spin-transfer torque. It has been shown that during its propagation, the BPW (called vortex in that work) can change it's circulation. However, it predicted that the switch of circulation should happen for BPWs with circulation positive with respect to the current direction, thus the opposite of what is observed in the work [28]. As a result the spin-transfer torque alone can't explain

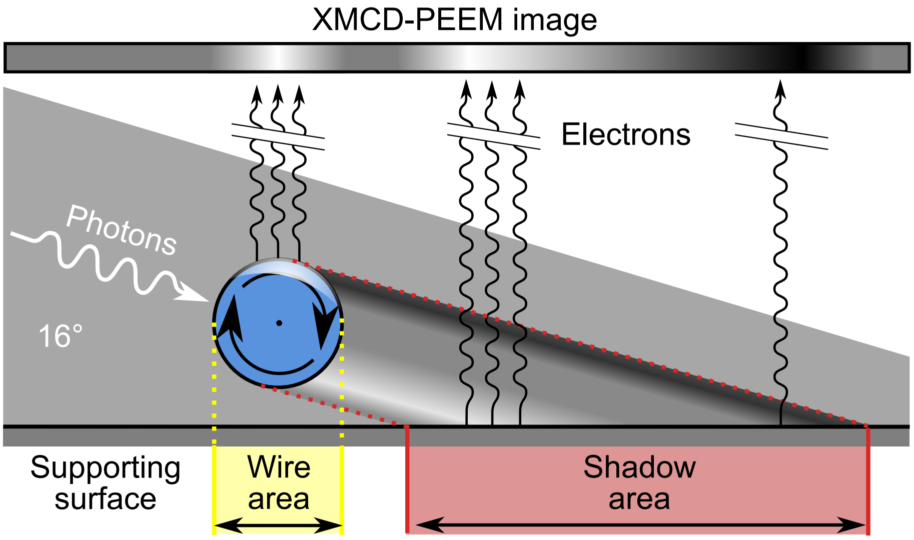

Figure 4.1: Schematic of shadow XMCD-PEEM and the contrast resulting from a BPW. Adapted from [28].

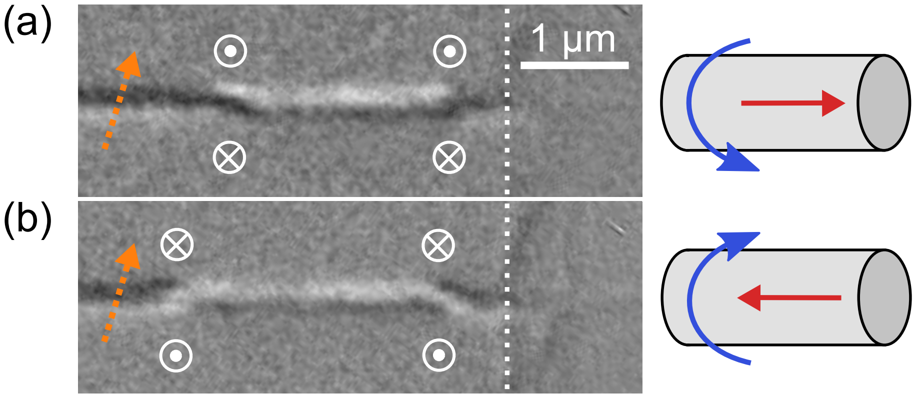

Figure 4.2: (a), (b) Consecutive XMCD-PEEM images of a nanowire with a tilted x-ray beam (orange arrow). The azimuthal circulation of the four BPWs seen in the nanowire shadow is indicated by the white arrows, consistent with the Œrsted field of the previously applied current (blue and red arrows in the right-hand schematic, respectively). From (a) to (b), a 15 ns and $1.4 \times 10^{11}\ \mathrm{A \cdot m^{-2}}$ current pulse switches 75% of BPWs. DW displacement from (a) to (b) cannot be discussed as directly resulting from spin-transfer torque, and the density of current lies below the threshold for free motion. Adapted from [28].

such behavior. This phenomenon is explained by the presence of the magnetic field generated by the current itself, the Œrsted field. Thus, the Œrsted field seems crucial for understanding the unusually-high speed of BPWs experimentally, and as such, deserves a thorough investigation.

The purpose of this chapter is to provide a comprehensive picture of the effect of the Œrsted field on domain walls in cylindrical nanowires, to set the ground for future experimental investigations, and for example guide the search for the magnonic regime occurring around $1\,\mathrm{km}\cdot\mathrm{s}^{-1}$, also called the spin-Cherenkov effect [60]. First, we examine the processes involved in the stabilization and selection of a specific circulation of the BPW, and then revisit the expected speed of BPWs under both spin-transfer and Œrsted field. For the simulations we considered two materials: $\mathrm{Fe}_{20}\mathrm{Ni}_{80}$ (permalloy) with the exchange stiffness $A_{\mathrm{ex}} = 1 \times 10^{-11}\,\mathrm{J}\cdot\mathrm{m}^{-1}$ and the spontaneous magnetization $M_{\mathrm{s}} = 8 \times 10^{5}\,\mathrm{A}\cdot\mathrm{m}^{-1}$ and $\mathrm{Co}_{20}\mathrm{Ni}_{80}$ with $A_{\mathrm{ex}} = 1.1 \times 10^{-11}\,\mathrm{J}\cdot\mathrm{m}^{-1}$ and $M_{\mathrm{s}} = 6.7 \times 10^{5}\,\mathrm{A}\cdot\mathrm{m}^{-1}$. The dipolar exchange length $l_{\mathrm{ex}} = \sqrt{2A_{\mathrm{ex}}/\mu_0 M_{\mathrm{s}}^2}$ is about 5 nm and 6.25 nm for each materials, respectively. The tetrahedrons that compose the meshes have a characteristic length of 4 nm, which is inferior to the exchange length of both materials. We considered a spin polarization rate $P = 0.7$ for both materials. In this chapter, we present results with units of length and current normalized with micromagnetic quantities, making the present work scalable to any soft magnetic material.

4.2 Transformation of the TVW into a BPW

Experimentally, soft magnetic nanowires exhibit domain walls of both TVW and BPW types, in the as-grown state as well as following ac demagnetization along a direction transverse to their axis [98, 100, 101], or motion of walls under magnetic field [99]. To the contrary, only BPWs are observed following the application of pulses of current [28], which is not explained by considering the effect of spin-transfer alone [35].

To understand this, we simulated the response of TVWs in $\mathrm{Co}_{20}\mathrm{Ni}_{80}$ nanowires subject to current pulses, taking into account the effect of the resulting Œrsted field only. We evidenced the existence of a threshold current, below which the structure of the TVW is only deformed, while above it the TVW is converted to a BPW. This occurs through the peripheral motion of the surface vortex and antivortex towards each other (Fig. 4.3(a)-(b)), until they merge, nucleating a Bloch point that then moves radially towards the axis, ending in a BPW (Fig. 4.3(c)-(d)). The BPW then reaches a steady configuration under the current pulse, and remains upon removal of the Œrsted field, with a circulation positive with respect to the direction of applied current $\mathbf{j}$. From a topological perspective, this process is similar to the dynamical transformation of a TVW subject to a longitudinal magnetic field [99]. Handwavingly, in the present case, the transformation can be understood, as the BPW and the Œrsted field share the same azimuthal symmetry, thus lowering the energy of the system against a TVW.

For a diameter of 90 nm, our simulations point at a threshold current for the TVW-BPW transformation of $2.8 \times 10^{11}\,\mathrm{A}\cdot\mathrm{m}^{-2}$. This explains why in [28], one observes only BPWs after current pulses, whose magnitude was rather around $10^{12}\,\mathrm{A}\cdot\mathrm{m}^{-2}$, suitable for the spin-transfer torque motion of domain walls.

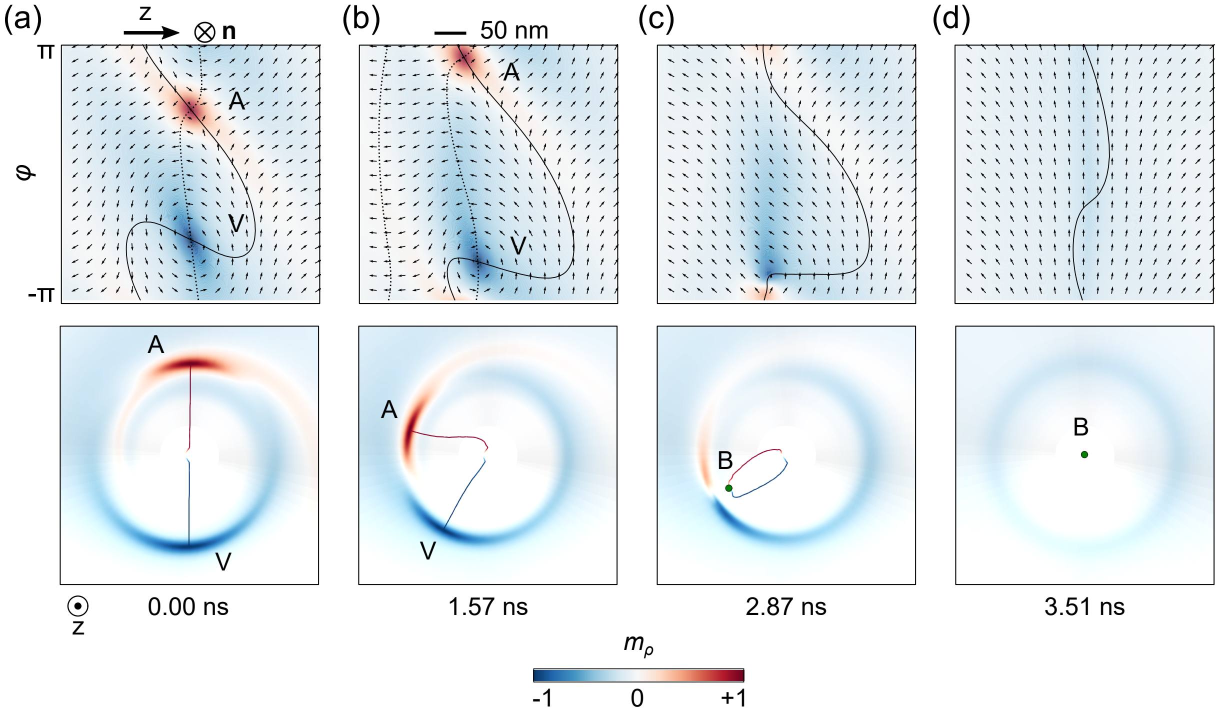

Figure 4.3: TVW transformation into a BPW under Œrsted field coming from a current density $j = 0.4 \times 10^{12}\,\mathrm{A \cdot m^{-2}}$, based on four snap shots over time (a to d), in $\mathrm{Co_{20}Ni_{80}}$ wire with diameter 90 nm. The top row consists of unrolled maps of surface magnetization, the color coding its radial component m_ρ. The dashed lines correspond to $m_\varphi = 0$ and the solid lines correspond to $m_z = 0$. The bottom row is the map of surface magnetization viewed with perspective from the inside of the wire, to which is added a volumic isoline corresponding to $|m_\rho| = 1$ and possibly a dot corresponding to the position of the Bloch-point. V and A highlight surface vortex and antivortex, respectively.

4.3 Switching of circulation of the Bloch-point wall

In this section we examine in detail the impact of the Œrsted field on the circulation of a BPW which may switch its circulation to the opposite direction. We provide a phenomenological description, a microscopic and a topological understanding, and the threshold of current required for the selection.

4.3.1 Phenomenology of the switching of circulation

We describe here what becomes of a BPW when subject to an Œrsted field, depending on its initial circulation. In the present context we define the sign of circulation with respect to the $\hat{\mathbf{e}}_\varphi$-axis, itself defined against the $\hat{\mathbf{e}}_z$ direction : for positive circulation $C+$ the azimuthal magnetization is parallel to the $\hat{\mathbf{e}}_\varphi$-axis, and for negative circulation $C-$ it is antiparallel to $\hat{\mathbf{e}}_\varphi$-axis. First we consider a head-to-head wall with no loss of generality, as a head-to-head domain wall and a tail-to-tail domain wall are equivalent through applying time-reversal and symmetry operation with respect to the xy plane. In sections 4.3.2 and 4.3.3 we nevertheless compare both. At this stage we disregard spin-transfer effects, so that following inertia-related motion in the first stages of dynamics, the walls remain immobile after reaching their final configuration.

Unless otherwise stated, the simulations have been conducted using $\alpha = 1$. This is an unphysically-large damping, however suitable to describe quasistatic situations in a realistic sample, such as pulses of current with rise time of a few nanoseconds, relevant to our experimental situation [28]. Therefore, we describe here a situation close to the minimum-energy path for magnetization processes. Considering a realistic damping value with sub-nanosecond rise time would induce complex ringing effects, like for precessional switching of macrospins [102]. We performed simulations with both wires and thick-wall tubes, leading to negligible differences. Here, we illustrate the process with a Permalloy wire with diameter 90 nm.

Figure 4.4 describes the behavior of the BPWs initially $C-$ or $C+$, while applying a positive current, thus favoring $C+$. Figure 4.4(a) qualitatively illustrates the rotation of magnetic moments in domains towards the Œrsted field at the wire surface and the evolution of the domain wall width up to the switching process. Figures 4.4(b)-(e) show the value over time of four quantities illustrating the process at play: (b) the Thiele wall parameter, (c) micromagnetic energies, the maxima and minima of the (d) azimuthal and (e) radial components of magnetization at the external surface. The BPW with initially positive circulation increases its width, reaching a plateau after about 0.5 ns (Fig. 4.4(b)). This is explained by the tilt of magnetization towards the azimuthal direction in the domains, thereby lowering the effective anisotropy inside the domain wall against the azimuthal direction, and thus increasing its width. The tilt reflects in the initial variation of $\max(m_\varphi)$ also evidenced for $C-$ (Fig. 4.4(d)), which is discussed in more detail in Appendix C.3. The exchange energy increases as domains display a partial curling, the dipolar energy decreases as the head-to-head wall gets wider, and the Zeeman energy due to the Œrsted field decreases both in the domains and in the domain wall. The behavior of the BPW with negative circulation depends on the magnitude of the current. Below a critical current density J_c, the BPW contracts until it reaches a stable width. Above this threshold, the wall width decreases further until it reaches a minimum, before increasing rapidly towards the width of the BPW with positive circulation, all energies also coinciding (Fig. 4.4(c)). This suggests a reversal of circulation of the wall, con-

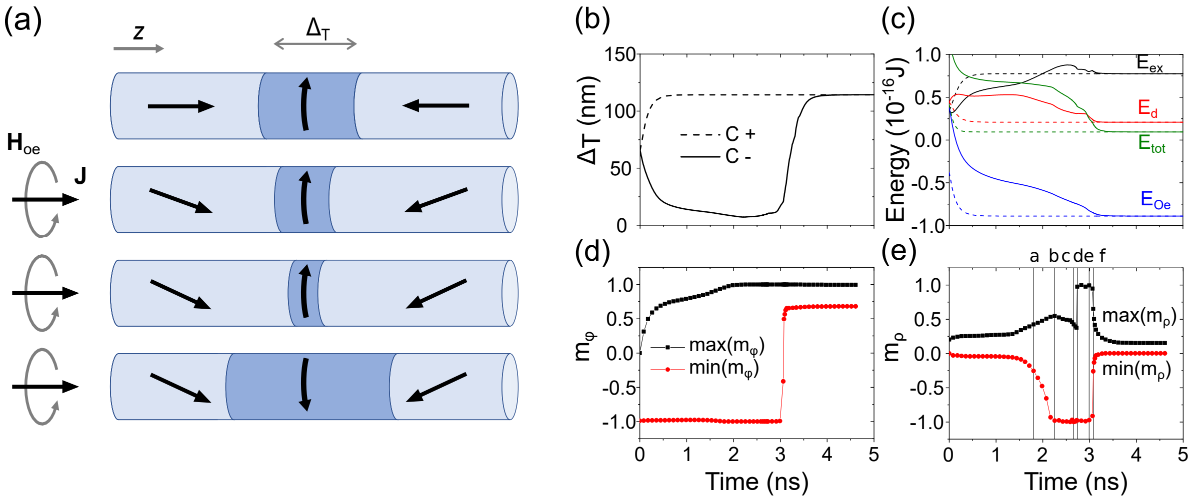

Figure 4.4: (a) Schematic of the circulation switching for a BPW initially $C-$. (b)-(e) Time evolution of four quantities illustrating the response of BPWs under the Œrsted field in a permalloy wire with diameter 90 nm and the applied current density $1.2 \times 10^{12}\,\mathrm{A \cdot m^{-2}}$, corresponding to an Œrsted field of 34 mT at the external surface: (b) the Thiele wall parameter, (c) micromagnetic energies, and the maxima and minima of the (d) azimuthal and (e) radial components of magnetization at the surface of the wire. The a, b, c, d, e, f labels correspond to timestamps of Fig.4.5. The solid line stands for initially negative circulation $C-$ and dashed line for initially positive positive circulation $C+$. Adapted from [62].

firmed by Fig. 4.4(d): in the initial state $\min(m_\varphi) = -1$ reflects the negative circulation, while $\max(m_\varphi) = 0$ reflects magnetization in the domains. In the final state, *i.e.*, after switching, $\max(m_\varphi) = +1$ now reflects the positive circulation, while $\min(m_\varphi)$ reflects the tilted magnetization in the domains. The variation of the radial component m_ρ is by far more complex (Fig.4.4(e)), suggesting a non-trivial switching process, detailed in the next section.

4.3.2 Details of the circulation switching mechanism

The BPW texture displays the rotational symmetry at rest. This symmetry is not conserved through the switching process, which is far from a simple coherent rotation of the wall's inner degree of freedom. The nontrivial evolution in time of the out-of-plane magnetization component m_ρ is illustrated in Figure 4.5. To follow the magnetization transformation both at the wire surface as well as in the volume we plotted the unrolled maps of m_ρ on the external wire surface (top row) and the same m_ρ surface maps seen from inside as a 3D view, completed with BP trajectories in the volume (bottom row).

Under the applied current, [Fig.4.5(a)], magnetization in the domains rotates towards the azimuthal direction to follow the Œrsted field. Given the azimuthal rotation in the domains, the surface map has some similarity with a 180° domain wall in a thin film, made of a central micro-domain delimited by $m_\varphi = 0$ isovalues (dashed back lines) and surrounded by two 90°-like walls. The central micro-domain is characterized by an outward radial component ($m_\rho > 0$), a well-documented fact [11, 60] for a wire at equilibrium and visible on Fig.4.4(e) at $t = 0$. Its sign results from positive magnetic charges of the head-to-head domain wall considered. On Fig.4.5(a) an instability is developing, with locus of maximum or minimum of m_ρ at $m_\varphi = 0$. At these locations the torque due to Œrsted field is maximum as it is perpendicular to the local magnetization.The instability

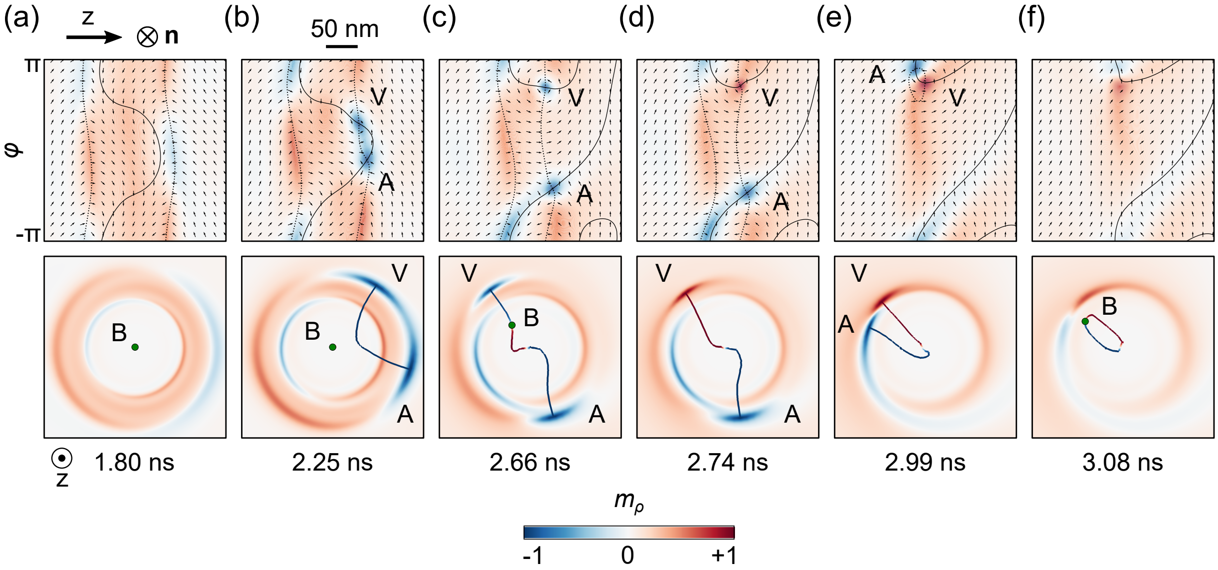

Figure 4.5: Snapshots illustrating the switching mechanism of BPW circulation in a permalloy wire with diameter 90 nm, for applied current amplitude $j = +1.2 \times 10^{12}\,\mathrm{A \cdot m^{-2}}$. (a)-(f) correspond to the time labels in Fig.4.4(e). Top row: unrolled maps of m_ρ at the wire surface. **n** indicates the direction of the outer normal of the wire surface. Dashed lines correspond to $m_\varphi = 0$ isovalues. Solid lines correspond to $m_z = 0$ isovalues. Bottom row: same surface maps of m_ρ seen from inside of the wire as a 3D view. Colored lines correspond to $|m_\rho| = 1$ isovalues. Green dots show the position of the BP. V and A highlight surface vortex and antivortex, respectively. Adapted from [62].

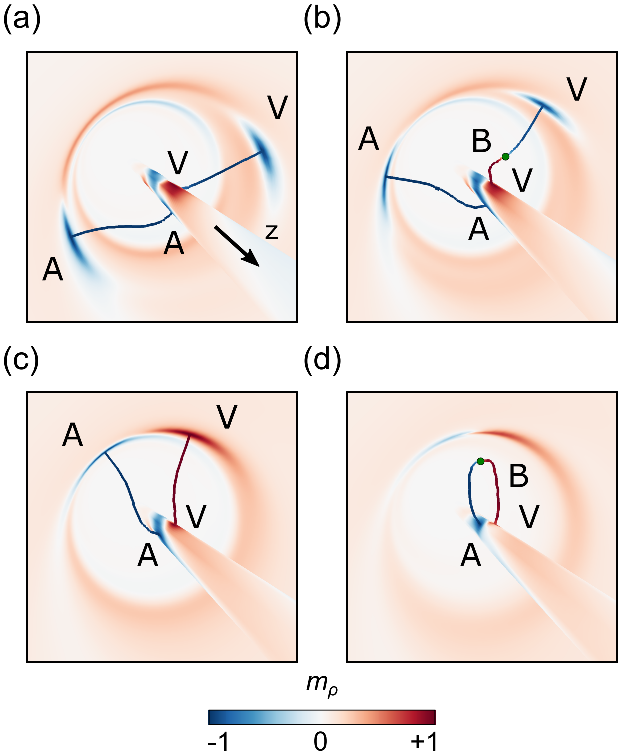

Figure 4.6: Snapshots illustrating the switching mechanism in a permalloy tube with diameter 90 nm for applied current amplitude $j = +1.0 \times 10^{12}\,\mathrm{A \cdot m^{-2}}$. The m_ρ colored maps seen from inside of the tube are the counterparts of Fig.4.5. Colored lines correspond to $|m_\rho| = 1$ isovalues. Green dots show the position of the BP. V and A highlight surface vortex and antivortex, respectively. Adapted from [62].

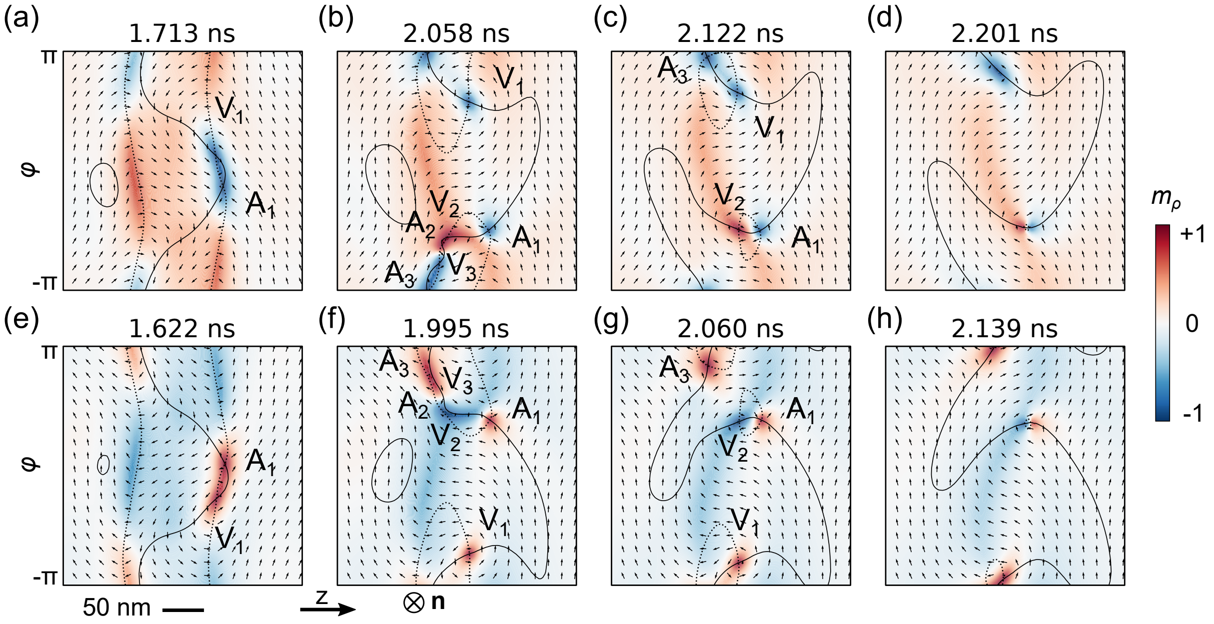

Figure 4.7: Unrolled m_ρ colored maps at the wire surface illustrating the switching mechanism in a permalloy wire with a head-to-head BPW (top row) and tail-to-tail BPW (bottom row). In both cases the circulation is initially negative $C-$, while the Œrsted field direction promotes positive circulation $C+$. Dashed lines correspond to $m_\varphi = 0$ isovalues. Solid lines correspond to $m_z = 0$ isovalues. V and A highlight surface vortex and antivortex, respectively. The normal **n** indicates the direction of the outer normal to the wire surface. All maps are plotted for the wire diameter 90 nm and for applied current amplitude $j = +1.4 \times 10^{12}\,\mathrm{A \cdot m^{-2}}$, corresponding to an Œrsted field of 39.5 mT at the external wire surface. Adapted from [62].

is accompanied with the deformation of the $m_z = 0$ isoline (solid black line). This behavior is consistent with the physics of walls in thin films, which tend to be of asymmetric Néel type or Bloch type to reduce the magnetostatic energy [95].

When reaching locally $|m_\rho| = 1$, the instability develops in a pair of vortex (V) and antivortex (AV) at the wire surface [Fig.4.5(b)]. This corresponds to event b on Fig.4.4(e), following a progressive decrease of min(m_ρ) and reflecting the rise of the instability. For topological reasons (discussed in the next section), these V and AV result from the continuous deformation of the ground state and thus share the same polarity (the same sign of m_ρ). The polarity happens to be negative, possibly because it allows to decrease the demagnetizing energy. Then, the V and AV move away one from another along the wire perimeter, which leaves in-between an area largely parallel to the magnetization direction in the domains [Fig.4.5(c)]. The phenomenon at play is clear: it is similar to a nucleation-propagation process, however not for an extended domain, but for the internal degree of freedom of a domain wall, such as the switching of the core of a vortex [50], or of the Néel cap in a Bloch wall [103].

The isolines $|m_\rho| = 1$ in the 3D view allows to track the extent of the radial pocket inside the wire. From Fig.4.5(b) to (c) (bottom row), it extends towards the axis, eventually reaching the existing Bloch point. After that, the Bloch point starts to move along this isoline towards the surface vortex, until it vanishes from the volume. The latter event [Fig.4.5(d)] is accompanied with the change of the vortex polarity. In Fig. 4.4(e) this event correspond to the abrupt change in max (m_ρ) due to the small size of the BP, and the instantaneous character of a change of topology. At this stage the wall is of transverse-vortex type, for which the transformation back to the Bloch point under external stimulus is similar to the situation described in Ref. [104]: the V and AV move further along the wire perimeter, until they merge [Figs.4.5(e),(f)]. This corresponds to event f on Fig.4.4(e), which this time is associated with merge of V and AV of the same polarity and thus the creation of a BP. Finally, the new BP moves towards the center of the wire, ending in an immobile BPW with positive circulation.

We highlight below a few other features of the switching mechanism. First, it is similar in thick-walled tubes, except the lack of the BP in the volume originally [Fig.4.6(a)]. The latter implies the additional step of a BP nucleation by means of V/AV pair creation and transformation [Fig.4.6(b)] at the inner surface. Then the BP travels towards the outer surface[Fig.4.6(c)]. Later a new one is created, travels towards the inner surface and annihilates[Fig.4.6(d)].

Second, the mechanism may become more complex for higher current densities, implying several pairs of V/AV. For example, Fig.4.7(a)-(d) show the case of a permalloy wire with diameter 90 nm and $j = 1.4 \times 10^{12}\,\mathrm{A \cdot m^{-2}}$. The switching process now involves two pairs of V/AV. One pair interacts first with the BP on the axis, switching the polarity of the vortex. At the end of the process the V/AV pair with the same polarity does not nucleate a BP, while the V/AV with opposite polarity does, leading again to the same final state, a BPW with positive circulation.

Third, Figure 4.7(e)-(h) also illustrates the equivalence of behavior of head-to-head and tail-to-tail domain walls, as expected. The situations displayed in the top and bottom rows of Fig.4.7 are equivalent through applying two symmetry operations: time-reversal (reversing both magnetization and applied current) and mirror symmetry around a plane containing the axis (*e.g.*, flipping top and bottom in the surface maps displayed). Accordingly, it can be checked that the top and bottom rows are equivalent under these two symmetries.

4.3.3 Topological description of the switching of circulation

In this section we analyze the switching process from a topological point of view. To do so, we calculate the so-called *winding numbers*, which measure the magnetization vector curling. This allows one to establish general features for the switching process.

For isotropic spherical spins, parametrized as $\mathbf{m} = (m_1, m_2, m_3)$, the S^2-winding number reads [105], [106]:

$$w = \frac{1}{4\pi} \int_M \mathbf{m} \cdot (\partial_1 \mathbf{m} \times \partial_2 \mathbf{m})\, dx_1 dx_2, \tag{4.1}$$

where x_1 and x_2 are arbitrary curvilinear coordinates in real space, and $\partial_i = \partial / \partial x_i$. In Cartesian coordinates this expression is often referred to as *skyrmion number*. The manifold M is usually understood to be either the compactified plane $\mathbb{R}^2$ (V and AV in a thin film), or a 2-sphere $\mathbb{S}^2$ (BP in the volume).

In practice, the application of Eq.4.1 to the surface texture with possibly a V or AV yields locally a half-integer number $w = qp/2$, where q is usually referred to as the topological charge (or topological vorticity, or S^1-winding number), and p the polarization [107]. V and AV are characterized by opposite topological charges: $q = +1$ and $q = -1$, correspondingly. The positive polarization $p = +1$ indicates the parallel alignment of the V/AV core with the outer normal and the negative $p = -1$ indicates the antiparallel alignement. The pair of V/AV with the same polarity has total $w = 0$ and thus may be deformed continuously into an uniform state. In the case of BP texture in volume, Eq.4.1 yields $w = \pm 1$, where positive sign indicates tail-to-tail BP type and negative sign head-to-head type.

In our study we consider topological objects in the volume (BP) and at the wire surface (V/AV). Strictly speaking, their winding numbers obtained with the same Eq.4.1 cannot be directly compared, and their sum should not obey any conservation law due to their contrasting geometrical nature. Conservation law may be established, for example, for purely flat nanomagnets which topological objects share the same manifold [108]. Nevertheless, the assessment of the total winding number change at the surface w_{surf} and, separately, in the volume w_{vol} reveals empirical rules for all switching processes described in this paper.

All snapshots in Figure 4.5 may be classified into three topological situations: the BP is in the volume (a)-(c), the BP left the volume and caused a change of V polarity (d)-(e), the BP reenters the volume (f). Corresponding winding numbers are summarized in Table 4.1.

Table 4.1: Winding numbers calculated for Figure 4.5.

figure labels	(a), (b), (c)	(d), (e)	(f)
ω_{surf}	0	+1	0
ω_{vol}	−1	0	−1

The change in w_{surf} and w_{vol} between (c) and (d) events, as well as between (e) and (f) events obeys

$$\Delta\omega_{\mathrm{surf}} = \Delta\omega_{\mathrm{vol}}. \tag{4.2}$$

This condition is also followed for thick-walled tubes [Fig.4.6] in the presence of inner and outer tube surfaces with normals pointing, correspondingly, towards negative and positive ρ-direction. Corresponding winding numbers are summarized in Table 4.2.

Table 4.2: Winding numbers calculated for Figure 4.6.

figure labels	(a)	(b)	(c)	(d)
$\omega^{\mathrm{in}}_{\mathrm{surf}}+\omega^{\mathrm{out}}_{\mathrm{surf}}$	$0+0$	$-1+0$	$-1+1$	$-1+0$
ω_{vol}	0	−1	0	−1

Moreover, the condition Eq.4.2 is also satisfied in the case of multiple V/AV pairs formation, which happens with rising current amplitude. Figure 4.7 illustrates the situation for which the initial instability creates the first V/AV pair of V and AV of the same polarity similar to Fig.4.5 and further evolves towards a more complex texture with two extra V/AV pairs identified by $m_z = 0$ and $m_\varphi = 0$ isolines crossing. The shared polarity of each new V/AV pair is not necessarily the same as for the previously created pair. Moreover, in most cases we note that each additional pair has opposite polarization with respect to the previous pair, which is consistent with the hypothesis of the overall out-of-plane component minimization and the reduction of associated demagnetizing field penalty in the system. The corresponding winding numbers assessment is summarized in Table 4.3.

The situation looks equivalent for head-to-head and tail-to-tail BPWs, except that in the first case the BP interacts with a V by changing its polarity and in the second case with an AV in order to satisfy Eq.4.2. No matter how many intermediate V/AV pairs

Table 4.3: Winding numbers calculated for Figure 4.7.

figure labels	(a), (b)	(c)	(d)	(e),(f)	(g)	(h)
ω_{surf}	0	+1	0	0	−1	0
ω_{vol}	−1	0	−1	+1	0	+1

were created during the switching process, the starting V/AV creation and final V/AV annihilation events always follow the same pattern.

The V/AV pair creation implies the additional exchange energy cost [Fig. 4.4(c)], and thus the threshold to be overcome for BP circulation switching. In the next section we calculate the corresponding critical current.

4.3.4 Critical current density of the switching of circulation

Here we are interested in describing the minimum current J_c required to switch the circulation of a BPW, from initially antiparallel to parallel to the Œrsted field. The determination of a switching threshold against field or current is a delicate issue in numerical micromagnetism. Indeed, the computation time needs be finite in practice, so that a criterium is required to decide whether switching would not occur for a more extended time. A standard method to circumvent this difficulty is through performing a scaling of a parameter, for instance susceptibility below the threshold [109, 110], or the switching time about the threshold [111, 112]. An interpolation through a few points and intercept with an axis then provides the threshold with high accuracy. In the present case, we consider the critical time τ_c required for switching, above the threshold current.

The first step is to exhibit a criterium to define τ_c, as the complex and parameters-dependent dynamics revealed in section 4.3.2 does not leave us with an ubiquitous one. After examination of various possibilities, the most robust choice turned out to be the time it takes for $\min(m_\varphi)$ at the external surface of the wire to change sign, directly highlighting the change of BPW circulation. In practice, the precise time for the change of sign is derived by fitting the curve in Fig.4.4(d) using an atanh function.

The second step is to perform an interpolation, which requires a guess for the associated scaling law. A simple physical view is the following: the threshold current J_c is associated with a critical slowing down of dynamics, and thus to the divergence of the characteristic time. A current density j applied above the threshold suddenly brings the system out-of-equilibrium, giving rise to an effective field linear with $j - J_c$, to first order. The associated Kittel precessional frequency is expected to scale with this quantity, so that the switching time shall scale with $(j - J_c)^{-1}$. The inverse critical time indeed behaves fairly linearly versus the current density whatever the material or geometry, wire or tube [Fig.4.8(a)]. The slight curvature arises probably because the Kittel's view for precession is too crude for the highly non-uniform process considered. To account for this curvature, in practice we used the phenomenological scaling law to fit these plots and extract precisely J_c:

$$\tau_c = \sigma_0 (j - J_c)^{-p} \tag{4.3}$$

In order to come closer to the experimental case, we considered more realistic damping parameters α, and also the effect of spin transfer, besides the Œrsted field [Fig.4.8(b)]. The switching time is largely affected by these parameters, however the threshold current J_c is not. This shows that the present results remain valid even for current pulses with a

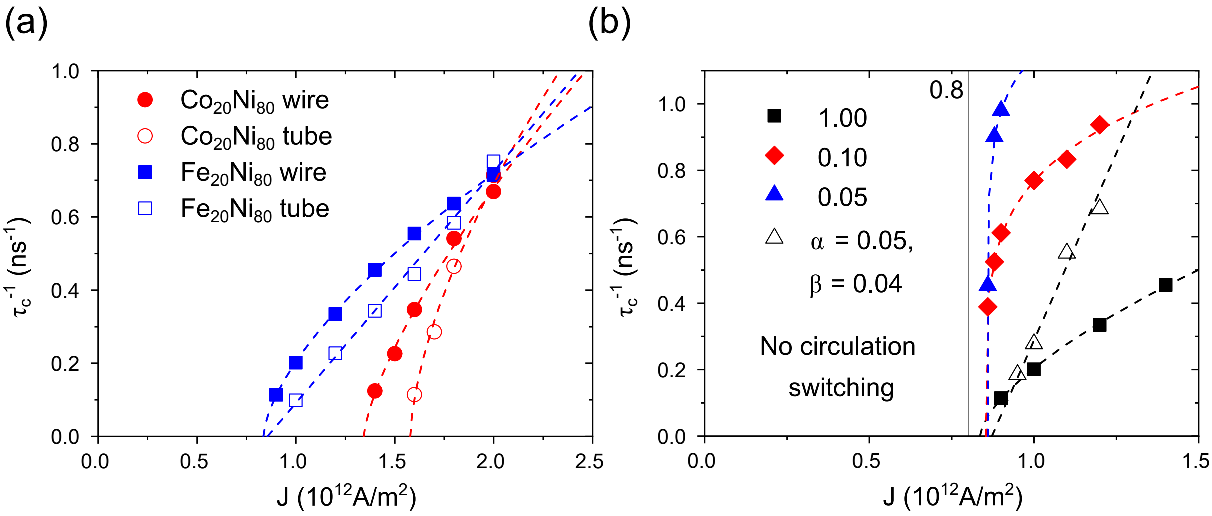

Figure 4.8: Inverse switching time versus applied current density, for nanowires (full symbols) or nanotubes (open symbols) of external diameter 90 nm and composition either $Fe_{20}Ni_{80}$ or $Co_{20}Ni_{80}$. The dashed lines corresponds to the fit using the power law of Eq.4.3. (a) Comparison for wires and tubes, with $\alpha = 1$. (b) Comparison for several α values without and with spin-transfer torque effect for $Fe_{20}Ni_{80}$. Adapted from [62].

sub-ns rise time, and that the Œrsted field is indeed the crucial and largely dominating reason for the switching of circulation.

Finally, to provide a complete view of the switching process, we evaluated the threshold current J_c against the radius R, illustrated on Fig.4.9(a) based on tubes. Plotting J_c against $1/R^3$ reveals a close-to-linear law [Fig.4.9(b)]:

$$J_\mathrm{c} \approx C\frac{A}{\mu_0 M_\mathrm{s} R^3}, \tag{4.4}$$

with C a dimensionless coefficient. This scaling law is supported by an analytical model balancing exchange with Œrsted Zeeman energy in the wire geometry (Appendix C.3), and partly by dimensional analysis (Appendix C.2). Let us comment the impact of this result. First, Eq.4.4 is valid for any magnetically soft material, upon the proper scaling of length and current density (Appendix C.1):

$$\tilde{j}_\mathrm{c} = (C/2)r^{-3}, \tag{4.5}$$

with $r = R/\ell_\mathrm{ex}$ the dimensionless radius. This law predicts a switching current only 20 % larger than the experimental one. We consider that this is a fair agreement, considering error bars on exchange stiffness, material composition, and possible sample defects or the role of temperature during the current pulse in the experiments. Second, the switching current reaches experimentally unpractical values below $R \approx 30\,\mathrm{nm}$ (circa $6\ell_\mathrm{ex}$). This means that the investigations published previously and neglecting the Œrsted field remain valid in the low-radius regime, the circulation of BPWs tending to switch positive with the direction of wall motion [11, 60], thus with the flow of electrons and hence negative with the direction of current. Also, there must exist a threshold regime where the effect of the Œrsted field and the chirality of the LLG equation compete, leading to an unpredictable circulation and wall speed. Conversely, for large radius note that the azimuthal tilt of magnetization in the domains scales with the same $1/R^3$ law (see Appendix C.3). This means that circulation switching should have no limit for large radius, occurring always for the same wall angle, around 270° following Fig.4.4.

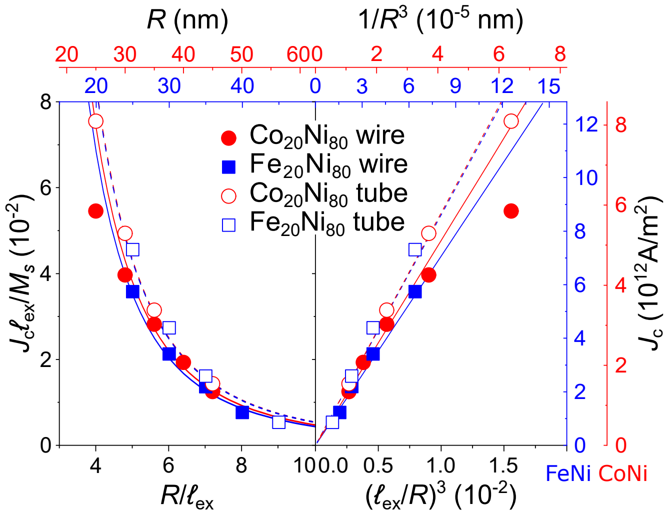

Figure 4.9: Critical current density J_c in nanowires versus (a) their radius R and (b) $1/R^3$. The dashed lines (tubes) and solid lines (wires) correspond to Eq.4.4. For tubes, $C = 10.73$ and 10.82 for $Fe_{20}Ni_{80}$ and $Co_{20}Ni_{80}$ respectively. For wires, $C = 8.81$ and 9.54 for $Fe_{20}Ni_{80}$ and $Co_{20}Ni_{80}$ respectively. For Bottom and left axis display dimensionless quantities, while top and right axis provide real quantities for the two material considered, $Fe_{20}Ni_{80}$ and $Co_{20}Ni_{80}$. Adapted from [62].

4.4 Spin-transfer-driven motion on the BPW under Œrsted field

The Œrsted field proves crucial in experiments to stabilize BPWs, and it selects a sign of circulation of the BPW opposite to the one expected from the chirality of the LLG equation during motion, if the current is large enough [35]. Yet, the Œrsted field does not break the symmetry between the two domains, and thus cannot drive a steady-state motion, for which spin-transfer torque remains crucial. Here we bring together the two effects, to elucidate to which extent the speed predicted so far based on spin-transfer alone, remains relevant. As discussed in 2.5, to avoid the numerical pinning of the BPW subjected to electrical current we substitute the wire by a thick-walled tube of the same diameter with a PBPW. Figure 4.10(a) plots the PBPW speed v as a function of applied current, including spin-transfer and Œrsted field effects. For simplicity we start directly with the PBPW circulation favorable to the Œrsted field to avoid the circulation switching. For current amplitudes relevant experimentally, the PBPW dynamics obeys the steady regime equation

$$\mathbf{v} = \frac{\beta}{\alpha}\mathbf{u}. \tag{4.6}$$

We attribute the discrepancies between Eq.4.6 and micromagnetics at high speeds to usual numerical artifacts related to the energy over-dissipation [37]. As expected, we did not observe any signature of Walker breakdown and did not find any significant change in velocity related to the presence of the Œrsted field, as illustrated in Fig.4.10(b).

4.5 Domain wall inertia

When a current is applied, we have shown that the Œrsted field will cause an expansion or a contraction of a BPW depending on its circulation (sec. 4.3.1). While the current in

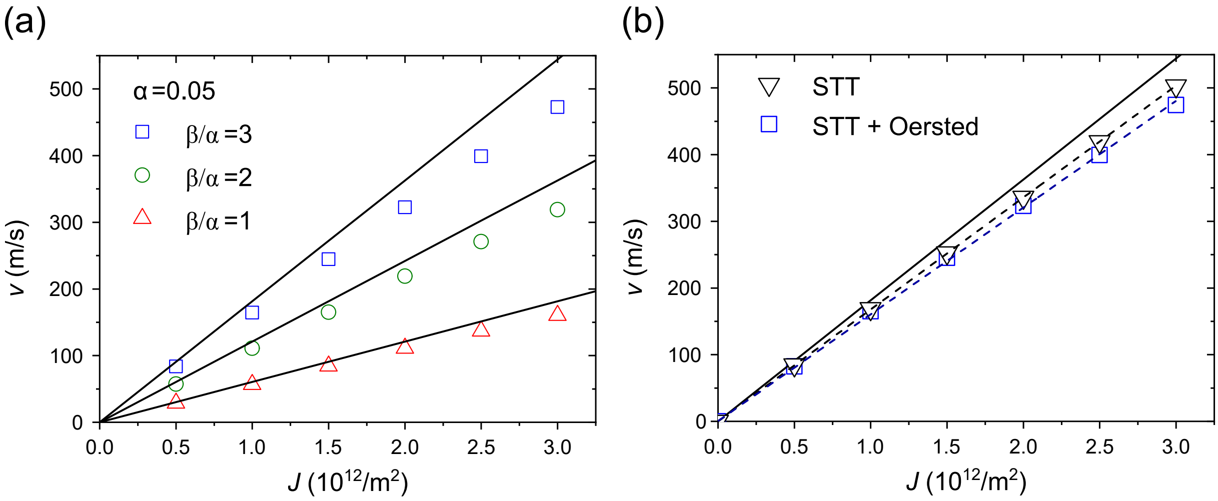

Figure 4.10: BPW speed vs applied current density for $Co_{20}Ni_{80}$ thick-walled tube with outer diameter 90 nm and inner diameter 10 nm. Solid black lines correspond to Eq.4.6. (a) Both spin-transfer and Œrsted effects are considered for different values of β/α and $\alpha = 0.05$. (b) Comparison between purely spin-transfer case and spin-transfer together with Œrsted field case for $\alpha = 0.05$ and $\beta = 0.15$. The dashed line is a linear fit. Adapted from [62].

simulations is continuously applied at the same amplitude (DC current), experimenters use current pulses. During a pulse, the domain wall will reach a propagation state of higher energy than the initial equilibrium state. At the end of the pulse, the domain wall will relax toward a lower energy state (the initial equilibrium state but shifted in position). During this relaxation process, the wall will continue to move due to its inertia. It is therefore important to know how the BPW behaves under the inertia when the current amplitude has reached zero. I simulated two BPWs of different circulation in a $Fe_{20}Ni_{80}$ thick-walled tube with outer diameter 90 nm and inner diameter 10 nm. I considered an applied current $j = 0.8 \times 10^{12}\,\mathrm{A \cdot m^{-2}}$ (inferior to the critical current for the case of negative circulation) for a duration of few nanoseconds, sufficient to reach a stationary propagation state, before cutting it off. The evolution of the position of both BPW with opposite circulation is shown in Fig.4.11. After that the current has been cut off, we can see (blue and red lines) that each wall propagates, due to inertia, for a duration inferior to the nanosecond until it stops, reaching an equilibrium position. The direction of propagation under the inertia is circulation dependent: if the circulation is negative (respectively positive), the BPW propagates in the same (resp. opposite) direction as the one of the electron flow. This result is expected from the LLG equation chirality. We also see that the resulting displacement increases when the damping parameter α decreases, giving an order of magnitude that goes from few tens of nanometers to 100 nm.

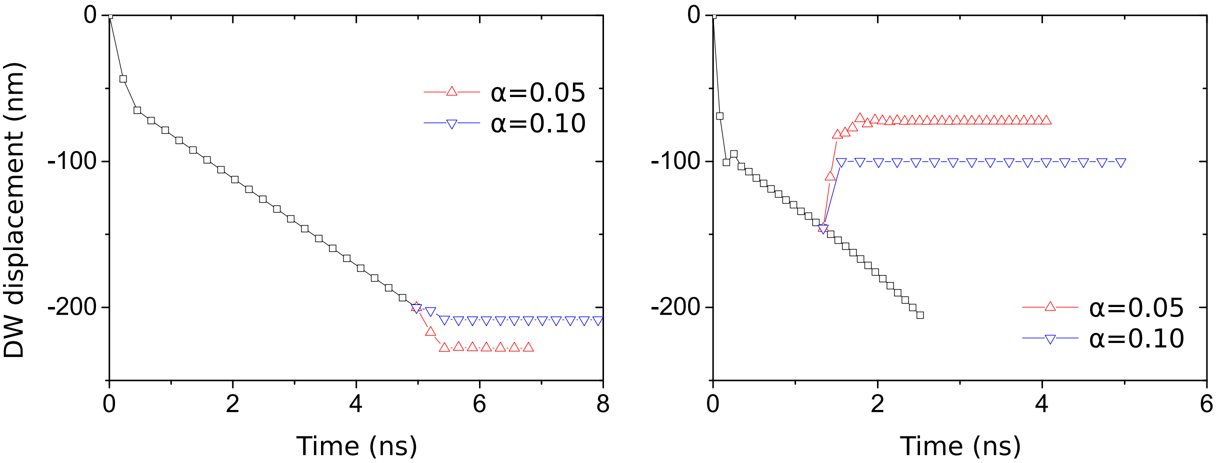

Figure 4.11: Bloch-point wall's position vs time for (a) negative circulation, (b) positive circulation. The black line with squares corresponds to the case with the current applied $j = 0.8 \times 10^{12}\,\mathrm{A \cdot m^{-2}}$, and the lines with triangles correspond to the case without current for two values of alpha. The system is a thick-walled tube of external diameter 90 nm and internal diameter 10 nm.

4.6 Conclusion

We reported recently the key role played by the Œrsted field in cylindrical soft magnetic nanowires, to stabilize Bloch-point walls (BPWs) and reach speed $> 600\,\mathrm{m \cdot s^{-1}}$ through spin-transfer torque [28].

Using micromagnetic simulations, we considered a transverse-vortex wall under the influence of the Œrsted field and showed that it transformed itself into a Bloch-point wall with the same circulation as the field. This transformation is characterized by the motion of both the vortex and the anti-vortex that constitute the wall, toward each other. It is then followed by their annihilation which inject a Bloch-point (preserving the wall polarity) inside the volume. The threshold current that triggers this transformation was found to be one order magnitude lower than the current values used in the experiment [28]. This shows that the Œrsted field stabilizes the Bloch-point wall type.

We then considered a Bloch-point wall under the influence of the Œrsted field for both circulations. For both cases, the magnetization in the domains tends to align with the field. When the circulation of the BPW is the same as the field, the wall width increases until it reaches a maximum. When the circulation is opposed to the field, the wall contracts until its width reaches a minimum. If the current is superior to a threshold, it breaks its structure, and the wall transform into a BPW with an opposite circulation. We showed that the threshold current is of the same order as the experiment [28], which shows that the Œrsted field plays the leading role in the circulation switching phenomenon observed. This threshold seems to follow a $1/R^3$ dependence and should apply for any soft material.

We also showed that the mechanism of the switching of circulation is not a coherent switching of the magnetization field, but rather, it involves the creation and annihilation of vortex-anti-vortex pairs and Bloch-points. Despite this complexity, the type of objects that appears during the transformation must respect a certain topological rule resulting from the continuity of the magnetization field. Meaning, the change of the winding number associated to the surface correspond to the change of the winding number associated to the volume.

Furthermore, we considered a thick-walled tube with what we call a Pseudo-Bloch-point wall inside. The main difference between this wall and the BPW is the absence of a Bloch-point in the case of the tube. We compared their structure and their dynamics. It results that the structure at the surface is very similar but inside the volume, they are different. We also showed that the circulation switching does occur for a PBPW for a threshold current slightly higher than the one of the BPW. Moreover, the switching mechanism is more complex. This additional complexity is due to the presence of the internal surface of the tube that allows the creation and annihilation of a vortex-anti-vortex pairs and Bloch-points. Finally, we have shown that the speed of the domain wall is largely determined by the spin transfer effect for the case of a BPW with the same circulation than the one of the Œrsted field.

Chapter 5

Conclusions and perspectives

To conclude, this manuscript presents a theoretical study on the current-induced dynamics of domain walls and associated critical phenomena, within two types of circular section nanowires. We combined analytical calculations and micromagnetic simulations performed with our in-house software FeeLLGood.

Chapter 3 focused on a transverse wall (TW) behavior in the smallest diameter section of the nanowire presenting a localized modulation in diameter. Such modulation acts as a potential barrier which implies that some threshold driving force must be applied to overcome the barrier. We calculated analytically the threshold value of both the applied magnetic field and the applied current as a function of the geometrical parameters. The analytical model developed is a simple scaling law, which may be useful in resolving experimental and nanofabrication issues.

While the chapter 3 treats a single modulation (a part of the geometrical protrusion) to establish the basis of the pinning phenomenon, further investigations should be focus on a single and multiple protrusions, which are relevant for applications. In our recent work, implying only the applied field and a single protrusion [39], we have shown that the protrusion length is the additional key parameter and may influence the pinning conditions. This study should be pursued and should be generalized for the applied current case.

While the control of the domain wall position may be done using geometric modulations studied in this manuscript, other alternatives and related nanofabrication constraints are discussed in the literature. For example, several studies are dedicated to the multisegmented nanowires with alternating ferromagnets of different magnetic parameters [101, 113–115] or to the cylindrical geometries including alternating tube and wire segments [84]. Both situations offer a list of open questions to be studied theoretically.

Further generalization may imply wires with several protrusions and domain walls, and the array of several nanowires. It has been shown for nanostrips that domain walls interact with each other when they are either in adjacent wires [96] or in the same wire [116, 117]. Also, the Œrsted field generated by adjacent nanowires should be considered. Consideration of these aspects is crucial to reach the high storage densities for memory applications.

Other phenomenon to be considered is the Bloch-point wall (BPW) behavior in the presence of the diameter or material properties modulations. These magnetic textures, naturally more stable in large diameter wires, are particularly interesting for reduction of the generated stray field, the non-desirable effect in the dense arrays of several nanowires. Moreover, BPW demonstrate fast dynamics crucial for high speed recording and inaccessible in systems with TWs in circular cross-section nanowires. However, the minimum wire diameter, required for the stability of the BPW ($> 7\ \ell_{\mathrm{ex}}$), implies that the compromise should be found in order to accommodate the wire diameter constraint with the desirable small size of the device.

Chapter 4 studies theoretically the impact of the Œrsted field and spin-transfer on a BPW inside a cylindrical nanowire. This study was partly motivated by our recent work [28], in which we reported the key role played by the Œrsted field in stabilizing BPWs, which are able to reach speeds up to $> 600\,\mathrm{m}\cdot\mathrm{s}^{-1}$ under applied current.

In this manuscript, we used micromagnetic simulations, analytical modeling and topological arguments to understand in detail and quantitatively the underlying phenomena. In particular the switching from negative to positive circulation of the BPW, with respect to the applied current. The main result is the $1/R^3$ dependence of the switching threshold, with R the wire radius, with the effect of the Œrsted field becoming predominant for wire radius above typically 30 nm. On the contrary, the speed of walls remains largely determined by spin-transfer alone, in a below-Walker regime. Thanks to a generalized micromagnetic scaling of lengths and densities of current, the present result may be applied to wires made of any soft magnetic material.

We are aware that the dynamics of Bloch-points in micromagnetic simulation should be treated with care. One way to refine the numerical treatment of the Bloch-point dynamics may be the use of multiscale modeling [26, 55] where the atomistic and the continuum approaches are merged. The comparison between both numerical methods may help to quantify the limits of purely micromagnetic modeling of the BPW current-driven dynamics.

Other important issue is related to the BPWs (and other magnetic textures) experimental imaging. For instance, several methods for the nanoscale characterization in the direct space (i.e. imaging) are under development locally in SPINTEC (X-ray Magnetic Dichroism, Magn. Force Imaging, Electron Holography etc) and using international facilities (Time-resolved X-ray imaging, Vectorial Field tomography with electrons). Until now, both developments (sophisticated theoretical tools and costly experimental instruments) do not benefit efficiently from each other and their accurate comparison. In this context, efforts should be done to convert usual FeeLLGood output into experimental-imagining-compatible output using the supplementary add-on module to our micromagnetic software.

In addition to single material wires, the continuous progress in nanofabrication gives rise to a new variety of multi-layered core-shell geometries. In the case of heavy metal material core with high spin-orbit coupling, the direct injection of spin-polarized electrons inside the ferromagnetic shell due the spin Hall effect is expected to give a possibility to to combine the spin-orbit torque efficiency with the high domain wall velocities within the same object. This type of systems will require the extension of physical model used in the current version of our software.

Appendix A

Appendices of chapter 1

A.1 Magnetostatic charge carried by a π-wall

A π-wall is first characterized by its boundary conditions. If $\lim_{z\to\pm\infty}\mathbf{m} = \pm 1$, we call it a tail-to-tail wall. If $\lim_{z\to\pm\infty}\mathbf{m} = \mp 1$, we call it a head-to-head wall. We associate to each one the number $Q = \pm 1$ often call the "topological charge" for tail-to-tail and head-to-head respectively. The only link i know between the magnetostatic volume charge $\rho_\mathrm{m} = -M_\mathrm{s}\nabla\cdot\mathbf{m}$ and the magnetostatic surface charge $\sigma_\mathrm{m} = M_\mathrm{s}\left(\mathbf{m}\cdot\mathbf{n}\right)$ is the divergence theorem:

$$\int_\Omega \nabla\cdot\mathbf{m}\ dV = \oint_{\partial\Omega}\mathbf{m}\cdot\mathbf{n}\ dS \tag{A.1}$$

where here Ω is a region of the wire with its respective boundary $\partial\Omega$. Hence for the magnetostatic charges, it gives:

$$\int_\Omega \rho_\mathrm{m}\ dV + \oint_{\partial\Omega}\sigma_\mathrm{m}\ dS = 0 \tag{A.2}$$

For simplicity we will consider a cylindrical nanowire. The boundary can be divided in three parts. The two sections on both sides of the wire and the lateral surface which gives $\partial\Omega = S_1\cup S_2\cup S_3$. The normal vector field for wire's end cross-sections S_1 and S_2 is trivial and gives $\mathbf{n}_{1,2} = \mp\hat{\mathbf{e}}_z$. One property of the π-wall is that whatever the inner structure of the wall, the integral over both wire's side boundaries gives always the same result:

$$\int_{S_{1,2}}\mathbf{M}\cdot\mathbf{n}_{1,2}\ dS = Q\pi R^2 M_\mathrm{s} \tag{A.3}$$

It results a total contribution of $2Q\pi R^2 M_\mathrm{s}$ from sides. To compute the charge of the lateral surface S_3 , we need to define $\mathbf{n}_3$. We define the position vector expressed using cylindrical coordinates:

$$\mathbf{r} = \rho\cos\varphi\ \hat{\mathbf{e}}_x + \rho\sin\varphi\ \hat{\mathbf{e}}_y + z\ \hat{\mathbf{e}}_z \tag{A.4}$$

The normal vector is usually constructed from a vector product of two vector tangent to the surface. In our case:

$$\mathbf{n}_3 = \partial_\varphi\mathbf{r}\times\partial_z\mathbf{r} = \rho\cos\varphi\ \hat{\mathbf{e}}_x + \rho\sin\varphi\ \hat{\mathbf{e}}_y \tag{A.5}$$

If we normalize this vector by $||\partial_\varphi\mathbf{r}\times\partial_z\mathbf{r}|| = \rho$ we get the unit normal vector of the lateral surface:

$$\hat{\mathbf{n}}_3 = \cos\varphi\ \hat{\mathbf{e}}_x + \sin\varphi\ \hat{\mathbf{e}}_y = \hat{\mathbf{e}}_\rho \tag{A.6}$$

If we want to compute the charge carried by the lateral surface, we need to define an ansatz for the magnetization field.

A.1.1 The transverse domain wall

The transverse wall is well described by the 1D model. It is convenient to define spherical coordinates w.r.t. the cartesian basis where $\mathbf{m} = (\sin\theta\cos\phi, \sin\theta\sin\phi, \cos\theta)$. Using the ansatz:

$$\theta(z) = 2\tan^{-1}\exp\left(\frac{-Qz}{\Delta}\right) \tag{A.7}$$

$$\phi(z) = \phi_{\mathrm{w}} \tag{A.8}$$

which gives the magnetization in cartesian coordinates:

$$m_x = \frac{\cos\phi_{\mathrm{w}}}{\cosh\left(\frac{z}{\Delta}\right)}, \quad m_y = \frac{\sin\phi_{\mathrm{w}}}{\cosh\left(\frac{z}{\Delta}\right)}, \quad m_z = Q\tanh\left(\frac{z}{\Delta}\right) \tag{A.9}$$

Surface charge

The integral over surface charges writes:

$$\int_{S_3} \mathbf{M}\cdot\mathbf{n}_3 \; dS = RM_{\mathrm{s}} \int_0^{2\pi}\int_{-\infty}^{\infty} \frac{\cos\phi_{\mathrm{w}}\cos\varphi}{\cosh\left(\frac{z}{\Delta}\right)} + \frac{\sin\phi_{\mathrm{w}}\sin\varphi}{\cosh\left(\frac{z}{\Delta}\right)} \; d\varphi dz \tag{A.10}$$

This double integral can be decomposed into two double integral where $\cos\phi_{\mathrm{w}}$ and $\sin\phi_{\mathrm{w}}$ can be placed outside. While the integral

$$\int_{-\infty}^{\infty} \frac{1}{\cosh\left(\frac{z}{\Delta}\right)} \; dz = \Delta\pi, \tag{A.11}$$

the integral over φ of $\cos\varphi$ and $\sin\varphi$ gives zero. As a result there is no contribution of the lateral surface to the total surface charge. Hence

$$\boxed{\oint_{\partial\Omega} \sigma_{\mathrm{m}} \; dS = 2Q\pi R^2 M_{\mathrm{s}}} \tag{A.12}$$

Volume charge

Given the divergence of $\mathbf{m}$:

$$\nabla\cdot\mathbf{m} = \frac{\partial m_x}{\partial x} + \frac{\partial m_y}{\partial y} + \frac{\partial m_z}{\partial z} \tag{A.13}$$

Using the ansatz, we see that only the last term remains and is:

$$\frac{\partial m_z}{\partial z} = \frac{Q}{\lambda\cosh^2\left(\frac{z}{\Delta}\right)} \tag{A.14}$$

which gives:

$$\int_{\Omega} \nabla\cdot\mathbf{m} \; dV = Q\int_0^R \rho d\rho \int_0^{2\pi} \; d\varphi \int_{-\infty}^{+\infty} \frac{1}{\Delta\cosh^2\left(\frac{z}{\Delta}\right)} dz \tag{A.15}$$

The total volume charge is:

$$\boxed{\int_{\Omega} \rho_{\mathrm{m}}\, dV = -2Q\pi R^2 M_{\mathrm{s}}} \tag{A.16}$$

We just have shown that (A.2) is verified. However, for a real transverse wall, the magnetization is not invariant inside the section. This manifest by a non nul transverse gradient in the volume and an asymmetric distribution of positive and negative charges at the surface. This result in a modification of the total charge carried by the wall.

$$q_{DW} = \int_{\Omega} \rho_{\mathrm{m}}\, dV + \int_{S_3} \mathbf{M} \cdot \mathbf{n}_3\, dS$$

Uniformly charged solid sphere approximation

The approximation of the uniformly charged solid sphere correspond to the definition of a closed 3-ball $B = B_R[z_{\mathrm{w}}] \subset \Omega$ of radius R centered at the wall position z_{w} which carries the entire charge of the wall. We assume this ball to be uniformly charged, thus with a constant volume charge density ρ_B. This gives us the equation

$$\int_{B} \rho_B dV = -2Q\pi R^2 M_{\mathrm{s}} \tag{A.17}$$

which gives

$$\rho_B = \frac{3q_{\mathrm{w}}}{4\pi R^3}. \tag{A.18}$$

where $q_{\mathrm{w}} = -2Q\pi R^2 M_{\mathrm{s}}$.

A.1.2 The Bloch-Point wall

The BPW does not have an analytic formulation. However, the magnetization on the lateral surface can be approximated. It is convenient to define spherical coordinates w.r.t. the cylindrical basis where $\mathbf{m} = (\sin\theta\cos\psi, \sin\theta\sin\psi, \cos\theta)$. Using the ansatz:

$$\theta(z) = 2\tan^{-1}\exp\left(\frac{-Qz}{\Delta}\right) \tag{A.19}$$

$$\psi(z) = \frac{\pi}{2} - p \tag{A.20}$$

where p is defined as the deviation angle or radial "tilt". We defined it such as $p \in [0, 2\pi]$. Thus the BPW has positive circulation if $p = 0$ and negative circulation if $p = \pi$. If $p \in]0, \pi[$, magnetization tilts out-of-plane outward (w.r.t. the local tangent plane) and if $p \in]\pi, 2\pi[$, magnetization tilts out-of-plane inward. We get for magnetization cylindrical coordinates:

$$m_\rho = \frac{\sin p}{\cosh\left(\frac{z}{\Delta}\right)}, \quad m_\varphi = \frac{\cos p}{\cosh\left(\frac{z}{\Delta}\right)}, \quad m_z = Q\tanh\left(\frac{z}{\Delta}\right) \tag{A.21}$$

We will demonstrate that this tilt depends on the boundary conditions. The integral (A.10) with this new ansatz gives:

$$RM_{\mathrm{s}}\sin p \int_0^{2\pi} d\varphi \int_{-\infty}^{\infty} \frac{1}{\cosh\left(\frac{z}{\Delta}\right)}\, dz = 2\pi^2 R\Delta M_{\mathrm{s}} \sin p \tag{A.22}$$

Hence the total surface charge with this additional contribution writes:

$$\boxed{\oint_{\partial\Omega} \sigma_{\mathrm{m}}\, dS = 2\pi R^2 M_{\mathrm{s}} \left(Q + \frac{\pi\Delta \sin p}{R} \right)} \tag{A.23}$$

The pole avoidance principle states that a magnetic system tends to avoid the creation of magnetostatic charges (i.e. the system tend to reduce the magnetostatic charge also reducing the demagnetizing energy). Hence, the tilt angle is constrained: if $Q = 1$, $\sin p$ must be negative, thus $p \in]\pi, 2\pi[$ and if $Q = -1$, $\sin p$ must be positive thus $p \in]0, \pi[$. This explain the selection of the tilt angle of the BPW depending on the boundary conditions (also called wall polarity). Indeed, it is observed that for a tail-to-tail wall, the tilt angle is out-of-plane inward w.r.t. local tangent plane and is out-of-plane outward for a head-to-head wall. Remark: If there exist other terms such as exchange or other source of anisotropy, a compromise will be made.

Appendix B

Appendices of chapter 3

B.1 Proof that $\frac{\delta\varepsilon}{\delta\phi} = 0$

In section 3.4.1 we assumed the energy density invariance with respect to the magnetization azimuthal angle $\phi_{\mathrm{w}}(t)$. We demonstrate that this statement holds for a 1D transverse domain wall. We remind that $\mathbf{m} = (\sin\theta\cos\phi, \sin\theta\sin\phi, \cos\theta)$ and the ansatz used is:

$$\theta(z,t) = 2\tan^{-1}\exp\left(\frac{z - z_{\mathrm{w}}(t)}{\Delta}\right) \tag{B.1}$$

$$\phi(z,t) = \phi_{\mathrm{w}}(t) \tag{B.2}$$

Exchange energy density

The exchange energy density is given by

$$\varepsilon_{\mathrm{ex}} = A\sum_i \left(\nabla m_i\right)^2 \tag{B.3}$$

Using the ansatz (B.1), we obtain this expression

$$\varepsilon_{\mathrm{ex}} = A\left(\partial_z\theta\right)^2 \tag{B.4}$$

which shows straightforwardly that $\frac{\partial\varepsilon_{\mathrm{ex}}}{\partial\phi} = 0$. As a side note the θ component of the exchange field is obtained from

$$\frac{\partial\varepsilon_{\mathrm{ex}}}{\partial\theta} = \frac{A}{\Delta^2}\sin 2\theta \tag{B.5}$$

Demagnetizing energy density

$$\varepsilon_{\mathrm{d}} = -\frac{\mu_0 M_{\mathrm{s}}}{2}\mathbf{m}\cdot\mathbf{H}_{\mathrm{d}} \tag{B.6}$$

The dipolar term is a non local term and writes:

$$\mathbf{H}_{\mathrm{d}}(\mathbf{r}) = \int\frac{\rho_{\mathrm{m}}(\mathbf{r}')(\mathbf{r}-\mathbf{r}')}{4\pi|\mathbf{r}-\mathbf{r}'|^3}d^3\mathbf{r}' + \oint\frac{\sigma_{\mathrm{m}}(\mathbf{r}')(\mathbf{r}-\mathbf{r}')}{4\pi|\mathbf{r}-\mathbf{r}'|^3}dS.$$

where $\rho_{\mathrm{m}} = -M_{\mathrm{s}}\nabla\cdot\mathbf{m}$ and $\sigma_{\mathrm{m}} = M_{\mathrm{s}}\mathbf{m}\cdot\mathbf{n}$.

Using the same ansatz the divergence reduces to $\partial_z m_z$. However, since $m_z = \cos\theta$, this implies automatically that the first integral does not depends on ϕ. For the surface contribution we will consider the simplest case of the infinite cylinder where $\mathbf{n} = (cos\varphi, sin\varphi, 0)$.

It can be generalized for any boundary which has revolution symmetry but for simplicity we will keep this example.

$$\mathbf{m} \cdot \mathbf{n} = \sin\theta \cos\phi_{\mathrm{w}} \cos\varphi + \sin\theta \sin\phi_{\mathrm{w}} \sin\varphi$$

The surface integral writes

$$\oint \frac{\mathbf{m}(\mathbf{r}') \cdot \mathbf{n}(\mathbf{r}')(\mathbf{r}-\mathbf{r}')}{4\pi|\mathbf{r}-\mathbf{r}'|^3} dS' = \oint \frac{\sin\theta' \cos\phi_{\mathrm{w}} \cos\varphi'(\mathbf{r}-\mathbf{r}')}{4\pi|\mathbf{r}-\mathbf{r}'|^3} dS' + \oint \frac{\sin\theta' \sin\phi_{\mathrm{w}} \sin\varphi'(\mathbf{r}-\mathbf{r}')}{4\pi|\mathbf{r}-\mathbf{r}'|^3} dS'$$

Using it into the energy expression we get

$$\mathbf{m} \cdot \mathbf{H_d} = \frac{\sin\theta}{4\pi} \left[\cos^2\phi_{\mathrm{w}} \oint \frac{\sin\theta' \ \cos\varphi'(\mathbf{r}-\mathbf{r}')}{|\mathbf{r}-\mathbf{r}'|^3} dS' + \sin^2\phi_{\mathrm{w}} \oint \frac{\sin\theta' \ \sin\varphi'(\mathbf{r}-\mathbf{r}')}{|\mathbf{r}-\mathbf{r}'|^3} dS' \right] \tag{B.7}$$

We can prove that both integrals of B.7 are equal upon a change of variable, leading to :

$$\mathbf{m} \cdot \mathbf{H_d} = \frac{\sin\theta}{4\pi} \oint \frac{\sin\theta' \ \cos\varphi'(\mathbf{r}-\mathbf{r}')}{|\mathbf{r}-\mathbf{r}'|^3} dS' \tag{B.8}$$

which is independant of ϕ_{w}. Hence, $\frac{\partial\varepsilon}{\partial\phi} = 0$

B.2 Domain wall energy expression (abrupt case)

In the follow we will compute analytically the zeeman energies from the applied field and the modulation field on a flat wall

$$\mathbf{m}(z) = \begin{cases} +\hat{\mathbf{e}}_z, & -L/2 < z < z_{\mathrm{w}}, \\ -\hat{\mathbf{e}}_z, & z_{\mathrm{w}} \leq z < L/2. \end{cases} \tag{B.9}$$

for the abrupt modulation profil:

$$R(z) = \begin{cases} R_1, & z < 0, \\ R_2, & z \geq 0. \end{cases} \tag{B.10}$$

The zeeman energy writes:

$$E_{\mathrm{z}} = -\mu_0 M_{\mathrm{s}} \int_{\Omega} \mathbf{m} \cdot \mathbf{H}_{\mathrm{ext}} dV \tag{B.11}$$

Applied field

We consider constant external field to be along the wire axis z i.e. $\mathbf{H}_{\mathrm{app}} = H_{\mathrm{a}} \hat{\mathbf{e}}_z$. In cylindrical coordinates, the integral becomes

$$E_{\mathrm{z}} = -2\pi\mu_0 M_{\mathrm{s}} \int_{-L/2}^{L/2} \left(\mathbf{m} \cdot \mathbf{H}_{\mathrm{ext}} \int_0^{R(z)} \rho d\rho \right) dz \tag{B.12}$$

We have to seperate the integral over z into three sections. Considering the wall on the left side:

$$I = \frac{H_{\mathrm{ext}}}{2} \left(\int_{-L/2}^{z_{\mathrm{w}}} R_1^2 dz - \int_{z_{\mathrm{w}}}^{0} R_1^2 dz - \int_0^{L/2} R_2^2 dz \right) \tag{B.13}$$

It results the simple expression for the zeeman energy:

$$E_{\mathrm{z}} = -\pi\mu_0 M_{\mathrm{s}} H_{\mathrm{ext}} \left(2R_1^2 z_{\mathrm{w}} + \frac{L}{2}(R_1^2 - R_2^2) \right) \tag{B.14}$$

Equivalently when the wall is on right side:

$$E_{\mathrm{z}} = -\pi\mu_0 M_{\mathrm{s}} H_{\mathrm{ext}} \left(2R_2^2 z_{\mathrm{w}} + \frac{L}{2}(R_1^2 - R_2^2) \right) \tag{B.15}$$

We can relates these energies to the volume charge of the wall q_{w}:

$$E_{\mathrm{z}} = -\mu_0 H_{\mathrm{ext}} q_{\mathrm{w}} z_{\mathrm{w}} + C \tag{B.16}$$

where $C = \mu_0 M_{\mathrm{s}} H_{\mathrm{ext}} \frac{L}{2} (\pi R_2^2 - \pi R_1^2)$ The derivative w.r.t. the wall position gives:

$$\frac{\partial E_{\mathrm{z}}}{\partial z_{\mathrm{w}}} = -\mu_0 H_{\mathrm{ext}} q_{\mathrm{w}} \tag{B.17}$$

Modulation field

Given the modulation field

$$H_{\text{mod}}(z) = \frac{M_{\text{s}}\,\text{sgn}(z_{\text{w}})}{2}\left(\frac{z}{\sqrt{R_2^2+z^2}} - \frac{z}{\sqrt{R_1^2+z^2}}\right) \tag{B.18}$$

where $\text{sgn}(z_{\text{w}}) = -1$ when the wall is on left side. The expression bla can be used when we consider the wall on the left side:

$$I = \frac{1}{2}\left(\int_{-L/2}^{z_{\text{w}}} H_{\text{mod}}(z)R_1^2dz - \int_{z_{\text{w}}}^{0} H_{\text{mod}}(z)R_1^2dz - \int_{0}^{L/2} H_{\text{mod}}(z)R_2^2dz\right) \tag{B.19}$$

The integrals of H_{mod} over z is based on the following integral

$$\int_a^b \frac{z}{\sqrt{R^2+z^2}}dz = \left[\sqrt{R^2+z^2}\right]_a^b \tag{B.20}$$

$$I = R_1^2\left(\sqrt{R_2^2+z_{\text{w}}^2} - \sqrt{R_1^2+z_{\text{w}}^2}\right) + C \tag{B.21}$$

Hence the resulting energy associated to modulation is

$$E_{\text{mod}} = \mu_0 M_{\text{s}}^2 \pi R_1^2\left(\sqrt{R_2^2+z_{\text{w}}^2} - \sqrt{R_1^2+z_{\text{w}}^2}\right) + C \tag{B.22}$$

We can relate this to the modulation field and the wall charge:

$$E_{\text{mod}} = \frac{\mu_0 M_{\text{s}} q_{\text{w}}}{2}\left(\sqrt{R_2^2+z_{\text{w}}^2} - \sqrt{R_1^2+z_{\text{w}}^2}\right) + C \tag{B.23}$$

We can then derive w.r.t. the wall position z_{w} which gives:

$$\frac{\partial E_{\text{mod}}}{\partial z_{\text{w}}} = \frac{\mu_0 M_{\text{s}} q_{\text{w}}}{2}\left(\frac{z_{\text{w}}}{\sqrt{R_2^2+z_{\text{w}}^2}} - \frac{z_{\text{w}}}{\sqrt{R_1^2+z_{\text{w}}^2}}\right) \tag{B.24}$$

We can relate it the the modulation field evaluated at the wall position z_{w}:

$$\frac{\partial E_{\text{mod}}}{\partial z_{\text{w}}} = -\mu_0 H_{\text{mod}}(z_{\text{w}}) q_{\text{w}} \tag{B.25}$$

It represent a sort of magnetic force exerted on a point magnetic charge. It is analogue to the lorentz force for the case of an electric field applied on an electric charge ($\mathbf{F} = q\mathbf{E}$).

Appendix C

Appendices of chapter 4

C.1 Dimensionless micromagnetics with Œrsted fields

It is a standard procedure to scale lengths to the dipolar exchange length in the micromagnetics of soft magnetic materials, so that results are material independent. Here, we extend the scaling to include the current density $\mathbf{j}$, source of the Œrsted field. The volume density of micromagnetic energy reads:

$$E = A\left(\boldsymbol{\nabla}\cdot\mathbf{m}\right)^2 - \frac{1}{2}\mu_0\mathbf{M}\cdot\mathbf{H}_\mathrm{d} - \mu_0\mathbf{M}\cdot\mathbf{H}_\mathrm{Œ} \tag{C.1}$$

In Eq.C.1, $\mathbf{H}_\mathrm{Œ} = (j\rho/2)\hat{\mathbf{e}}_\theta$, with ρ the distance to the wire axis. To switch to dimensionless variables, we normalize Eq.C.1 with the dipolar constant $K_\mathrm{d} = (1/2)\mu_0 M_\mathrm{s}^2$, turning to dimensionless energy e. Simultaneously, we normalize lengths with the dipolar exchange length ℓ_ex, the magnetization vector with spontaneous magnetization M_s, turning into unity $\mathbf{m}$, magnetic fields with spontaneous magnetization M_s, written $\mathbf{h}$. These normalizations are the usual ones for soft magnetic materials. In the present case, we also normalize the volume density of charge current $\mathbf{j}$ with $M_\mathrm{s}/\ell_\mathrm{ex}$, written $\tilde{\mathbf{j}}$. Eq.C.1 becomes:

$$e = \left(\boldsymbol{\nabla}_u\cdot\mathbf{m}\right)^2 - \mathbf{m}\cdot\mathbf{h}_\mathrm{d} - \tilde{\mathbf{j}}\tilde{\rho}\,\mathbf{m}\cdot\hat{\mathbf{e}}_\theta \tag{C.2}$$

$\boldsymbol{\nabla}_u$ stands for the gradient operator against the dimensionless coordinates u, and $\tilde{\rho}$ is the dimensionless distance to the axis. Thus, the results of our manuscript are valid for any soft magnetic material, provided that the above normalization is used. We drew a number of figures in the manuscript based on these dimensionless variables.

C.2 Critical current: dimensional analysis

Numerical simulations reported in Sec.4.3.4 have shown that the threshold current J_c required to switch the circulation of a BPW scales with R^{-3}, R being the radius of the nanowire. Here, we discuss the physical meaning of this scaling law, based on dimensional analysis.

The switching depends on the balance between different energies, related to the exchange interaction, the demagnetizing field and the Œrsted field. These involve the following physical quantities: exchange stiffness A in $\mathrm{J}\cdot\mathrm{m}^{-1}$, the dipolar constant $K_\mathrm{d} = (1/2)\mu_0 M_\mathrm{s}^2$ in $\mathrm{J}\cdot\mathrm{m}^{-3}$, and the Zeeman energy involving $\mu_0 M_\mathrm{s}$. Thus, the relevant independent physical quantities that may be involved in determining J_c are: the exchange stiffness A, the spontaneous magnetization M_s, the vacuum permeability μ_0 and the nanowire radius R. Therefore, an expansion of the law determining J_c must necessarily be:

$$J_\mathrm{c} \sim A^\alpha\, R^\beta\, \mu_0^\gamma\, M_\mathrm{s}^\delta\ , \tag{C.3}$$

with α, β, γ and δ dimensionless coefficients to be determined. This equation can be translated into its SI units:

$$\mathrm{A}\cdot\mathrm{m}^{-2} = \left(\mathrm{m}\cdot\mathrm{kg}\cdot\mathrm{s}^{-2}\right)^\alpha \cdot \mathrm{m}^\beta \cdot \left(\mathrm{m}\cdot\mathrm{kg}\cdot\mathrm{s}^{-2}\cdot\mathrm{A}^{-2}\right)^\gamma \cdot \left(\mathrm{A}\cdot\mathrm{m}^{-1}\right)^\delta\ , \tag{C.4}$$

which leads to the following set of equations, related to the powers of meter, kilogram, second and Ampere:

$$\begin{aligned} \alpha+\beta+\gamma-\delta &= -2 && \text{(C.5)}\\ \alpha+\gamma &= 0 && \text{(C.6)}\\ -2\alpha-2\gamma &= 0 && \text{(C.7)}\\ -2\gamma+\delta &= 1 && \text{(C.8)} \end{aligned}$$

Eq.C.6 and Eq.C.7 are equivalent, so that this set becomes:

$$\begin{aligned} \beta &= -1-2\alpha && \text{(C.9)}\\ \gamma &= -\alpha && \text{(C.10)}\\ \delta &= 1-2\alpha && \text{(C.11)} \end{aligned}$$

This set of equations is under-determined once, with α taking any possible value. Writing $\alpha = 1+n$, we end up in:

$$J_\mathrm{c} \sim \sum_n C_n \frac{A}{\mu_0 M_\mathrm{s} R^3} \left(\frac{\ell_\mathrm{ex}}{R}\right)^{2n} \tag{C.12}$$

with coefficients C_n. So, dimensional analysis alone does not allow to explain that $J_\mathrm{c} \sim 1/R^3$, which corresponds to a predominant C_0. This suggests that the dipolar exchange length is largely irrelevant. Said differently, the remaining term $A/(\mu_0 M_\mathrm{s} R^3)$ can be decomposed as the ratio of A/R^2 with $\mu_0 M_\mathrm{s} R$, suggesting a competition of exchange energy and Œrsted Zeeman energy alone, to determine the switching of circulation. A model based on this competition is detailed below.

C.3 Critical current: analytical model for the scaling law

Here we propose a simple argument to explain the $1/R^3$ dependence of the threshold current J_c for circulation switching [Fig.4.9]. The model does not intend to be a rigorous one, however to put forward the physical ground responsible for this scaling law.

The previous section suggested that J_c is predominantly determined by the competition of exchange and Zeeman Œrsted energies. We consider this competition in the curling effect in the domains, for which the absence of dipolar fields, and the translational symmetry, allow a straightforward modeling. The Œrsted field forces magnetization at radius ρ to acquire an azimuthal component, tilting from $\hat{\mathbf{z}}$ towards $\hat{\mathbf{e}}_\phi$. We propose to describe this tilt with a test function:

$$\theta(\rho) = \theta_0 \sin\left(\frac{\pi}{2}\frac{\rho}{R}\right). \tag{C.13}$$

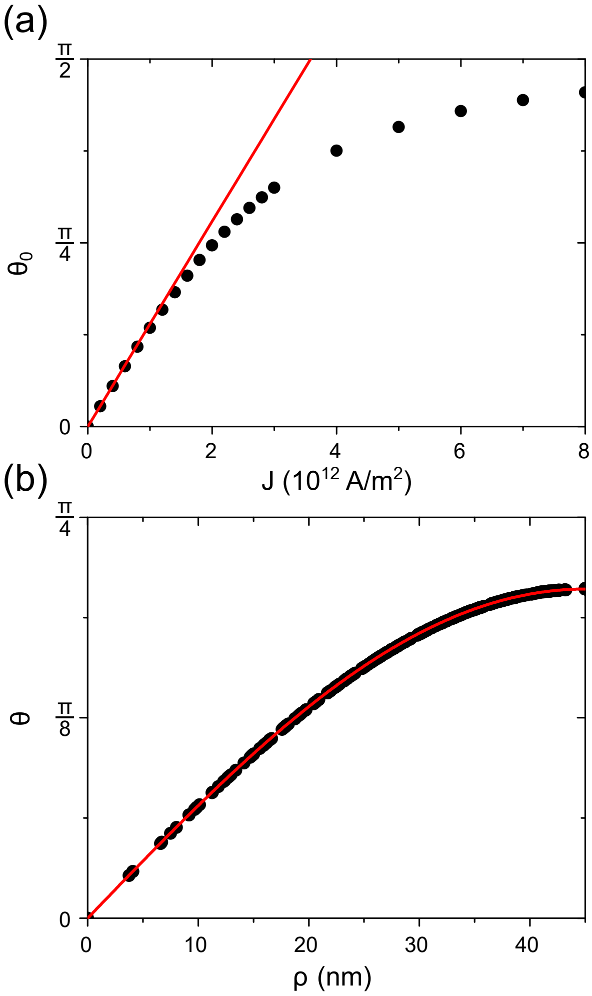

Figure C.1: Comparison of the analytical model versus micromagnetic simulations, for the effect of the Œrsted field on magnetization in an extended domain. We used following parameters: wire radius $R = 45\,\mathrm{nm}$, $A = 1.1 \times 10^{-11}\,\mathrm{J \cdot m^{-1}}$ and $M_\mathrm{s} = 6.7 \times 10^5\,\mathrm{A \cdot m^{-1}}$. The line stand for the (linear) analytical solution [Eq.C.18], while symbols stand for micromagnetic simulations. (a) Current density j required to reach a given azimuthal tilt of magnetization θ_0 on the nanowire surface, in an initially uniformly-magnetized domain. (b) Radial variation of the tilt of magnetization θ, for $j = 1.6 \times 10^{12}\,\mathrm{A^2 \cdot m^{-1}}$. Adapted from [62].

R is the external radius and $\theta_0 = \theta(\rho = R)$. The volume density of exchange energy E_ex and of the Zeeman Œrsted energies, read:

$$\begin{aligned} E_\mathrm{ex} &= A\left[\left(\frac{\partial\theta}{\partial\rho}\right)^2 + \frac{\sin^2(\theta)}{\rho^2}\right], &\text{(C.14)}\\ E_\mathrm{Z} &= -\mu_0 M_\mathrm{s}\frac{j\rho}{2}\sin(\theta). &\text{(C.15)}\end{aligned}$$

The total energy for a wire length L is:

$$\mathcal{E}_\mathrm{T} = \int_0^R 2\pi\rho L\left(E_\mathrm{ex} + E_\mathrm{Z}\right)\mathrm{d}\rho. \tag{C.16}$$

This integral may be evaluated by making use of a Taylor series expansion of $\sin(x)$ around $x = 0$, and consideration of the test function for $\theta(\rho)$. Expanding to second order for θ_0, Eq.C.16 becomes:

$$\xi_{\mathrm{T}} = \frac{\pi^3 L A \theta_0^2}{4}\left(2 - \frac{\pi^2}{6} + \frac{10\pi^4}{1728}\right) - \frac{\pi^2 \mu_0 M_{\mathrm{S}} L j R^3 \theta_0}{8}\left(1 - \frac{\pi^2}{36}\right). \tag{C.17}$$

The minimization of this total energy with respect to θ_0, we find a simple relation between j, θ_0 and R:

$$j = \frac{4\pi A \theta_0}{\mu_0 M_{\mathrm{s}} R^3} \frac{\left(1 - \frac{\pi^2}{36}\right)}{\left(2 - \frac{\pi^2}{6} + \frac{10\pi^4}{1728}\right)}. \tag{C.18}$$

Fig.C.1a compares the relationship between θ_0 and j, the linear law in the present analytical model [Eq.C.18], and micromagnetic simulations. The match is excellent at low angle, until $\theta_0 \approx \pi/3$, a range consistent with the expansion of the sin function. The deviation beyond this point is not troublesome, as the associated density of current is too high to be experimentally relevant. The perfect match between the simulation and the analytical model is equally observed in the radial dependence of the tilting of magnetization [Fig.C.1(b)] for low applied current densities. In conclusion, Eq.C.18 is perfectly valid, suggesting the origin of the law $J_{\mathrm{c}} \sim 1/R^3$ as resulting from the dominant competition between exchange and Zeeman energies.

References

[1] Parkin S. & Yang S.-H. *Memory on the racetrack.* Nature Nanotech **10**, 195–198 (2015).

[2] Allwood D. A., Xiong G., Faulkner C. C., Atkinson D., Petit D. & Cowburn R. P. *Magnetic domain-wall logic.* Science **309**, 1688–1692 (2005).

[3] Lequeux S., Sampaio J., Cros V., Yakushiji K., Fukushima A., Matsumoto R., Kubota H., Yuasa S. & Grollier J. *A magnetic synapse: Multilevel spin-torque memristor with perpendicular anisotropy.* Sci Rep **6**, 31510 (2016).

[4] Thiele A. A. *Steady-state motion of magnetic domains.* Phys. Rev. Lett. **30**, 230–233 (1973).

[5] Ono T., Miyajima H., Shigeto K., Mibu K., Hosoito N. & Shinjo T. *Propagation of a magnetic domain wall in a submicrometer magnetic wire.* Science **284**, 468–470 (1999).

[6] Grollier J., Boulenc P., Cros V., Hamzic A., Vaurès A., Fert A. & Faini G. *Switching a spin valve back and forth by current-induced domain wall motion.* Appl. Phys. Lett. **83**, 509–511 (2003).

[7] Miron I. M., Gaudin G., Auffret S., Rodmacq B., Schuhl A., Pizzini S., Vogel J. & Gambardella P. *Current-driven spin torque induced by the rashba effect in a ferromagnetic metal layer.* Nat. Mater. **9**, 230 (2010).

[8] Chauleau J.-Y., Weil R., Thiaville A. & Miltat J. *Magnetic domain walls displacement: Automotion versus spin-transfer torque.* Phys. Rev. B **82**, 214414 (2010).

[9] Dean J., Bryan M. T., Cooper J. D., Virbule A., Cunningham J. E. & Hayward T. J. *A sound idea: Manipulating domain walls in magnetic nanowires using surface acoustic waves.* Appl. Phys. Lett. **107**, 142405 (2015).

[10] Hinzke D. & Nowak U. *Domain Wall Motion by the Magnonic Spin Seebeck Effect.* Phys. Rev. Lett. **107**, 027205 (2011).

[11] Thiaville A. & Nakatani Y. *Spin dynamics in confined magnetic structures III*, vol. 101 of *Topics Appl. Physics*, chap. Domain-wall dynamics in nanowires and nanostrips, 161–205 (Springer, Berlin, 2006).

[12] Thiaville A. & Nakatani Y. *Nanomagnetism and Spintronics*, chap. Micromagnetic simulation of domain wall dynamics in nanostrips, 231–276 (Elsevier, 2009).

[13] Fernandez-Pacheco A., Streubel R., Fruchart O., Hertel R., Fischer P. & Cowburn R. P. *Three-dimensional magnetism.* Nat. Commun. **8**, 15756 (2017).

[14] Paulus P., Luis F., Kröll M., Schmid G. & de Jongh L. *Low-temperature study of the magnetization reversal and magnetic anisotropy of Fe, Ni, and Co nanowires.* Journal of Magnetism and Magnetic Materials **224**, 180–196 (2001).

[15] Jamet S., Rougemaille N., Toussaint J. & Fruchart O. *Head-to-head domain walls in one-dimensional nanostructures.* In *Magnetic Nano- and Microwires*, 783–811 (Elsevier, 2015).

[16] Ferguson C. A., MacLaren D. A. & McVitie S. *Metastable magnetic domain walls in cylindrical nanowires.* Journal of Magnetism and Magnetic Materials **381**, 457–462 (2015).

[17] Feldtkeller E. *Mikromagnetisch stetige und unstetige Magnetisierungskonfigurationen.* Z. Angew. Physik **19**, 530 (1965).

[18] Feldtkeller E. *Continuous and Singular Micromagnetic Configurations.* IEEE Trans. Magn. **53**, 1–8 (2017).

[19] Berganza E., Jaafar M., Bran C., Fernández-Roldán J. A., Chubykalo-Fesenko O., Vázquez M. & Asenjo A. *Multisegmented nanowires: a step towards the control of the domain wall configuration.* Sci. Rep. **7**, 11576 (2017).

[20] Pitzschel K., Bachmann J., Martens S., Montero-Moreno J. M., Kimling J., Meier G., Escrig J., Nielsch K. & Görlitz D. *Magnetic reversal of cylindrical nickel nanowires with modulated diameters.* J. Appl. Phys. **109**, 033907 (2011).

[21] Berganza E., Bran C., Vazquez M. & Asenjo A. *Domain wall pinning in fecocu bamboo-like nanowires.* Sci. Rep. **6**, 29702 (2016).

[22] Esmaeily A. S., Venkatesan M., Razavian A. S. & Coey J. M. D. *Diameter-modulated ferromagnetic CoFe nanowires.* Journal of Applied Physics **113**, 17A327 (2013).

[23] Iglesias-Freire Ó., Bran C., Berganza E., Mínguez-Bacho I., Magén C., Vázquez M. & Asenjo A. *Spin configuration in isolated FeCoCu nanowires modulated in diameter.* Nanotechnology **26**, 395702 (2015).

[24] Palmero E. M., Bran C., del Real R. P. & Vázquez M. *Synthesis and magnetism of modulated FeCo-based nanowires.* J. Phys.: Conf. Ser. **755**, 012001 (2016).

[25] Mohanan P V. & Kumar P. S. A. *Chirality dependent pinning and depinning of magnetic vortex domain walls at nano-constrictions.* Journal of Magnetism and Magnetic Materials **422**, 419–424 (2017).

[26] Hertel R. *Ultrafast domain wall dynamics in magnetic nanotubes and nanowires.* J. Phys.: Condens. Matter **28**, 483002 (2016).

[27] Yan M., Kákay A., Gliga S. & Hertel R. *Beating the Walker Limit with Massless Domain Walls in Cylindrical Nanowires.* Phys. Rev. Lett. **104**, 057201 (2010).

[28] Schöbitz M., De Riz A., Martin S., Bochmann S., Thirion C., Vogel J., Foerster M., Aballe L., Menteş T. O., Locatelli A., Genuzio F., Le-Denmat S., Cagnon L., Toussaint J. C., Gusakova D., Bachmann J. & Fruchart O. *Fast Domain Wall Motion Governed by Topology and Oersted Fields in Cylindrical Magnetic Nanowires.* Phys. Rev. Lett. **123**, 217201 (2019).

[29] Allende S., Altbir D. & Nielsch K. *Magnetic cylindrical nanowires with single modulated diameter.* Phys. Rev. B **80**, 174402 (2009).

[30] Salem M. S., Sergelius P., Corona R. M., Escrig J., Görlitz D. & Nielsch K. *Magnetic properties of cylindrical diameter modulated Ni80Fe20 nanowires: interaction and coercive fields.* Nanoscale (2013).

[31] Chandra Sekhar M., Liew H. F., Purnama I., Lew W. S., Tran M. & Han G. C. *Helical domain walls in constricted cylindrical NiFe nanowires.* Appl. Phys. Lett. **101**, 152406 (2012).

[32] Fernandez-Roldan J. A., del Real R. P., Bran C., Vazquez M. & Chubykalo-Fesenko O. *Magnetization pinning in modulated nanowires: from topological protection to the "corkscrew" mechanism.* Nanoscale **10**, 5923 (2018). `1801.00643v1`.

[33] Allende S. & Arias R. *Transverse domain wall propagation in modulated cylindrical nanostructures and possible geometric control.* Phys. Rev. B **83**, 174452 (2011).

[34] Hertel R. & Kirschner J. *Magnetization reversal dynamics in nickel nanowires.* Physica B **343**, 206 (2004).

[35] Wieser R., Vedmedenko E. Y., Weinberger P. & Wiesendanger R. *Current-driven domain wall motion in cylindrical nanowires.* Phys. Rev. B **82**, 144430 (2010).

[36] Alouges F. & Jaisson P. *Convergence of a finite element discretization for the landau-lifshitz equations in micromagnetism.* Mathematical Models and Methods in Applied Sciences **16**, 299–316 (2006).

[37] Alouges F., Kritsikis E., Steiner J. & Toussaint J.-C. *A convergent and precise finite element scheme for Landau–Lifschitz–Gilbert equation.* Numer. Math. **128**, 407–430 (2014).

[38] *feeLLGood Software.* `http://feellgood.neel.cnrs.fr/`.

[39] De Riz A., Trapp B., Fernandez-Roldan J., Thirion C., Toussaint J.-C., Fruchart O. & Gusakova D. *Domain wall pinning in a circular cross-section wire with modulated diameter.* In *Magnetic Nano- and Microwires*, 427–453 (Elsevier, 2020).

[40] Brown W. F. *Micromagnetics* (Wiley, 1963).

[41] Coey J. M. D. *Magnetism and magnetic materials* (Cambride University Press, 2010).

[42] Jackson J. D. *Classical Electrodynamics* (Wiley, 1975).

[43] Abert C. *Discrete Mathematical Concepts in Micromagnetic Computations.* Ph.D. thesis University of Hamburg (2013).

[44] Gilbert T. *A phenomenological theory of damping in ferromagnetic materials.* IEEE Trans. Magn. **40**, 3443–3449 (2004).

[45] Slonczewski J. C. *Current-driven excitation of magnetic multilayers.* J. Magn. Magn. Mater. **159**, L1–L7 (1996).

[46] Zhang S. & Li Z. *Roles of Nonequilibrium Conduction Electrons on the Magnetization Dynamics of Ferromagnets.* Phys. Rev. Lett. **93**, 127204 (2004).

[47] Thiaville A., Nakatani Y., Miltat J. & Suzuki Y. *Micromagnetic understanding of current-driven domain wall motion in patterned nanowires.* Europhys. Lett. **69**, 990–996 (2005).

[48] Forster H., Schrefl T., Suess D., Scholz W., Tsiantos V., Dittrich R. & Fidler J. *Domain wall motion in nanowires using moving grids.* J. Appl. Phys. **91**, 6914 (2002).

[49] Hertel R. *Thickness dependence of magnetization structures in thin permalloy rectangles.* Z. Mettalkd **93**, 957 (2002).

[50] Thiaville A., Garcìa J. M., Dittrich R., Miltat J. & Schrefl T. *Micromagnetic study of Bloch-point-mediated vortex core reversal.* Phys. Rev. B **67**, 094410 (2003).

[51] Yan M., Kákay A., Gliga S. & Hertel R. *Beating the Walker limit with massless domain walls in cylindrical nanowires.* Phys. Rev. Lett. **104**, 057201 (2010).

[52] Bartels S. & Prohl A. *Constraint preserving implicit finite element discretization of harmonic map flow into spheres.* Math. Comp. **76**, 1847–1860 (2007).

[53] Dutt A. & Rokhlin V. *Fast Fourier Transforms for Nonequispaced Data.* SIAM J. Sci. Comput. **14**, 1368–1393 (1993).

[54] White C. A. & Head-Gordon M. *Rotating around the quartic angular momentum barrier in fast multipole method calculations.* J. Chem. Phys. **105**, 5061–5067 (1996).

[55] Andreas C., Kákay A. & Hertel R. *Multiscale and multimodel simulation of bloch-point dynamics.* Phys. Rev. B **89**, 134403 (2014).

[56] Hertel R. & Kákay A. *Analytic form of transverse head-to-head domain walls in thin cylindrical wires.* Journal of Magnetism and Magnetic Materials **379**, 45–49 (2015).

[57] Blügel S. & Bihlmayer G. *Handbook of magnetism and magnetic materials*, vol. 1, chap. Magnetism of Low-dimensional Systems: Theory (Wiley, 2007).

[58] Garanin D. A. *Fokker-Planck and Landau-Lifshitz-Bloch equations for classical ferromagnets.* Phys. Rev. B **55**, 3050 (1997).

[59] Lebecki K. M., Hinzke D., Nowak U. & Chubykalo-Fesenko O. *Key role of temperature in ferromagnetic Bloch point simulations.* Phys. Rev. B **86**, 094409 (2012).

[60] Yan M., Andreas C., Kakay A., Garcia-Sanchez F. & Hertel R. *Fast domain wall dynamics in magnetic nanotubes: Suppression of Walker breakdown and Cherenkov-like spin wave emission.* Appl. Phys. Lett. **99**, 122505 (2011).

[61] Landeros P. & Núñez A. S. *Domain wall motion on magnetic nanotubes.* J. Appl. Phys. **108**, 033917 (2010).

[62] De Riz A., Hurst J., Schöbitz M., Thirion C., Bachmann J., Toussaint J. C., Fruchart O. & Gusakova D. *Mechanism of fast domain wall motion via current-assisted Bloch-point domain wall stabilization.* Phys. Rev. B **103**, 054430 (2021).

[63] Fernandez-Roldan J. A., De Riz A., Trapp B., Thirion C., Vazquez M., Toussaint J.-C., Fruchart O. & Gusakova D. *Modeling magnetic-field-induced domain wall propagation in modulated-diameter cylindrical nanowires.* Scientific Reports **9** (2019).

[64] Barnes S. E., Ieda J. & Maekawa S. *Magnetic memory and current amplification devices using moving domain walls.* Appl. Phys. Lett. **89**, 122507 (2006).

[65] Parkin S. S. P., Hayashi M. & Thomas L. *Magnetic domain-wall racetrack memory.* Science **320**, 190 (2008).

[66] Lavrijsen R., Lee J.-H., Fernandez-Pacheco A., Petit D. C. M. C., Mansell R. & Cowburn R. P. *Magnetic ratchet for three-dimensional spintronic memory and logic.* Nature **493**, 647–650 (2013).

[67] Allwood D. A., Xiong G., Cooke M. D., C.Faulkner C., Atkinson D., Vernier N. & Cowburn R. P. *Submicrometer ferromagnetic not gate and shift register.* Science **296**, 2003–2006 (2002).

[68] Hayashi M., Thomas L., Rettner C., Moriya R. & Parkin S. S. P. *Direct observation of the coherent precession of magnetic domain walls propagating along permalloy nanowires.* Nat. Phys. **3**, 21 (2007).

[69] Bochmann S., Döhler D., Trapp B., Staňo M., Wartelle A., Fruchart O. & Bachmann J. *Preparation and physical properties of soft magnetic nickel-cobalt nanowires with modulated diameters.* J. Appl. Phys. **124**, 163907 (2018).

[70] Yokoyama Y., Suzuki Y., Yuasa S., Ando K., Shigeto K., Shinjo T., Gogol P., Miltat J., Thiaville A., Ono T. & Kawagoe T. *Kerr microscopy observations of magnetization process in microfabricated ferromagnetic wires.* J. Appl. Phys. **87**, 5618 (2000).

[71] Bryan M. T., Schrefl T. & Allwood D. A. *Symmetric and asymmetric domain wall diodes in magnetic nanowires.* Appl. Phys. Lett. **91**, 142502 (2007).

[72] Lewis E. R., Petit D., O'Brien L., Fernandez-Pacheco A., Sampaio J., Jausovec A.-V., Read H. T. Z. D. E. & Cowburn R. P. *Fast domain wall motion in magnetic comb structures.* Nat. Mater. 980 (2010).

[73] Beguivin A., O'Brien L. A., Jausovec A. V., Petit D. & Cowburn R. P. *Magnetisation reversal in permalloy nanowires controlled by near-field charge interactions.* Appl. Phys. Lett. **99**, 142506 (2011).

[74] Sampaio J., O.'Brien L., Read D. E., Lewis E. R., Zeng H. T., Petit D., anf L. Thevenard R. P. C. & Cardoso S. *Coupling and induced depinning of magnetic domain walls in adjacent spin valve nanotracks.* J. Appl. Phys. (2013).

[75] Vogel A., Wintz S., Gerhardt T., Bocklage L., Strache T., Im M.-Y., Fischer P., Fassbender J., McCord J. & Meier G. *Field- and current-induced domain-wall motion in permalloy nanowires with magnetic soft spots.* Appl. Phys. Lett. **98**, 202501 (2011).

[76] Serrano-Raman L., Fernandez-Pacheco A., Ibarra M. R., Petit D., Cowburn R. P., Tyliszczak T. & De Teresa J. M. *Modification of domain-wall propagation in co nanowires via ga+ irradiation.* Eur. Phys. J. B **86**, 97 (2013).

[77] Bauer U., Emori S. & Beach G. S. D. *Voltage-controlled domain wall traps in ferromagnetic nanowires.* Nat. Nanotechnol. **8**, 411–416 (2013).

[78] Fert A. & Piraux J. L. *Magnetic nanowires.* J. Magn. Magn. Mater. **200**, 338–358 (1999).

[79] Sousa C. T., Leitao D. C., Proenca M. P., Ventura J., Pereira A. M. & Araujo J. P. *Nanoporous alumina as templates for multifunctional applications.* Appl. Phys. Rev. **1**, 031102 (2014).

[80] Staňo M. & Fruchart O. *Handbook of Magnetic Materials*, vol. 27, chap. Magnetic nanowires and nanotubes (Elsevier, 2018).

[81] Salem M. S., Tejo F., Zierold R., Sergelius P., Moreno J. M. M., Görlitz D., Nielsch K. & Escrig J. *Composition and diameter modulation of magnetic nanowire arrays fabricated by a novel approach.* Nanotechnology **29**, 065602 (2018).

[82] Lee W. & Kim J.-C. *Highly ordered porous alumina with tailor-made pore structures fabricated by pulse anodization.* Nanotechnology **21**, 485304 (2010).

[83] Salazar-Aravena D., Corona R. M., Goerlitz D. & Escrig K. J. *Magnetic properties of multisegmented cylindrical nanoparticles with alternating magnetic wire and tube segments.* J. Magn. Magn. Mater. **346**, 171 – 174 (2013).

[84] Neumann R. F., Bahiana M., Vargas N. M., Altbir D., Allende S., Görlitz D. & Nielsch K. *Domain wall control in wire-tube nanoelements.* Appl. Phys. Lett. **102**, 202407 (2013).

[85] Dubois S., Piraux L., George J. M., Ounadjela K., Duvail J. L. & Fert A. *Evidence for a short spin diffusion length in permalloy from the giant magnetoresistance of multilayered nanowires.* Phys. Rev. B **60**, 477–484 (1999).

[86] Bochmann S., Fernandez-Pacheco A., Mačkovič M., Neff A., Siefermann K. R., Spiecker E., Cowburn R. P. & Bachmann J. *Systematic tuning of segmented magnetic nanowires into three-dimensional arrays of 'bits'.* RCS Adv. **7**, 37627 (2017).

[87] Bran C., Ivanov Y. P., Kosel J., Chubykalo-Fesenko O. & Vazquez M. *Co/Au multisegmented nanowires: a 3d array of magnetostatically coupled nanopillars.* Nanotechnology **28**, 095709 (2017).

[88] Becker R. *Elastische Spannungen und magnetische Eigenschaften.* Physikalische Zeitschrift **33**, 905–913 (1932).

[89] Becker R. & Döring W. *Ferromagnetismus* (Springer, 1939).

[90] Kondorski E. *On the nature of coercive force and irreversible changes in magnetisation.* Phys. Z. Sowjetunion **11**, 597 (1937).

[91] Kondorski E. J. J. Exp. Theor. Fiz. **10**, 420 (1940).

[92] Aharoni A. *Reduction in coercive force caused by a certain type of imperfection.* Phys. Rev. **119**, 127–131 (1960).

[93] Abraham C. & Aharoni A. *Linear decrease in the magnetocrystalline anisotropy.* Phys. Rev. **120**, 1576–1579 (1960).

[94] Trapp B. *Nucleation and Propagation of Magnetic Domain Walls in Cylindrical Nanowires with Diameter Modulations.* Ph.D. thesis Université Grenoble Alpes (2018).

[95] Hubert A. & Schäfer R. *Magnetic domains. The analysis of magnetic microstructures* (Springer, Berlin, 1999).

[96] Krüger B. *The interaction of transverse domain walls.* J. Phys.: Condens. Matter **24**, 024209 (2012).

[97] Landeros P. & Núñez Á. S. *Domain wall motion on magnetic nanotubes.* Journal of Applied Physics **108**, 033917 (2010).

[98] Da Col S., Jamet S., Rougemaille N., Locatelli A., Menteş T. O., Burgos B. S., Afid R., Darques M., Cagnon L., Toussaint J. C. & Fruchart O. *Observation of bloch-point domain walls in cylindrical magnetic nanowires.* Phys. Rev. B **89**, 180405 (2014).

[99] Wartelle A., Trapp B., Staňo M., Thirion C., Bochmann S., Bachmann J., Foerster M., Aballe L., Menteş T. O., Locatelli A., Sala A., Cagnon L., Toussaint J. & Fruchart O. *Bloch-point-mediated topological transformations of magnetic domain walls in cylindrical nanowires.* Phys. Rev. B **99**, 024433 (2019). ArXiv:1806.10918.

[100] Biziere N., Gatel C., Lassalle-Balier R., Clochard M. C., Wegrowe J. E. & Snoeck E. *Imaging the fine structure of a magnetic domain wall in a ni nanocylinder.* Nano Lett. **13**, 2053 (2013).

[101] Ivanov Y. P., Chuvilin A., Lopatin S. & Kosel J. *Modulated magnetic nanowires for controlling domain wall motion: Toward 3D magnetic memories.* Am. Chem. Soc. Nano **10**, 5326 (2016).

[102] Bauer M., Fassbender J., Hillebrands B. & Stamps R. L. *Switching behavior of a Stoner particle beyond the relaxation time limit.* Phys. Rev. B **61**, 3410–3416 (2000).

[103] Cheynis F., Masseboeuf A., Fruchart O., Rougemaille N., Toussaint J. C., Belkhou R., Bayle-Guillemaud P. & Marty A. *Controlled switching of néel caps in flux-closure magnetic dots.* Phys. Rev. Lett. **102**, 107201 (2009).

[104] Wartelle A., Thirion C., Afid R., Jamet S., Da Col S., Cagnon L., Toussaint J.-C., Bachmann J., Bochmann S., Locatelli A., Onur Menteş T. & Fruchart O. *Broadband setup for magnetic-field-induced domain wall motion in cylindrical nanowires.* IEEE Trans. Magn. **51**, 4300403 (2015).

[105] Braun H.-B. *Topological effects in nanomagnetism: From superparamagnetism to chiral quantum solitons.* Advances in Physics **61**, 1–116 (2012).

[106] Braun H.-B. *Solitons in real space: Domain walls, vortices, hedgehogs, and skyrmions.* In *Springer Series in Solid-State Sciences*, 1–40 (Springer International Publishing, 2018).

[107] Tretiakov O. A. & Tchernyshyov O. *Vortices in thin ferromagnetic films and the skyrmion number.* Phys. Rev. B **75**, 012408 (2007).

[108] Tchernyshyov O. & Chern G. W. *Fractional vortices and composite domainwalls in flat nanomagnets.* Phys. Rev. Lett. **95**, 197204–7 (2005).

[109] Rave W., Ramstöck K. & Hubert A. *Corners and nucleation in micromagnetics.* J. Magn. Magn. Mater. **183**, 329–333 (1998).

[110] Fruchart O., Toussaint J. C. & Kevorkian B. *Micromagnetic model of non-collective magnetization reversal in ultrathin magnetic dots with in-plane uniaxial anisotropy.* Phys. Rev. B **63**, 174418 (2001).

[111] Sun J. Z. *Spin-current interaction with a monodomain magnetic body: A model study.* Phys. Rev. B **62**, 570–578 (2000).

[112] Bedau D., Liu H., Bouzaglou J.-J., Kent A. D., Sun J. Z., Katine J. A., Fullerton E. E. & Mangin S. *Ultrafast spin-transfer switching in spin valve nanopillars with perpendicular anisotropy.* Appl. Phys. Lett. **96**, 022514 (2010).

[113] Kim W. J., Lee T. D. & Lee K. J. *Domain wall pinning by alternating materials in current-induced domain wall motion: Domain wall pinning by alternating materials.* phys. stat. sol. (b) **244**, 4439–4442 (2007).

[114] García Fernández J., Vega Martínez V., Thomas A., de la Prida Pidal V. & Nielsch K. *Two-Step Magnetization Reversal FORC Fingerprint of Coupled Bi-Segmented Ni/Co Magnetic Nanowire Arrays.* Nanomaterials **8**, 548 (2018).

[115] Bran C., Berganza E., Fernandez-Roldan J. A., Palmero E. M., Meier J., Calle E., Jaafar M., Foerster M., Aballe L., Rodriguez A. F., del Real R. P., Asenjo A., Chubykalo-Fesenko O. & Vazquez M. *Magnetization ratchet in cylindrical nanowires.* Am. Chem. Soc. Nano **12**, 5932–5939 (2018).

[116] Thomas L., Hayashi M., Moriya R., Rettner C. & Parkin S. *Topological repulsion between domain walls in magnetic nanowires leading to the formation of bound states.* Nature Communications **3**, 810 (2012).

[117] Pivano A. & Dolocan V. O. *Analytical description of the topological interaction between magnetic domain walls in nanowires.* Phys. Rev. B **101**, 014438 (2020).

Abstract

This thesis presents a theoretical study of the magnetic domain wall behavior in magnetically soft nanowires with a circular cross section subjected to an applied electron current. My work focuses on the domain wall dynamics and related critical phenomena such as domain wall pinning and the internal wall structure transformations. We combined micromagnetic simulations with simplified analytical models, to provide an overview of key parameters, useful in predicting and understanding experiments. In particular, the manuscript quantifies two critical phenomena. First, we discuss the control of the transverse domain wall position by introducing geometrical inhomogeneities in the moderate diameter wires ($< 7\ l_{ex}$). Diameter modulations play the role of a potential barrier which implies that some threshold driving force must be applied to overcome the barrier. We calculated the threshold current-induced and field-induced driving force as a function of the geometrical parameters. The analytical model developed is a simple scaling law, which may be useful in resolving experimental and nanofabrication issues. Second, we quantify the effect of the spin-transfer torque together with the Œrsted field generated by the electric current in large diameter wires ($> 7\ l_{ex}$). For such diameters, the Bloch-point walls, which exhibit several interesting features, occur to be the most stable configurations. The Bloch-point wall is characterized by a micromagnetic singularity, the Bloch-Point, and by a curling magnetization (thus a circulation). In the frame of this thesis, we showed that the previously overlooked Œrsted field is key in experiments to stabilize the BPW and reach speed above 600m/s with spin-transfer. The switching of the azimuthal circulation of the BPW to match that of the Œrsted field occurs above a threshold current which we quantify as a function of geometry and material parameters. We also highlight the complexity of BPW transformation involving topological objects at the surface and in the volume.

Résumé

Cette thèse présente une étude théorique de la dynamique de parois de domaines magnétiques sous courant dans des nanofils magnétiques doux à section circulaire. Ce travail se focalise sur la dynamique de parois de domaines et les phénomènes critiques qui en découlent, tels que le piègeage de parois et le changement de leur structure interne. Nous combinons des simulations micromagnétiques avec des descriptions analytiques simplifiées afin de fournir une vue d'ensemble des paramètres clés, utiles à la prédiction et à la compréhension des expériences. En particulier, le manuscrit quantifie deux phénomènes critiques. Premièrement, nous nous sommes intéressés au contrôle de la position d'une paroi de domaines transverse par l'introduction d'inhomo-généités géométriques pour des fils de diamètres modérés ($< 7\ l_{ex}$). Il peut être exercé à l'aide de modulations de diamètre, créant une barrière de potentiel s'opposant à la propagation, et donc, nécessitant une amplitude seuil (de champ ou de courant) pour la franchir. Nous avons calculé en fonction des paramètres géométriques, le courant et le champ de seuil. Le modèle analytique développé est une simple loi d'échelle qui peut être utilisée dans la résolution de problèmes expérimentaux. Deuxièmement, nous quantifions les effets du transfer de spin et du champ d'Œrsted généré par le courant éléctrique dans des fils de diamètre ($> 7\ \ell_{\mathrm{ex}}$). Pour de tels diamètres, les parois point-de-Bloch, qui présentent des propriétés intéressantes, sont les configurations les plus stables. La paroi point-de-Bloch est caractérisée par une singularité, le point-de-Bloch, et une aimantation azimuthale (donc une circulation). Dans le cadre de cette thèse, nous avons montré que le champ d'Œrsted, généralement négligé, est essentiel à la stabilisation des parois point-de-Bloch, permettant d'atteindre des vitesses au delà de 600m/s sous transfer de spin. Tout particulièrement, le manuscrit quantifie le courant de seuil necessaire au changement de circulation de parois de Point-de-Bloch, observé expérimentalement dans un travail récent, exprimé sous la forme d'une loi d'échelle. Nous mettons aussi en évidence la complexité de transformation de Point-de-Bloch impliquant les objets topologiques en volume et en surface.